

*A Floating Probe Force Microscope with  
Sub-Femtonewton Resolution*

A DISSERTATION PRESENTED  
BY  
LULU LIU  
TO  
THE SCHOOL OF ENGINEERING AND APPLIED SCIENCES

IN PARTIAL FULFILLMENT OF THE REQUIREMENTS  
FOR THE DEGREE OF  
DOCTOR OF PHILOSOPHY  
IN THE SUBJECT OF  
APPLIED PHYSICS

HARVARD UNIVERSITY  
CAMBRIDGE, MASSACHUSETTS  
DECEMBER 2016

© 2016 - LULU LIU  
ALL RIGHTS RESERVED.

## *A Floating Probe Force Microscope with Sub-Femtonewton Resolution*

### ABSTRACT

Forces below the 1 fN level are highly relevant at the forefront of optics, in studies of biological processes, and in the design and actuation of optomechanical devices. Conventional force spectroscopy methods, including AFMs, have limited to a resolution of piconewtons or hundreds of femtonewtons what is measurable in these systems. A new class of promising force microscopes, utilizing a floating, optically trapped probe, have thusfar been unable to achieve thermally limited measurements.

We design and demonstrate an instrument proven to improve force sensitivity in fluid by more than two orders of magnitude over current techniques. Our instrument, with sub-femtonewton resolution, is fully capable of scanning and positioning similar to a traditional AFM. Along with the expanded science capabilities that come with a dramatic improvement in instrument sensitivity, our position tracking methods, with resolution down to the angstrom level, open up new areas of study in the detailed dynamics of optically driven microspheres.

# Contents

<b>1</b>	<b>LIGHT-MATTER INTERACTION</b>	<b>1</b>
1.1	Why does light interact with matter? . . . . .	2
1.2	Optical forces . . . . .	3
1.3	Optical tweezers . . . . .	5
1.4	Mie theory . . . . .	6
1.5	The Rayleigh approximation . . . . .	11
1.6	The Maxwell stress tensor . . . . .	11
<b>2</b>	<b>THERMAL MOTION</b>	<b>14</b>
2.1	Perrin's argument for atoms . . . . .	15
2.2	Einstein's kinetic theory of Brownian motion . . . . .	17
2.3	The Fluctuation-Dissipation Theorem . . . . .	18
2.4	Langevin equation of motion . . . . .	19
2.5	Mean-squared displacement . . . . .	26
2.6	Reynold's number . . . . .	26
<b>3</b>	<b>UNDERSTANDING NOISE</b>	<b>29</b>
3.1	What is noise? . . . . .	30
3.2	Propagation of error . . . . .	32
3.3	Turning down the noise . . . . .	33
<b>4</b>	<b>FORCE MICROSCOPY</b>	<b>37</b>

4.1	Why measure femtonewton forces? . . . . .	38
4.2	Atomic Force Microscope . . . . .	39
4.3	Floating Probe Microscope . . . . .	42
<b>5</b>	<b>PARTICLE TRACKING WITH A CALIBRATED EVANESCENT WAVE</b>	<b>48</b>
5.1	Experiment . . . . .	49
5.2	Two experimental results . . . . .	55
5.3	Conclusions . . . . .	62
<b>6</b>	<b>THERMALLY-LIMITED SUB-FEMTONEWTON RESOLUTION FORCE MI-</b>	
	<b>CROSCOPY</b>	<b>63</b>
6.1	Introduction . . . . .	64
6.2	Force measurement with a compliant probe . . . . .	65
6.3	Optical force on a sphere in an evanescent field . . . . .	66
6.4	Setup . . . . .	67
6.5	Data acquisition and analysis . . . . .	69
6.6	Results . . . . .	70
6.7	Conclusion . . . . .	73
<b>7</b>	<b>ELLIPTICAL MOTION OF MICROSPHERES IN AN EVANSCENT FIELD</b>	<b>89</b>
7.1	Introduction . . . . .	90
7.2	Forces on a driven, trapped microsphere . . . . .	91
7.3	Results . . . . .	95
7.4	Conclusion . . . . .	100
<b>8</b>	<b>APPENDIX</b>	<b>117</b>
8.1	Components . . . . .	118
8.2	Set-up and Alignment . . . . .	121
8.3	Fiber Coupling . . . . .	139
8.4	Microfluidic Sample Chambers . . . . .	143
8.5	Pump Beam Focusing . . . . .	144
8.6	Phase Calibration . . . . .	146

8.7 Labview Control Software . . . . . 147

REFERENCES 158

# Listing of figures

1.2.1 Simple dipole drawing . . . . .	4
1.3.1 Ashkin's 1986 image of an optically trapped microparticle . . . . .	6
1.4.1 Mie scattering geometry . . . . .	7
2.1.1 Sketch from Perrin's 1909 paper . . . . .	16
2.3.1 Sketch of brownian motion at a molecular level . . . . .	18
2.4.1 Power spectral density of a free Brownian particle . . . . .	21
2.4.2 Schematic of an optically trapped microsphere . . . . .	22
2.4.3 Power spectral density of an optically trapped Brownian particle	23
2.4.4 Dynamic regimes of an optically trapped Brownian particle . . .	24
2.4.5 Low-mass approximation for power spectral density . . . . .	25
2.6.1 Low Reynold's number swimmer . . . . .	27
3.1.1 Gaussian distribution . . . . .	31
3.3.1 Power spectrum and RMS noise . . . . .	34
4.1.1 Formation of DNA loops regulated by fN forces . . . . .	38
4.2.1 SEM image of an AFM cantilever . . . . .	40
4.2.2 Cantilever of an atomic force microscope . . . . .	41
4.3.1 Schematic of an optical tweezer . . . . .	43
4.3.2 Probability density function from Prieve's 1990 paper . . . . .	45
4.3.3 Potential profiles from Prieve's 1990 paper . . . . .	45

5.1.1	TIRM set-up . . . . .	50
5.1.2	Calibration curves with and without AR Coating . . . . .	52
5.1.3	Calibration curves relation to Debye length . . . . .	54
5.2.1	Calibration curves as a function of probe beam angle . . . . .	56
5.2.2	Measured and predicted near-wall hindered diffusion . . . . .	60
5.2.3	Potential energy profiles measured with 4 trap powers . . . . .	61
6.4.1	Experimental set-up: fN forces measurement . . . . .	68
6.4.2	Power spectral density (PSD) of a Brownian probe . . . . .	70
6.6.1	Force resolution of floating probe measurements . . . . .	71
6.6.2	Agreement between measurements and Mie theory . . . . .	72
6.7.1	Least-squares fit to MSD . . . . .	77
6.7.2	Spring constant of optical trap . . . . .	78
6.7.3	Numerical simulations confirming Mie theory approximation . .	88
7.2.1	Optically trapped sphere in its anisotropic environment . . . . .	94
7.3.1	Elliptical orbits of trapped microspheres, varying frequency . . .	96
7.3.2	Elliptical orbits of trapped microspheres, varying radius . . . . .	97
7.3.3	Measured and predicted torque applied to fluid . . . . .	99
7.4.1	Setup of 2D measurement . . . . .	102
7.4.2	Analysis flow for determination of unknown mechanical parameters	103
7.4.3	Power spectral density in 2D . . . . .	104
7.4.4	Damping coefficients perpendicular and parallel to wall . . . . .	105
7.4.5	Trap stiffness in the two directions . . . . .	107
7.4.6	Net force on an microparticle in elliptical orbit . . . . .	108
7.4.7	Optical forces in an evanescent field . . . . .	111
7.4.8	Angular momentum in microsphere undergoing elliptical motion	116
8.0.1	Force microscope in operation . . . . .	118
8.1.1	CAD Drawing of objective and prism assembly . . . . .	120
8.2.1	Optical paths and equipment on top level . . . . .	122
8.2.2	45 degree mirror . . . . .	123

8.2.3	Photo of LED beam path . . . . .	125
8.2.4	Photo demonstrating how to find objective focus . . . . .	126
8.2.5	Dark-field microscope image of PS beads . . . . .	127
8.2.6	Photo showing capacitive sensor attachment . . . . .	128
8.2.7	Photo showing alignment of beam expander . . . . .	130
8.2.8	Photo of probe beam configuration . . . . .	132
8.2.9	Photo of confocal collection scheme . . . . .	133
8.2.10	Photo of pump beam optics . . . . .	135
8.2.11	Schematic of a QPD . . . . .	136
8.2.12	Photo showing back-scattered trap beam . . . . .	137
8.2.13	Photo of balanced detector and optics . . . . .	138
8.3.1	Photo showing fiber coupling alignment . . . . .	140
8.4.1	Microfluidic chamber . . . . .	142
8.4.2	Drawing of coverslip with laser drilled holes . . . . .	143
8.4.3	Drawing of sealant cut into shape . . . . .	143
8.4.4	Drawing of assembled microfluidic chamber . . . . .	144
8.4.5	Photo of microfluidic chamber . . . . .	145
8.5.1	Microscope image of pump beam spot . . . . .	146
8.7.1	Custom Labview Control Front Panel . . . . .	148

FOR MY GRANDMOTHER, WHO DIED THIS YEAR. THIS IS WHY I DIDN'T COME  
VISIT MORE OFTEN. I'M SORRY. I MISS YOU.

# Acknowledgments

THE LIST INCLUDES MY PI, OF COURSE, and Alex Woolf, Simon Kheifets, Vincent Ginis, Andrea Di Donato, Zhang Wu, Brandon Foley, and Arman Amirzhan. To my advisor and scientific collaborators: thank you for your contributions to this project. It was a joy to work with you.

There are also those who have been very helpful in their capacity as university staff. Stacia Zatsiorsky and Deni Peric, our lab's administrators, Philippe de Rouffignac and Jason Tresback from the Center for Nanoscale Systems (CNS), are all very good at their jobs and deserve raises and promotions and more time off.

An even larger circle of colleagues and acquaintances have lent their help and their time out of sheer kindness. Some—Mikhail Kats, Sorel Massenburg, Tom Kodger, Max Eggersdorfer—taught me skills, some—David Siegel, Keith Karasek—offered advice. Thank you for your time; you're examples to me.

To my parents who thought it would be a good idea for me to go back to school—thanks for the encouragement. To Eric Betzig who asked me why I was wasting my time with my original dissertation project—thanks for the cold water.

*So how, children, does the brain, which lives without a spark  
of light, build for us a world full of light?*

Anthony Doerr

# 1

## Light-Matter Interaction

TO SEE THE WORDS on this page, to feel the sun on your skin, is to experience the interaction of light with matter. Light and matter are so present in our lives that, without study, most of us know quite a lot about these interactions. For instance, we know that trees cast shadows and these shadows are dark. We can't see through lead but we can see through air. A mirror shows our reflection but not a piece of paper.

To catalog the ways in which light and matter interact, and to predict, measure, and design these interactions to serve a specific purpose, is the general study of optics. In this chapter I hope to explain broadly some common features of light-matter interactions, then go into more detail about phenomena most relevant to this work.

## 1.1 WHY DOES LIGHT INTERACT WITH MATTER?

Atoms are electrically neutral, but their parts are not. Apply a voltage, or electric field, to a conducting material and something happens – a current of electrons begins to flow.

For an insulating material, the change is more subtle. Nevertheless, electron clouds deform in response to the field and the loss of symmetry causes the atom to become slightly polarized.

A linear material is the simplest, most familiar type. As long as the field is small, the induced polarization per unit volume in these materials is proportional to the electric field. That is,

$$\vec{P} \propto \vec{E} \quad (1.1)$$

The constant of proportionality is determined by the electric susceptibility,  $\chi_e$ , of the material— just how readily it polarizes compared to other materials under a certain applied field.

*Light* is an oscillating, propagating, electromagnetic field. When it strikes a material, the atoms that compose it feel an electric field and a magnetic field, which are quickly changing in direction. Its response, or its electric susceptibility, depends on both the composition of the material and the frequency of oscillation of these fields.

THE RESULT OF LIGHT STRIKING MATTER is that light can be absorbed, confined, scattered, or even emitted.

Absorption occurs when the energy of a photon goes into altering the state of matter in some way. For instance, if an electron is ionized or ejected from an atom, or if it is simply promoted to a higher energy level. This energy may be re-emitted as a photon—say, the electron recombines with the atom or drops back down to the lower energy state—or it may become thermal energy raising the temperature of the material.

Our skin, like most other parts of our body, is composed mainly of water. Water, a molecule with a permanent dipole, stretches and rotates in the presence of an electric field. Infrared light excites a number of these vibrational *modes*, so in effect, the energy of the photon is converted into kinetic, or thermal energy. It is because of absorption that sunlight feels hot on our skin.

In scattering, light encounters matter and is deflected from its original direction of travel. It may be redirected to travel in largely the same direction, a completely new direction, or in many directions at once. The difference in scattering phenomena explains the different visual experiences of looking through a piece of glass, seeing your reflection in a mirror, and staring at a blank piece of paper.

Multiple reflections or total internal reflection may cause photons to become "trapped" for some time in a limited spatial region. Optical confinement can refer to waveguides or micro-cavities or even defects within a photonic crystal [36]. These effects, along with stimulated emission phenomena where the presence of a photon induces matter to emit more photons with the same wavelength and phase [20], are a bit outside of common intuition and experience. But they are nevertheless important for everyday technologies. For instance, stimulated emission is a key physical process in the workings of a laser, and fiber-optic cables which allow Internet communication are waveguides which confine and transmit light pulses over long distances with minimal loss.

## 1.2 OPTICAL FORCES

The easiest way to understand how a force may arise from light-matter interactions is to consider a single dipole,  $\vec{p}$ . A dipole moment is formed by the spatial separation of a positive charge from an equal magnitude negative charge. Polarization refers to the creation of such a dipole moment in matter.

$$\vec{p} = q\vec{d} \tag{1.2}$$

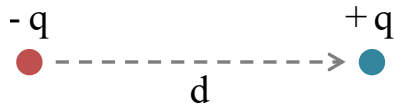


**Figure 1.2.1:** Drawing of a dipole moment.

The dipole may be permanent, such as in the case of water molecules, or induced. Induced dipoles follow the relation in Equation 1.1 for linear materials, with  $\vec{p} \propto \vec{E}$ .

Consider such a dipole, for example Figure 1.2.1, whether it is permanent or induced, in an electric field.  $\vec{E}$  is pointed in some direction which forms an angle  $\theta$  with  $\vec{d}$ . An electrostatic force will pull the positive charge in the  $\hat{E}$  direction and push the negative charge in the  $-\hat{E}$  direction, which in general results in a torque,  $\tau$ , on the dipole.

$$\vec{\tau} = \vec{p} \times \vec{E} \quad (1.3)$$

This torque goes to zero when  $\vec{d}$  becomes parallel to the electric field, so it can be intuitively understood that an electric field rotates the dipole to align with the field.

In this case, in a constant electric field, there is no *net force* on the dipole since the force on the negative charge is exactly equal and opposite to the force on the positive charge. If field strength varies from position to position, however, this is no longer the case. Consider a dipole which lies along the x-axis,

$$\begin{aligned} \vec{F}_{net} &= \vec{F}_+ + \vec{F}_- = q(\vec{E}(x_o + d) - \vec{E}(x_o)) \\ &= qd \frac{d\vec{E}}{dx} \Big|_{x=x_o}, \end{aligned}$$

where, in the last line,  $d$  was approximated to be very small. The result is the net force is proportional to the gradient of the electric field multiplied by the dipole moment. This can be generalized in three dimensions as

$$\vec{F}_{net} = (\vec{p} \cdot \vec{\nabla}) \vec{E} \quad (1.4)$$

For an induced dipole, where  $\vec{p}$  is itself proportional to  $\vec{E}$ , the net force can be re-written, using a vector calculus identity for  $\vec{\nabla}(\vec{A} \cdot \vec{B})$ , to be proportional to the gradient of the intensity of the electric field.

$$\vec{F}_{net} = \frac{1}{2} \vec{\nabla}(\vec{p} \cdot \vec{E}) = \frac{1}{2} \alpha \vec{\nabla} E^2 \quad (1.5)$$

THE ABOVE CALCULATIONS PROVIDE a kind of crude intuition for what we will later call the *gradient force*. Another way of understanding this force is that the dipole tends to move into a configuration which would *minimize energy*.

Equation 1.5 shows that the net force may be written as a gradient of some quantity. This implies the force is conservative and that this quantity is the negative of a potential energy, where,

$$U = -\frac{1}{2} \vec{p} \cdot \vec{E} = -\frac{1}{2} \alpha E^2 \quad (1.6)$$

The lowest energy configuration occurs when the dipole moment is aligned with the electric field in the region of highest field. A similar argument may be made for permanent dipoles. Since most materials are polarizable, this tendency to be attracted to electric field maxima would be exploited in the creation of optical tweezers.

### 1.3 OPTICAL TWEEZERS

In 1986, Arthur Ashkin and his colleagues at Bell Labs demonstrated the first working optical tweezer [8], composed of a single, focused laser beam, and capable of capturing and holding in place microparticles ranging from nanometers to microns in size.

The simple system was modeled in the context of separate gradient and scattering forces: the former acting to pull the particle towards the highest

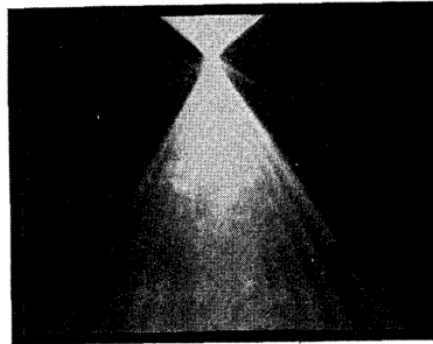


**Figure 1.3.1:** Ashkin's 1986 microscope image of an optically trapped microsphere, showing, in the striations, the distinctive Mie scattering interference orders.

intensity region and the latter pushing the particle in the direction of light propagation. The physical explanation was given in two regimes. First, the dipolar regime was explored where the particle is approximated to be a point particle much smaller than the wavelength of light. Then, a ray optics picture was offered where the refraction of light by a particle much larger than its wavelength results in a change of momentum that causes an attractive force.

Though the explanations give a useful intuition, microparticles in general, including those used in the Ashkin experiment, fall into neither of the above categories [74]. The appropriate treatment is one using wave optics, but accounting for the finite size of the scatterer. This approach, named Mie theory, is an exact scattering solution generally applicable to spherical particles interacting with an electromagnetic field.

#### 1.4 MIE THEORY

A signature of Mie scattering is the emergence of morphology-dependent electromagnetic resonances which occur for particles of particular radii. These are to be distinguished from optical resonances due to the material's intrinsic response to light of different frequencies, reflected in the material's optical constants.

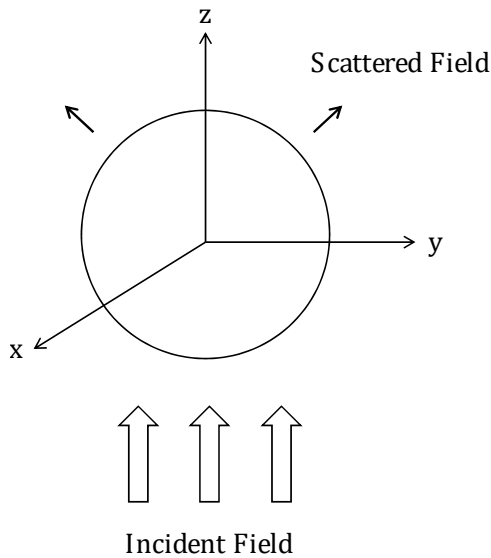


**Figure 1.4.1:** Mie scattering geometry showing spherical particle, incident and scattered fields.

In its simplest form, Mie theory imagines a plane wave incident on a sphere. The oscillating fields induce a polarization within the sphere which varies with time and position. Oscillating charges and dipoles radiate and a scattered field results, which propagates radially outward from the sphere. The superposition of the incident and scattered fields give the distinctive Mie scattering interference pattern in the far-field, visible in Figure 1.3.1.

THE PROBLEM CAN BE SOLVED in three steps. First, obtain a set of generic solutions to Maxwell's wave equations which form a complete orthonormal basis in the spherical coordinate system. Second, express the incident, scattered, and internal fields in terms of these solutions. Third, solve for the unknown parameters in these fields by imposing boundary conditions derived from Maxwell's Equations.

For a full discussion, the Bohren and Huffman text [13] is recommended. Below is this procedure in brief.

#### 1.4.1 STEP ONE: VECTOR SPHERICAL HARMONICS

The homogeneous wave equations for electric and magnetic fields in the absence of sources reads,

$$\begin{aligned}\nabla^2 \vec{E} + k^2 \vec{E} &= 0 \\ \nabla^2 \vec{B} + k^2 \vec{B} &= 0\end{aligned}\tag{1.7}$$

where  $k^2 = \epsilon\mu\omega^2$ , and time-harmonic, monochromatic solution of the form  $\vec{E} = \vec{E}_0(x, y, z)e^{-i\omega t}$  have been inserted. Here,  $\epsilon$  and  $\mu$  indicate the optical properties of the medium –  $\epsilon$  is the *electric permittivity* and  $\mu$  the *magnetic permeability* – and  $k$  is the wavevector in the medium.

Presented without derivation are the *Vector Spherical Harmonic* solutions which obey the vector wave equations in 1.7 as well as the individual Maxwell's equations,

$$\vec{M}_{l,m} = \vec{\nabla} \times (\vec{r} \psi_{l,m}) \tag{1.8}$$

$$\vec{N}_{l,m} = \frac{\vec{\nabla} \times \vec{M}_{l,m}}{k}, \tag{1.9}$$

with

$$\psi_{l,m}(r, \theta, \varphi) = \sqrt{\frac{2}{\pi}} Z_l(kr) P_l^m(\cos \theta) e^{im\varphi}. \tag{1.10}$$

In these equations, the indices  $l, m$  are integers, with  $l \geq 0$  and  $|m| \leq l$ . The function  $Z_l$  represents a *Spherical Bessel Function* and  $P_l^m$  are the set of *Associated Legendre Polynomials*.

The solutions form a complete orthonormal set, and thus, any solution of the wave equation satisfying Maxwell's Equations may be written as a linear combination of these functions.

#### 1.4.2 STEP TWO: REAL FIELDS AS SPHERICAL HARMONICS

An operator,  $A$ , is *linear* if its action on a superposition of functions  $(a_1 f_1 + a_2 f_2 + \dots)$  can be written as its action on each individual part such that,

$$A(a_1 f_1 + a_2 f_2 + \dots) = a_1 A(f_1) + a_2 A(f_2) + \dots \quad (1.11)$$

where  $a_i$  are constants.

The linearity of Maxwell's Equations allows separate solutions found for incident and scattered fields to be superimposed in each region of space. The total field, guaranteed to also be a solution to Maxwell's Equations, is then connected across regions by boundary conditions.

Any electromagnetic field can theoretically be written in terms of the spherical harmonics discussed in the previous section.

$$\vec{E}_{inc} = \sum_{l,m} \left[ a_{l,m} \vec{N}_{l,m} + \beta_{l,m} \vec{M}_{l,m} \right] \quad (1.12)$$

Since the incident field is known, the coefficients  $a_{l,m}$  and  $\beta_{l,m}$  can be computed directly. The incoming magnetic field may be found by taking the curl of this expression, so no new coefficients are necessary to write  $\vec{H}_{inc}$ .

A similar expression can be written for the scattered field,  $E_{scat}$  and the field inside the particle,  $E_{int}$ .

$$\vec{E}_{scat} = \sum_{l,m} \left[ a_{l,m} \vec{N}_{l,m} + b_{l,m} \vec{M}_{l,m} \right] \quad (1.13)$$

$$\vec{E}_{int} = \sum_{l,m} \left[ c_{l,m} \vec{N}_{l,m} + d_{l,m} \vec{M}_{l,m} \right] \quad (1.14)$$

Since  $E_{inc}$  is often simply expressed in Cartesian coordinates, e.g. a monochromatic plane wave, it may seem counterproductive to recast these fields in spherical harmonics. However, by respecting the spherical geometry of our scatterer, we make the last step, matching the boundary conditions, very straight-forward.

### 1.4.3 STEP THREE: BOUNDARY CONDITIONS

Boundary conditions derived from Maxwell's Equations govern the behavior of electromagnetic fields crossing from one medium into another. They are phrased in relation to the interface normal direction,  $\hat{n}$ , which, in the case of a sphere with its center at the coordinate origin, is the  $\hat{r}$  direction.

It becomes clear that complex manipulations of the previous sections have the purpose of simplifying this matching procedure. The total fields on the interior of the Mie particle are related to the total fields in the surrounding medium by

$$\begin{aligned}\hat{r} \times (\vec{E}_{out} - \vec{E}_{in}) &= 0 & \hat{r} \cdot (\epsilon_{out} \vec{E}_{out} - \epsilon_{in} \vec{E}_{in}) &= 0 \\ \hat{r} \times (\mu_{out} \vec{B}_{out} - \mu_{in} \vec{B}_{in}) &= 0 & \hat{r} \cdot (\vec{B}_{out} - \vec{B}_{in}) &= 0,\end{aligned}\quad (1.15)$$

assuming no "free" surface charges and currents exist. *Incidentally, these boundary conditions also work for scatterers which are electrical conductors, as long as the free electron contribution to the polarization is included in a complex dielectric function,  $\tilde{\epsilon}$ .*

Replacing  $\vec{E}_{out} = \vec{E}_{scat} + \vec{E}_{inc}$  and  $\vec{E}_{in} = \vec{E}_{int}$ , and similarly for  $\vec{B}$ -fields, the coefficients may be matched order by order resulting in exceptionally complex expressions for  $a$ ,  $b$ ,  $c$ , and  $d$ , which I will not quote here.

Two important points should be noted which will become important later on.

First, the Mie scattering solution is an infinite series. Its convergence depends on a diminishing contribution from scattering at higher orders. It becomes necessary in a practical calculation to truncate the series at a certain order, given an acceptable margin of error. As the Mie particle becomes larger relative to the wavelength, contributions from higher orders grow in importance, thus, Mie theory calculations are limited in a practical sense.

Second, the result of a Mie scattering calculation is the analytical expression of the electromagnetic field over all space given a specific scattering configuration. Quantities of physical importance, such as the optical force on the scatterer, the differential and total scattering cross-sections, the absorption and extinction cross-sections, etc, must be calculated based on these fields. In Section 1.6 I

discuss the framework for calculating optical forces from electromagnetic fields.

## 1.5 THE RAYLEIGH APPROXIMATION

Mie theory gives the generalized scattering solution for all particle sizes and all wavelengths of light. In the limit of small particles, however, the much simpler dipolar solution, as discussed in Section 1.2 may be recovered through an approximation.

Two criteria must be met. The particle radius must be much smaller than the wavelength of light ( $ka \ll 1$ ), and the index of refraction of the scatterer must be close to that of the medium ( $n_s/n_m \approx 1$ ). In this case, the Mie infinite series may be approximated by the first (dipolar) term, with  $l = 1$ . For an incident, linearly polarized plane wave, all coefficients with  $m \neq 1$  are zero, and the only scattering coefficients to be considered are  $a_{1,1}$  and  $b_{1,1}$ . This greatly simplifies the calculations, and results in the familiar Rayleigh scattering cross-section which is proportional to the fourth power of the frequency of light,

$$\begin{aligned}\sigma_{scat} &= \frac{6\pi}{k^2} \left[ \frac{4(ka)^6}{9} \left| \frac{(n_s/n_m)^2 - 1}{(n_s/n_m)^2 + 2} \right|^2 \right] \\ &= \frac{k^4}{6\pi} |\alpha|^2,\end{aligned}\tag{1.16}$$

where  $\alpha$  is the complex polarizability of the sphere, defined as  $\alpha = 3V\frac{N^2-1}{N^2+2}$ .  $V$  is the volume of the sphere.

## 1.6 THE MAXWELL STRESS TENSOR

Electromagnetic waves carry momentum. When light is scattered by a particle, some portion of it is redirected from its original path, that is, its momentum is altered. The scatterer therefore feels a recoil force due to the conservation of momentum.

*But what is this recoil force acting on, exactly?*

Recall that, in Section 1.1, we discussed the reason that light interacts with matter—matter is made up of positive and negative charges. Imagine one of these charges inside the scatterer, immersed in an electromagnetic field, perhaps the total field calculated in Section 1.4. Force on this charge, at a specific moment in time, given by the Lorentz force law, is

$$\vec{F} = q(\vec{E} + \vec{v} \times \vec{B}). \quad (1.17)$$

We could calculate the total force on the scatterer by finding the force on each individual charge, but it is often easier to work with fields. Using Maxwell's Equations to replace the charge in Equation 1.17 with the fields produced by the presence of the charge, and integrating over all charges, the total force (in each direction) can be written [30],

$$F_i = \oint_S T_{ij} \cdot da_j - \epsilon\mu \frac{d}{dt} \int_V S_i dV, \quad (1.18)$$

where

$$T_{ij} \equiv \epsilon \left( E_i E_j - \frac{1}{2} \delta_{ij} E^2 \right) + \frac{1}{\mu} \left( B_i B_j - \frac{1}{2} \delta_{ij} B^2 \right) \quad (1.19)$$

is the Minkowski form of the *Maxwell Stress Tensor* [38]<sup>1</sup>. The indices  $i, j$  span the three dimensions,  $\delta_{ij}$  is the Kronecker delta, and  $\vec{S}$  is the Poynting vector of the electromagnetic field. Using the relation between the Poynting vector and the momentum density of an EM field,  $\vec{\rho}_{em} = \vec{S}/c^2$ , Equation 1.20 may be rewritten,

$$\frac{d}{dt} (P_{mech,i} + P_{em,i}) = \oint_S T_{ij} \cdot da_j \quad (1.20)$$

where  $F_i = \frac{dP_i}{dt}$  has been used, and  $P_{mech}$  and  $P_{em}$  represent the total momentum of the charges and fields, respectively, within the volume.

In this form, this equation is clearly an expression of conservation of

---

<sup>1</sup>The correct form of the Maxwell Stress Tensor in magnetic dielectric media, and how it ought to be used, has been a source of controversy for some time. For more about this problem, see [46].

momentum. In words, the change in total momentum—of charges and fields—within a volume is equal to the rate of momentum "flow" into that volume.

In a steady-state problem, the fields are unchanging, and  $\frac{d}{dt}P_{em}$  may be neglected. So it can be interpreted that by reading the change in momentum of the EM field, one can infer the force on the scatterer within.

Generalized to time-averaged quantities of oscillating fields, as in the case of light where  $E_i(t) = \tilde{E}_i e^{i\omega t}$  and  $B_i(t) = \tilde{B}_i e^{i\omega t}$ , the Maxwell Stress tensor is, quite similarly,

$$\langle T_{ij} \rangle = \frac{1}{2} \left[ \epsilon \left( \tilde{E}_i \tilde{E}_j^* - \frac{1}{2} \delta_{ij} |E|^2 \right) + \frac{1}{\mu} \left( \tilde{B}_i \tilde{B}_j^* - \frac{1}{2} \delta_{ij} |B|^2 \right) \right] \quad (1.21)$$

where the overall factor of  $1/2$  has appeared because  $\langle \cos^2(\omega t) \rangle = 1/2$ .

*Repose is only an illusion due to the imperfection of our senses.*

Jean Baptiste Perrin

# 2

## Thermal Motion

WHEN JEAN BAPTISTE PERRIN WAS, IN 1926, awarded the Nobel Prize in Physics for his work on Brownian motion, the prize credited his discovery of *the discontinuous structure of matter*. This is the lesser known story of the atom, but in fact, the prediction and measurement of thermal motion had settled a great debate.

The turn of the nineteenth century brought to physics a wave of new ideas. Classical thermodynamics, which had enjoyed much success in its energetic description of nature, met a new challenger in the form of molecular kinetic theory. That matter could be granular was not a brand new idea—chemists since John Dalton had been using the theoretical construct of atoms—but it was not believed to be any more than a mathematical tool.

The new kinetic theory, however, presupposed the physical reality of atoms

and molecules and aimed to describe thermodynamics through their statistical, ensemble behavior. The first experimental validation of this theory, which finally put to rest the concept of continuous, infinitely divisible matter, came in 1909, and was a measurement of Brownian motion.

## 2.1 PERRIN'S ARGUMENT FOR ATOMS

Translated from Perrin's 1909 paper *Brownian Motion and Molecular Reality* [56] is this thought experiment:

What is really strange and new in the Brownian movement is, precisely, that it never stops. At first that seems in contradiction to our every-day experience of friction. If for example, we pour a bucket of water into a tub, it seems natural that, after a short time, the motion possessed by the liquid mass disappears. Let us analyse further how this apparent equilibrium is arrived at: all the particles had at first velocities almost equal and parallel; this co-ordination is disturbed as soon as certain particles, striking the walls of the tub, recoil in different directions with changed speeds, to be soon deviated anew by their impacts with other portions of the liquid. So that, some instants after the fall, all parts of the water will be still in motion, but it is now necessary to consider quite a small portion of it, in order that the speeds of its different points may have about the same direction and value...

What we observe, in consequence, so long as we can distinguish anything, is not a cessation of the movements, but that they become more and more chaotic, that they distribute themselves in a fashion the more irregular the smaller the parts.

Does this de-co-ordination proceed indefinitely?

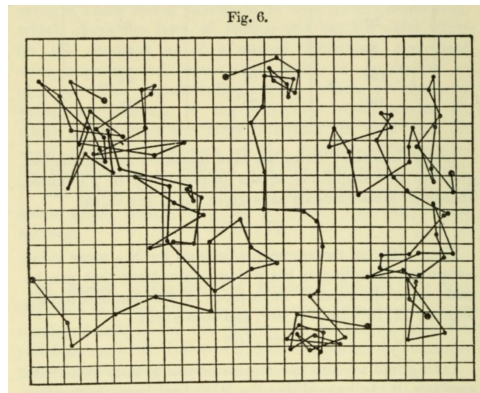


**Figure 2.1.1:** Sketch of Brownian motion from Perrin's 1909 paper.

The results of his experiment—the observation of Brownian motion—is itself the answer to this question: no. He goes on to make a logical argument for discrete matter on this basis.

Since the distribution of motion in a fluid does not progress indefinitely, and is limited by a spontaneous re-co-ordination, it follows that the fluids are themselves composed of granules or molecules, which can assume all possible motions relative to one another, but in the interior of which dissemination of motion is impossible. If such molecules had no existence it is not apparent how there would be any limit to the de-co-ordination of motion...

The Brownian movement is permanent at constant temperature: that is an experimental fact. The motion of the molecules which it leads us to imagine is thus itself also permanent. If these molecules come into collision like billiard balls, it is necessary to add that they are perfectly elastic, and this expression can, indeed, be used to indicate that in the molecular collisions of a thermally isolated system the sum of the energies of motion remains definitely constant.

**In brief the examination of Brownian movement alone suffices**

**to suggest that every fluid is formed of elastic molecules,  
animated by a perpetual motion.**

## 2.2 EINSTEIN'S KINETIC THEORY OF BROWNIAN MOTION

The success of Perrin's 1909 experiment is largely the agreement of its quantitative results with a prediction made by Albert Einstein in 1905 – and independently, by Marian Smoluchowski in 1906 – based on molecular kinetic theory [19].

Einstein's key insight was that a microscopic particle undergoing Brownian motion differed from a solute molecule dissolved in a liquid only by its dimensions. As such, a collection of Brownian particles would be expected to exhibit its own osmotic pressure.

By incorporating the mobility ( $\mu = 1/\gamma$ ) of these individual particles in calculating a drift current due to osmotic pressure, Einstein derived an expression for the diffusion coefficient,  $D$ , in Fick's Laws, which had been previously left as an empirical quantity:

$$D = k_B T \mu \quad (2.1)$$

or, if the particle could be approximated as a sphere,

$$D = \frac{k_B T}{6\pi\eta R} \quad (2.2)$$

where  $k_B$  is the Boltzmann constant,  $T$  is the temperature in Kelvin,  $\eta$  the viscosity of the fluid medium and  $R$  the radius of the diffusing body.

Recognizing, also, that the key measurable quantity in Brownian motion is the mean-squared-displacement, rather than the velocity, Einstein derived the additional relation, for one-dimensional diffusion,

$$\langle \Delta x^2 \rangle = 2Dt, \quad (2.3)$$

stating that the absolute mean displacement of a Brownian particle in time  $t$  is

proportional to the square-root of time. This distinctive feature of a random walk enabled the quantitative comparison of Perrin's measurements with kinetic theory— the direct evidence needed to make the definitive case for the atom.

### 2.3 THE FLUCTUATION-DISSIPATION THEOREM

Einstein's equation (2.1) happened to be an early example of a fluctuation-dissipation relation. However, the idea would not be formalized until 1928, when Harry Nyquist reviewed the problem of thermal fluctuations in conductors in electrical circuits [54]. Then, only in 1951, came the proof for the general form of the fluctuation-dissipation theorem, which unified the law in all linear systems which obey microscopic reversibility [15].

The fluctuation-dissipation theorem, as its name implies, finds a fundamental connection between thermal fluctuations of a physical system and the system's dissipative qualities.

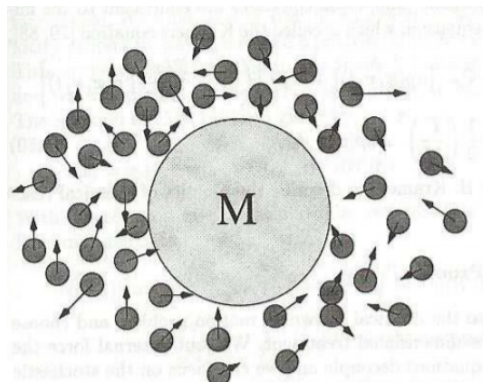


**Figure 2.3.1:** Sketch of brownian motion at a molecular level. [68]

Consider the case of a particle in a fluid. In thermal equilibrium the molecules of the fluid are striking, randomly, the particle from all sides. This has two distinct mechanical effects on the particle. First, the particle appears to move around in a random, jerky manner, that is, it undergoes Brownian motion. Second, the particle, if caused to move by some external stimulus, will feel an impedance—

due to collisions with these fluid molecules—tending to dissipate the energy of its motion and bring the particle to rest.

Since the two effects come from the same origin, it is not surprising that they are related. Or, in the language of Perrin's argument in the earlier section, in a system that is reversible, re-coordination (fluctuation) is simply the inverse of de-coordination (dissipation), facilitated by the same physical processes (collisions).

Specifically, it can be shown [15] that the thermal force power spectrum,  $S_F = |\tilde{F}_{th}(\omega)|^2$ , of Brownian motion of a particle is proportional to its drag coefficient  $\gamma$ . Thus, thermal noise increases with higher temperatures as well as more dissipation.

$$S_F = 2\gamma k_B T \quad (2.4)$$

Similarly, the power spectrum of fluctuations in an electrical circuit is related to the resistance of the circuit to current flow<sup>1</sup>.

## 2.4 LANGEVIN EQUATION OF MOTION

### 2.4.1 FREE MOTION

Though a particle undergoing Brownian motion moves in an essentially non-deterministic way, its motion can be accurately modeled using the familiar Newtonian dynamic equations. In the most simple case of unconstrained one-dimensional motion, the Langevin equation reads,

$$m \frac{dv(t)}{dt} = -\gamma v(t) + F_{th}(t) \quad (2.5)$$

where  $F_{th}$  is the stochastic thermal force, and  $v(t) = \frac{dx(t)}{dt}$ . The nature of a stochastic force ensures that any given instance of this force at time  $t$  cannot be

---

<sup>1</sup>The notion that a quantity proportional to the square of some variable would be called the *power spectrum* of that variable comes from electronics, where Power  $\propto V^2$

exactly known, however, statements can be made about its ensemble average values.

Since the particle is equally likely to be struck by a fluid molecule from either side, the average stochastic force should be zero. However, as explained in Section 2.3, the second moment of the distribution,  $\langle F_{th}(t)F_{th}(t') \rangle$  is non-zero and related to the drag,  $\gamma$ , by Equation 2.4. Thus, it can be shown that  $F_{th}$  has the following properties:

$$\langle F_{th}(t) \rangle = 0 \quad \langle F_{th}(t)F_{th}(t') \rangle = 2\gamma k_B T \delta(t - t'). \quad (2.6)$$

Here,  $\langle \dots \rangle$  is used to denote the ensemble average, and the delta-function ensures that each impulse is uncorrelated with every other.

From this very simple model one can already deduce some universal aspects of a particle's motion in fluid. Taking an average of Equation 2.5, and setting the mean stochastic force to its average value of zero, we obtain,

$$\langle v(t) \rangle = \langle v(0) \rangle e^{-\frac{\gamma}{m}t} \quad (2.7)$$

where  $\tau_p = m/\gamma$  emerges as an important time scale which we will call the *momentum relaxation time*. It can be understood as the time it takes for a particle to lose its ballistic momentum in the fluid. In other words, on time scales much longer than  $\tau_p$ , the particle behaves as if it has no inertial mass.

If we Fourier transform Equation 2.5 and rearrange to write the particle's motion  $\tilde{x}(\omega)$  in terms of the driving force  $\tilde{F}_{th}(\omega)$ , we obtain,

$$\tilde{x}(\omega) = \frac{\tilde{F}(\omega)}{m\omega^2 + i\gamma\omega} \quad (2.8)$$

and we may identify the complex quantity  $\chi(\omega) = \frac{1}{m\omega^2 + i\gamma\omega}$  as the *response function* of the linear system.

To examine the power spectral density (PSD), or power spectrum, of the

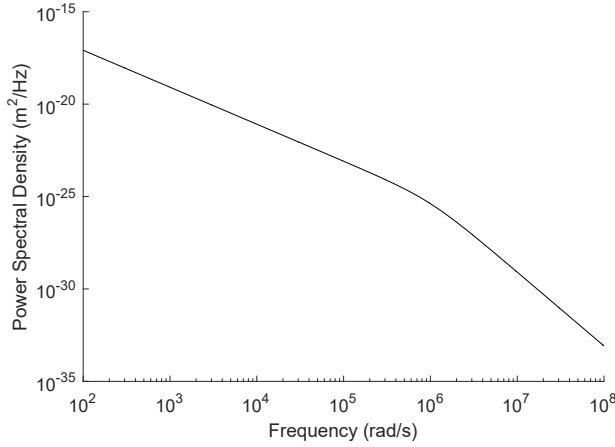


**Figure 2.4.1:** Power spectral density of a free Brownian particle in fluid with typical parameters:  $\gamma = 1 \times 10^{-7} \text{ N}\cdot\text{s}/\text{m}$ ,  $k_B T = 4 \times 10^{-21} \text{ J}$ ,  $\tau_p = 10^{-6} \text{ s}$

particle's position, recall  $S_x(\omega) = |\tilde{x}(\omega)|^2$ :

$$S_x(\omega) = \frac{S_F(\omega)}{m^2\omega^4 + \gamma^2\omega^2} = \frac{S_F}{\gamma^2\omega^2\left(\frac{\omega^2}{\omega_p^2} + 1\right)} \quad (2.9)$$

where  $S_F(\omega) = 2\gamma k_B T$  is a constant, as determined in the earlier discussion on fluctuations and dissipation. Two distinct regimes emerge, again, defined by their relationship to  $\tau_p = \omega_p^{-1}$ . First, on very short time scales, or  $\omega \gg \omega_p$ , the first term in the denominator dominates, and  $S_x$  is proportional to  $\omega^{-4}$ . The motion is ballistic. However, at time scales longer than  $\tau_p$ , where  $\omega \ll \omega_p$ , motion is diffusive and  $S_x$  is proportional to  $\omega^{-2}$ . Figure 2.4.1 shows this dependence.

#### 2.4.2 CONSTRAINED MOTION

Now consider a Brownian particle which is constrained to move inside a harmonic potential formed by an optical trap, as in Figure 2.4.2. We modify

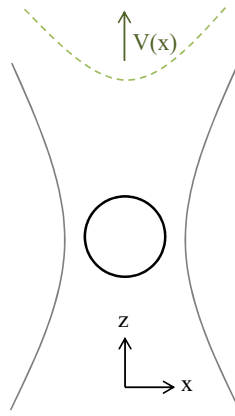


**Figure 2.4.2:** Schematic of an optically trapped microsphere. In green: an approximation of the harmonic trap potential.

Equation 2.5 with a new term accounting for the trap's restoring force,

$$m \frac{d^2x(t)}{dt^2} = -\kappa x - \gamma \frac{dx(t)}{dt} + F_{th}(t) \quad (2.10)$$

where the equation of motion is now expressed in terms of the position variable,  $x(t)$ , and  $\kappa$  represents the stiffness of the optical trap, or its *spring constant*.

The complex response function becomes,

$$\chi(\omega) = \frac{1}{\kappa - m\omega^2 + i\gamma\omega} \quad (2.11)$$

resulting in a Lorentzian expression for the power spectral density,

$$S_x(\omega) = \frac{S_F(\omega)}{m^2 \left[ (\omega_o^2 - \omega^2)^2 + \omega_p^2 \omega^2 \right]}. \quad (2.12)$$

The natural resonance  $\omega_o$  of the system was introduced and defined as  $\omega_o^2 = \kappa/m$ . Completing the square to put Equation 2.12 in a more familiar form,

$$S_x(\omega) = \frac{S_F(\omega)}{m^2 \left[ (\omega^2 - \omega_L^2)^2 + (\frac{1}{2}\Gamma)^2 \right]}, \quad (2.13)$$

we find that the Lorentzian has a peak centered around  $\omega_L = \sqrt{\omega_o^2 - \frac{1}{2}\omega_p^2}$ , with a width of  $\Gamma = 2\sqrt{\omega_o^4 - \omega_L^4}$ .

First, let's examine how the optical trap affects a typical microsphere in fluid. Figure 2.4.3 compares the power spectrum of the trapped sphere with that of the free sphere plotted in Figure 2.4.1.

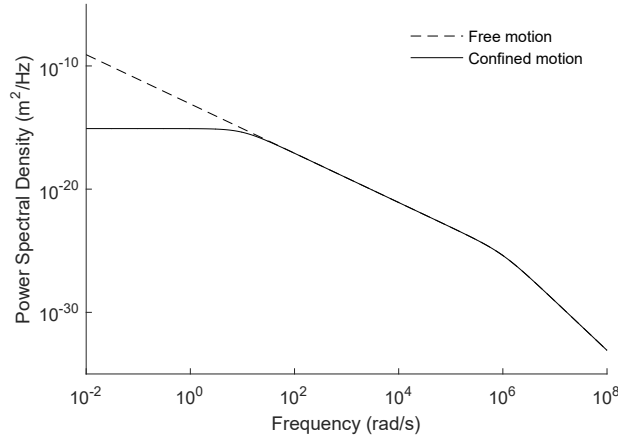


**Figure 2.4.3:** Power spectral density of an optically trapped Brownian particle in fluid compared with that of a free particle. Typical parameters were used:  $\gamma = 1 \times 10^{-7} \text{ N*s/m}$ ,  $k_B T = 4 \times 10^{-21} \text{ J}$ ,  $\tau_p = 10^{-6} \text{ s}$ ,  $\kappa = 1 \times 10^{-6} \text{ N/m}$ .

One can see immediately that on short time scales—i.e. at high frequencies—the motion of an optically trapped sphere is indistinguishable from that of a freely diffusing sphere. Intuitively, on short time scales, the Brownian particle does not "sense" the optical trap. On long time scales—at low frequencies—however, the motion is limited compared to that of a free particle. This can be understood as the optical trap imposing a sort of "cap" on the maximum mean-squared displacement.

Next, let's examine the different dynamical regimes potentially accessible by a trapped microsphere. To do this, we must change the relative values of the system's various time constants. Figure 2.4.4 shows the power spectrum of a microsphere in different fluid environments, or under varying  $\omega_p$  relative to a

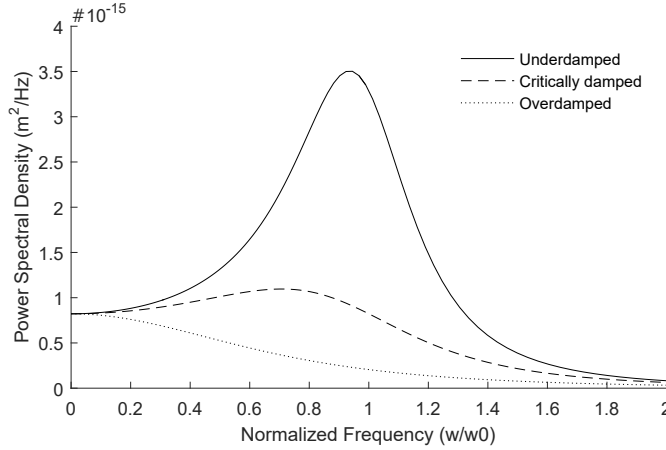


**Figure 2.4.4:** Power spectral density of an optically trapped Brownian particle in fluid, showing different dynamic regimes. Fixed parameters:  $k_B T = 4 \times 10^{-21}$  J,  $\kappa = 1 \times 10^{-6}$  N/m. Underdamped:  $\omega_p = 0.5\omega_0$ . Critically damped:  $\omega_p = \omega_0$ . Overdamped:  $\omega_p = 2\omega_0$ .

fixed  $\omega_0$ .

The three regimes are labeled *underdamped*, *critically damped*, and *overdamped* in analogy to the classic problem of a damped harmonic oscillator. A typical microsphere in a fluid environment corresponds to a  $\omega_p \approx 500\omega_0$  case, or a highly overdamped case. On the other hand, the viscosity of air is 100 times smaller than that of water, and a critically damped or even underdamped regime may be reached.

Since all measurements described in this document were made in a fluidic environment, we can focus on the highly overdamped case. This specialization allows us to make a few simplifying approximations. First, recall that  $\tau_p = m/\gamma$  defines the time scale for dissipation of inertia. Since  $\tau_p$  is on the order of a microsecond, instruments operating with sample rates on the order of kHz should be insensitive to the effect of particle mass. Testing this hypothesis, we eliminate the middle term in the denominator of Equation 2.11 to obtain,

$$\chi(\omega) = \frac{1}{\kappa + i\gamma\omega} \quad (2.14)$$

with a correspondingly simplified power spectrum,

$$S_x(\omega) = \frac{S_F(\omega)}{\gamma^2 \left[ \left( \frac{\kappa}{\gamma} \right)^2 + \omega^2 \right]}. \quad (2.15)$$

we can identify the quantity  $\kappa/\gamma$  as a corner frequency,  $\omega_c$ . At frequencies much larger than the corner frequency  $\omega \gg \omega_c$ , the power spectrum is proportional to  $\omega^{-2}$ . This is exactly the diffusive behavior discussed earlier. At frequencies much lower than the corner frequency, the power spectrum is a constant, and the motion is capped.

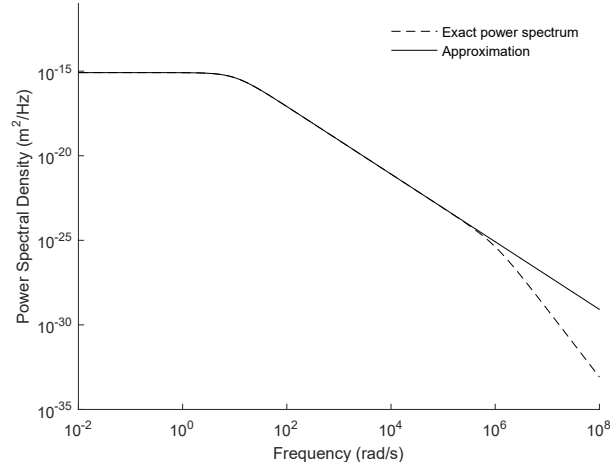


**Figure 2.4.5:** Power spectral density of an optically trapped Brownian particle in fluid, low-mass approximation compared with exact solution. Typical parameters were used:  $\gamma = 1 \times 10^{-7}$  N\*s/m,  $k_B T = 4 \times 10^{-21}$  J,  $\tau_p = 10^{-6}$  s,  $\kappa = 1 \times 10^{-6}$  N/m.

Figure 2.4.5 compares the exact power spectrum from Equation 2.12 with the low-mass approximation of Equation 2.15 for a typical spherical microparticle in fluid. The excellent agreement of the two expressions on time scales larger than the momentum relaxation time,  $\tau_p$ , allows the use of the low-mass approximation for the remainder of this work.

## 2.5 MEAN-SQUARED DISPLACEMENT

Though the *mean-squared displacement* (MSD) and the *power spectral density* (PSD) may look very different, they contain the same information about the dynamics of the system.

To see this, recall the alternate definition of the power spectral density as defined as the Fourier transform of the auto-correlation function,

$$G_x(\tau) = \langle x(t)x(t + \tau) \rangle,$$

$$S_x(\omega) = \frac{1}{\sqrt{2\pi}} \int_{-\infty}^{\infty} G_x(\tau) e^{-i\omega\tau} d\tau \quad (2.16)$$

The connection between the MSD and the autocorrelation function is straight-forward to derive. If  $\langle x(t) \rangle$  is zero, and setting  $t' = t + \tau$ ,

$$\begin{aligned} \langle \Delta x(\tau)^2 \rangle &= \langle (x(t') - x(t))^2 \rangle \\ &= \langle x(t')^2 \rangle - 2\langle x(t')x(t) \rangle + \langle x(t)^2 \rangle \\ &= 2\text{Var}(x) - 2G_x(\tau) \end{aligned} \quad (2.17)$$

Therefore, the mean-squared-displacement  $\langle \Delta x(\tau)^2 \rangle$  can be written in terms of the variance and power spectrum as,

$$\langle \Delta x(\tau)^2 \rangle = 2\text{Var}(x) - 2 \frac{1}{\sqrt{2\pi}} \int_{-\infty}^{\infty} S_x(\omega) e^{i\omega\tau} d\omega \quad (2.18)$$

Though the MSD and PSD contain the same information, occasionally it is more convenient to use one form over another, especially in performing least-square fits.

## 2.6 REYNOLD'S NUMBER

It is appropriate, in a discussion about Brownian dynamics of microparticles in fluid, to calculate the Reynolds number of such a system. The Reynold's number

in fluid dynamics is the ratio of inertial to viscous forces in the system, and as such, quantifies their relative importance.

$$Re = Rv\rho/\eta \quad (2.19)$$

$R$  is the dimension of the object moving with velocity  $v$  through fluid,  $\rho$  and  $\eta$  are the density and viscosity of the fluid, respectively.

Our daily experience exemplifies a high Reynold's number system. As an example, a human swimming in a pool of water will have a Reynold's number of about  $10^4$ . We might be surprised, therefore, to find that many of our physical intuitions do not carry over to low Reynold's number systems such as the ones in this study.

Objects moving in a low Reynold's number regime do not behave as if they have inertia [63]. An applied force induces almost instantaneous movement, and when the force stops, so does the motion.

There is no notion of "stirring" in the usual sense, either. Any mixing of fluids or particles in a low Reynold's number regime due to stirring can be "unmixed" by simply reversing the direction of agitation.

Finally, as will become applicable later, propulsion, or inversely, pumping, in such systems is governed by a different set of principles. These are principles of symmetry. Since there is no sense in propelling forward by "pushing" back on the fluid, propulsion is achieved only through configurational changes of a body that break time-reversal symmetry [63]. An example is given in Figure 2.6.1.

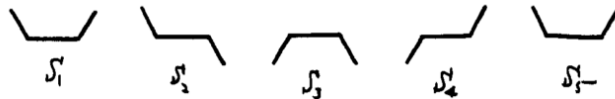


**Figure 2.6.1:** Example of a low Reynold's number swimmer from Purcell's *Life at Low Reynold's Number* [63]

The Reynold's number for our system of microparticles in water can be

estimated by comparison with a sort of *characteristic force*, which would pull any object through our medium with a Reynold's number of 1. For water, that force is 1 nanonewton, or  $1 \times 10^{-9}$  N. Since our target forces are in the femtonewton range, around six orders of magnitude smaller, our system is deep in the low Reynold's number regime.

*Go placidly amid the noise and the haste, and remember what  
peace there may be in silence.*

Max Ehrmann. *Desiderata*

# 3

## Understanding noise

IN FEBRUARY OF THIS YEAR, the Laser Interferometer Gravitational Observatory (LIGO) announced the first direct observation of a gravitational wave, triggered by the merger of two black holes 1.3 billion light-years away. Within three months of the initial detection, another event was confirmed. The evidence that these events are plentiful in the universe, and that their signatures can be measured quantitatively, has ushered in a new field of gravitational wave astronomy.

LIGO saw its first light in 2002. For nearly a decade, no gravitational wave signal was detected. In 2010 the instruments were taken down for a four year construction period, consisting of both major and minor technological upgrades. The final difference? A factor of 10 improvement in sensitivity.

Doesn't sound like much, but seeing 10 times farther in space meant searching a 1000 times larger volume. Just two days after the instrument came back online,

the first gravitational wave signal appeared.

I tell this story to make two points clear:

- *Understanding noise is essential to the successful design of an instrument.*
- *A small increase in sensitivity of our instruments can usher in whole new worlds of science.*

### 3.1 WHAT IS NOISE?

A signal,  $S$ , with arbitrary units, corresponds to some physical quantity that we would like to detect in the lab. We use an instrument which *measures*  $S$ , but not to its exact value. Instead, our instrument adds a quantity,  $N$ , to our signal, which varies in value each time the measurement is taken, such that the output,  $T$ , is,

$$T = S + N. \quad (3.1)$$

$N$  here stands for some kind of instrumental noise, pulled from a distribution. Say we measure the quantity,  $T$ , a number of times. We would obtain a vector,  $T_i$ , which is in each case equal to  $S_i + N_i$ . But since  $S_i$  is the same in each measurement,  $T_i = S + N_i$ . Now we can derive some relevant quantities. First, taking the average,

$$\langle T \rangle = S + \langle N \rangle. \quad (3.2)$$

We find that the average of the measured values,  $T$ , should be equal to  $S$  as long as the average noise,  $\langle N \rangle$  is zero.  $\langle N \rangle$  is also the *first moment* of its distribution. Squaring Equation 3.2 and then taking the average, we obtain an equation for the second moment of  $T$ ,

$$\langle T_i T_j \rangle = S^2 + \langle N_i N_j \rangle + 2S\langle N \rangle. \quad (3.3)$$

If each instance of the noise is uncorrelated with other instances, then  $\langle N_i N_j \rangle = \langle N^2 \rangle \delta_{ij}$ , and, assuming that  $\langle N \rangle$  is zero as before, Equation 3.3 simplifies to,

$$\langle T^2 \rangle = S^2 + \langle N^2 \rangle, \quad (3.4)$$

where  $\langle N^2 \rangle$  is the *second moment* of the distribution, or its *variance*. Therefore, the variance of  $T$ , defined as  $\text{Var}(T) = \langle (T - \langle T \rangle)^2 \rangle$  is,

$$\langle (T - \langle T \rangle)^2 \rangle = \langle T^2 \rangle - S^2 = \langle N^2 \rangle. \quad (3.5)$$

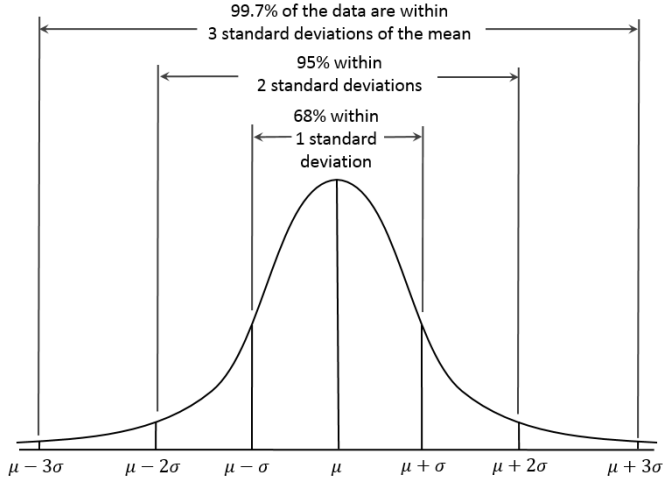


**Figure 3.1.1:** Sketch of a Gaussian distribution (Wikipedia Creative Commons).

We see that  $T$  is drawn from a distribution as well, but one with a mean of the true signal  $S$ , and a variance of the noise  $N$ . This is what is meant by the *uncertainty* on a single measurement  $T_i$ . We can denote the uncertainty in the same units as  $S$  by taking a square-root.

$$\sigma_T = \sqrt{\langle (T - \langle T \rangle)^2 \rangle} = \sqrt{\langle N^2 \rangle} \quad (3.6)$$

Here, we've defined  $\sigma_T$  as the root-mean-squared (RMS) error on each

measurement of  $T$ . This quantity can be understood probabilistically. Typically, noise is Gaussian distributed<sup>1</sup>, and for a Gaussian function, as pictured in Figure 3.1.1, two-thirds of the area is bounded by  $\pm\sigma$ . This means, *for a single measurement  $T$ , there is roughly a 2/3 chance it will fall within  $\sigma_T$  of  $S$ , its true value.*

### 3.2 PROPAGATION OF ERROR

We've seen a simple linear example in Equation 3.6 of how errors propagate from variables to a function of such variables. To generalize, assume a linear function,  $f(x_1, x_2, \dots, x_n)$ , such that

$$f(x_1, x_2, \dots, x_n) = a_1 x_1 + a_2 x_2 + \dots + a_n x_n. \quad (3.7)$$

If each variable  $x_i$  has uncertainty  $\sigma_i = \sqrt{\langle x_i^2 \rangle}$ , to find  $\sigma_f$  we need to begin by squaring Equation 3.7. We can write the result in matrix form,

$$f^2 = a_1^2 x_1^2 + \dots + a_n^2 x_n^2 + 2a_1 a_2 x_1 x_2 + \dots + 2a_1 a_n x_1 x_n \dots = A_{ij} x_i x_j, \quad (3.8)$$

where summation over repeated indices is implied and  $A_{ij} = a_i a_j$ . To find the uncertainty  $\sigma_f = \sqrt{\langle f^2 \rangle}$ , we take the average of both sides of the equation, and setting the general covariance,  $\langle x_i x_j \rangle = \sigma_{ij}^2$ , we obtain,

$$\sigma_f^2 = \langle f^2 \rangle = A_{ij} \sigma_{ij}^2. \quad (3.9)$$

In the simple case where all variables  $\{x_i\}$  are uncorrelated with one another, the propagation of error formula reduces simply to,

$$\sigma_f^2 = a_i^2 \sigma_i^2. \quad (3.10)$$

This method of propagating error applies to general functions  $f(x_1, x_2, \dots, x_n)$

---

<sup>1</sup>Typical noise processes are the sum of multiple random variables and as such do take on a Gaussian distribution per the Central Limit Theorem.

which are not linear function of  $\{x_i\}$  as well. The most common method utilizes the *Taylor series* to rewrite the function  $f(\{x_i\})$  as a sum of polynomials. Using a Taylor expansion around  $x = \mu$ , where  $\mu$  is the mean of  $x$ ,

$$f(x) = f(\mu) + f'(\mu)x + \frac{f''(\mu)}{2}x^2 + \dots \quad (3.11)$$

Therefore, an arbitrary function of multiple variables  $f(x_1, x_2, \dots, x_n)$ , to first order in the Taylor series, may be written

$$f(x_1, x_2, \dots, x_n) = \left. \frac{\partial f}{\partial x_1} \right|_{\mu_1} x_1 + \left. \frac{\partial f}{\partial x_2} \right|_{\mu_2} x_2 + \dots + \left. \frac{\partial f}{\partial x_n} \right|_{\mu_n} x_n + C. \quad (3.12)$$

The same matrix  $A_{ij}$  as above may be written now with  $A_{ij} = \left. \frac{\partial f}{\partial x_i} \right|_{\mu_i} \left. \frac{\partial f}{\partial x_j} \right|_{\mu_j}$  and the general formula for error propagation which results, assuming uncorrelated variables  $\{x_i\}$  is,

$$\sigma_f^2 = \left( \left. \frac{\partial f}{\partial x_1} \right|_{\mu_1} \right)^2 \sigma_1^2 + \left( \left. \frac{\partial f}{\partial x_2} \right|_{\mu_2} \right)^2 \sigma_2^2 + \dots + \left( \left. \frac{\partial f}{\partial x_n} \right|_{\mu_n} \right)^2 \sigma_n^2 \quad (3.13)$$

### 3.3 TURNING DOWN THE NOISE

One nearly universal way of reducing the uncertainty of a measurement is to repeat that measurement many times. In a survey, this means increasing the sample size. In a camera, this means leaving the shutter open for longer. In the hypothetical measurement made in Section 3.1, we can take the average of the vector of independent measurements,  $T_i$ .

The error on the *mean* of  $T$ , or  $\sigma_{\langle T \rangle}$ , can be calculated from the error propagation formula. Since,

$$\langle T \rangle = \frac{1}{n} \sum_i T_i = \frac{1}{n} (T_1 + T_2 + \dots + T_n) \quad (3.14)$$

therefore,

$$\sigma_{\langle T \rangle}^2 = \frac{1}{n^2} (\sigma_{T_1}^2 + \sigma_{T_2}^2 + \dots + \sigma_{T_n}^2) = \frac{1}{n^2} (n\sigma_T^2) \quad (3.15)$$

The error on the mean of  $n$  measurements is smaller than the error on each individual measurement by the square-root of  $n$ . That is,  $\sigma_{\langle T \rangle} = \sigma_T / \sqrt{n}$ .

To generalize this concept, we identify a signal's average value,  $\langle T \rangle$ , with its Fourier transform at zero frequency, where the discrete Fourier transform is defined,

$$\tilde{T}_k = \frac{1}{n} \sum_m T_m e^{2\pi i k m / n}. \quad (3.16)$$

The  $k = 0$  Fourier component is also known as the *DC component* of the signal. The same uncertainty can be assigned to any other Fourier component, that is, other values of  $k$ , as long as the length of the signal is fixed.

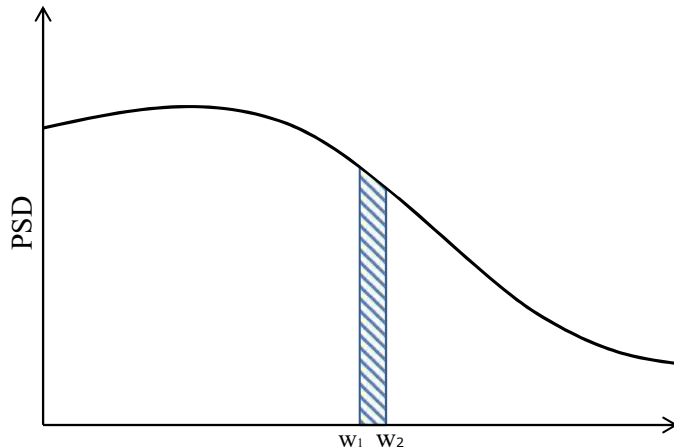


**Figure 3.3.1:** The RMS noise is the square-root of the total power in a band,  $\Omega$ , found by integrating the power spectral density (PSD) of noise between  $\omega_1$  and  $\omega_2$ .

To make this more formal, recall the continuous power spectral density (PSD)

as defined by Equation 2.16. We can rewrite,

$$G_x(\tau) = \frac{1}{\sqrt{2\pi}} \int_{-\infty}^{\infty} S_x(\omega) e^{i\omega\tau} d\omega, \quad (3.17)$$

where  $G_x(\tau) = \langle x(t)x(t + \tau) \rangle$  is the auto-correlation function of some noise variable  $x(t)$ . Setting  $\tau = 0$ , the equation above becomes,

$$\langle x(t)^2 \rangle = \frac{1}{\sqrt{2\pi}} \int_{-\infty}^{\infty} S_x(\omega) d\omega. \quad (3.18)$$

This is a statement that the total variance of the signal is equal to the integral over the entire power spectrum. The above can also be found through an application of *Parseval's Theorem*, which posits the unitarity of a Fourier transform.

Consequently, the variance in a limited *band*, with bandwidth  $\Omega = \omega_2 - \omega_1$ , can be found by a finite integral of the power spectrum between  $\omega_1$  and  $\omega_2$ ,

$$\langle x(t)^2 \rangle_{\Omega} = \sqrt{\frac{2}{\pi}} \int_{\omega_1}^{\omega_2} S_x(\omega) d\omega, \quad (3.19)$$

where  $S_x$  is now the single-sided power spectral density. This calculation is shown graphically in Figure 3.3.1. In the discrete case, this becomes,

$$\sigma_{\Omega}^2 = 2 \sum_{\omega_1 < \omega_i < \omega_2} S_x(\omega_i) \Delta\omega, \quad (3.20)$$

where  $\Delta\omega$  is the minimum possible bandwidth defined by  $\Delta\omega = \frac{2\pi}{n}$ , with  $n$  being the total number of data points. *It becomes clear in this form that the lowest RMS noise which can be achieved coincides with this minimum bandwidth and a choice of  $\omega_0$  such that  $S_x$  is also minimal.*

$$\sigma_{min}^2 = 2S_x(\omega_0)\Delta\omega \quad (3.21)$$

Written in terms of  $n$ , the square-root dependence on sample size emerges once

more,

$$\sigma_{min} = \sqrt{\frac{4\pi S_x(\omega_o)}{n}}. \quad (3.22)$$

A technique called *lock-in detection*, which will be utilized in this work, enables measurement in this specified, optimized band. By modulating a weak signal at the frequency  $\omega_o$ , and performing a single point Fourier transform, maximum signal-to-noise ratio can be achieved.

*There's plenty of room at the bottom.*

Richard Feynman

# 4

## Force Microscopy

FOR THE DIFFERENT ORDERS OF MAGNITUDE forces in our lives there exist very different methods of measurement. For instance, a bathroom scale, using a spring or a strain gauge, is useful in the range of tens to hundreds of newtons. For larger forces a piezoelectric or hydraulic system may be more ideal, and can be employed, for instance, in a truck weighing station. For very small forces, such as the forces which cause proteins to fold in a particular way, a common approach is to track the mechanical deformation of a compliant probe.

Compliant probes are typically made of a flexible cantilever, such as in the case of an *atomic force microscope* (AFM). The cantilever bends in response to an interaction; that deflection is measured and translated into a force. An optically trapped particle can also act as a compliant probe. In this case, a restoring force is provided by optical forces—akin to the spring stiffness of the cantilever—and

motion of the trapped particle relative to its equilibrium position is indicative of a mechanical force. Though AFM's are the standard for performing scanning probe measurements, floating probes have several important advantages including, most importantly, a much lower fundamental limit to the smallest force detectable.

#### 4.1 WHY MEASURE FEMTONEWTON FORCES?

Measurements are scientists' connection to reality. Not only do high precision instruments enable the validation of existing scientific theories, just as importantly, they inspire the search for new theories and new models. It is therefore difficult to predict the kind of impact a two-orders-of-magnitude improvement in force sensitivity will have in various scientific fields.

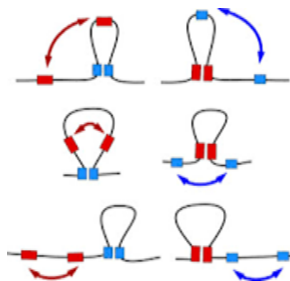


**Figure 4.1.1:** The formation of DNA loops, shown here, is believed to be regulated by femtonewton forces. Graphic from Hfsp.org.

*Biology.* An important point of comparison in biological systems is  $k_B T$ , or the energy scale of thermal fluctuations. For physical systems in a thermal bath, interaction with energies much smaller than  $k_B T$  will tend to have a depressed effect. As such, we may estimate the length-scales on which various forces will tend to act resulting in a marked effect on structure and function. For instance, piconewton forces, such as those involved in hydrogen bonds, will tend to act on the order of nanometers. This implies femtonewton forces would indeed be most likely involved in long-distance interactions on the scale of a micron. Biophysics in the femtonewton and sub-femtonewton regime is in very nascent stages.

However, recently scientists have begun to consider the effects of femtonewton forces in biology, specifically the important roles they may play in biomolecule morphology and structure, the formation of DNA loops and, consequently, in gene regulation [1, 5, 12, 17].

*Optics.* Richard Feynman once said about the future of physics, "There is plenty of room at the bottom." And indeed, recent decades have seen a boom in nanoscale research and fabrication. A particularly interesting area of research focuses on the fabrication of nano- and micro-scale mechanical devices and sensors—miniature pumps, probes, and switches—for use in, among other applications, lab-on-a-chip systems [29]. Light has emerged as a natural tool for the control of individual nano-scale components, with ability to non-invasively manipulate each part individually, as well as many parts in parallel.

For all we know about light, physicists are still developing intuition for the myriad of effects of light on matter. Ongoing studies exploring "anomalous" forces involving tractor beams [52], spin-momentum locking in evanescent waves [11], and spin-orbital momentum transfer [78] have attracted much interest in recent years. They present potentially novel methods of actuation in microfluidic and miniaturized systems.

Since optical forces tend to scale with  $L^2$ , where  $L$  is the probe dimension, while the inertia scales with  $L^3$ , an efficient probe which responds mechanically to an optical force is destined to be small. In fact, they are typically optimized for  $L \approx \lambda$ , where  $\lambda$  is the wavelength of light. Spherical particles fitting this description, whose geometry enables exact calculation of optical forces via analytical Mie Theory (see Section 1.4), are precisely subject to forces at and below the limit of current instrument sensitivities.

## 4.2 ATOMIC FORCE MICROSCOPE

AFM cantilevers (see Figure 4.2.1) have the dimensions of a long rectangle—about tens of microns wide and hundreds of microns long. At the end of the cantilever is the *tip*, a small pyramid with a radius of curvature tens of

nanometers at the point.

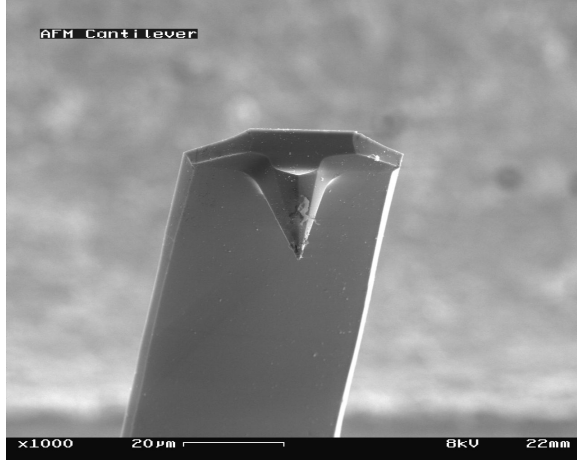


**Figure 4.2.1:** Scanning Electron Microscope (SEM) image of an AFM cantilever tip.

The cantilever is attached to a piezo stage with freedom to move in all three dimensions. The vertical degree of freedom allows the acquisition of force curves as a function of height. The lateral degrees of freedom enables area scanning of a surface—revealing its various topographical and even chemical features. When the tip is brought close to a surface, interaction with the surface causes the cantilever to flex. The amount of flexure is measured by the displacement of a collimated laser beam specularly reflected from the back of the cantilever, as illustrated in Figure 4.2.2.

Force curves as a function of height,  $F_z(z)$ , can be acquired as in the above set-up by scanning the cantilever position with the piezo stage. At each height, the deflection of the cantilever is measured and converted into a force assuming the cantilever behaves as a spring, such that,

$$F_z = -\kappa \Delta z \quad (4.1)$$

where  $\kappa$  is the spring constant, or spring stiffness. The assumption that the

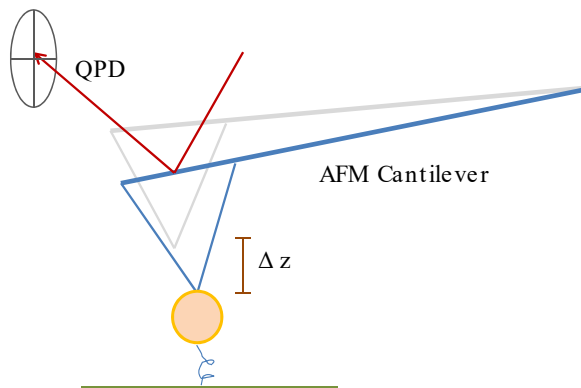


**Figure 4.2.2:** Cantilever of an atomic force microscope (AFM), showing a quadrant photodiode (QPD) detection method. In this example, a microsphere is shown attached to the cantilever tip and tethered by a protein to a functionalized surface. This is a typical method for measuring the forces needed to unfold a protein in a multi-step process.

restoring force is linear with deflection is only valid for small deflections. Thus, an AFM is sensitive to a certain range of forces, defined by the mechanical properties of the chosen cantilever.

The smallest force measurable by an AFM is determined by the random noise in the system. We can define the force sensitivity of a system as the signal threshold which equals the system noise – for a signal-to-noise ratio of 1, or  $S/N = 1$ .

Noise breaks down into two main categories – measurement noise and thermal mechanical noise.

Measurement noise is inherent to the instrument and its various components in the signal path. It limits the precision with which an AFM cantilever's position may be determined by the measurement apparatus. It, for instance, includes shot noise from the laser, electronic noise in the analog-to-digital converter, dark currents in our photodiode, and noise due to interference and resistances in the electronic circuits [53].

In the case that measurement noise is the limiting factor to instrument precision, more compliant cantilevers have been designed. Their lower stiffness, or smaller spring constants, amplify the effects of a small force into a measurable

displacement.

Thermal mechanical noise, on the other hand, refers to actual random motion of the cantilever itself. The cantilever, in a thermal bath of fluid molecules, undergoes Brownian motion as a result of random collisions. We learned from Chapter 2 that the force spectrum of such collisions is flat— that is, the noise is *white*— and the magnitude of these fluctuations is proportional to the temperature as well as the cantilever’s drag coefficient,  $\gamma$ .

To reiterate,

$$S_F = 2\gamma k_B T \quad (4.2)$$

Since thermal mechanical noise results in physical displacements of the cantilever which may mask its response to an applied force, it imposes a fundamental limit on the sensitivity of any mechanical probe instrument. And this limit is much quicker reached in fluid than in air, on account of the orders of magnitude larger drag forces in the former environment. The result is the reduced functionality of AFM’s in fluid, un-helped by more compliant cantilever designs, and a limit to the achievable force resolution of around 1-10 piconewtons.

### 4.3 FLOWING PROBE MICROSCOPE

To improve upon this fundamental sensitivity limit, some have proposed and fabricated miniature cantilevers [70] which present a reduced footprint in fluid. These cantilevers can be about ten-times smaller than those commercially available, and can hypothetically result in nearly an order of magnitude reduction in thermal noise and increase in sensitivity. But in trade, cantilevers become stiffer as they become smaller. Accordingly, they also scatter less light and are more difficult to track using the back-reflected laser beam. These increases in measurement noise have the potential to offset reductions in thermal noise.

Alternatively, floating probe microscopes replace the AFM cantilever with an optically trapped— but otherwise free-floating— microsphere. It offers

independent choice of probe dimensions and trap stiffness, and microspheres as small as a micron in diameter can be used, resulting, potentially, in a more than two-orders-of-magnitude reduction in drag compared with commercial AFM cantilevers.

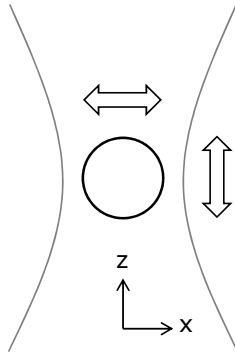


**Figure 4.3.1:** Schematic of an optical tweezer. By moving the focus of the optical trap, the floating probe's mean position can be manipulated to "scan" across an area or volume.

Additionally, floating probe microscopes have the following advantages over conventional AFMs:

- An optical trap spring constant which is tunable by changing laser power.
- Non-intrusive and *in situ* contact-free measurements.
- Minimal mechanical coupling to noisy environment. In contrast with AFMs, noise shielding is generally unnecessary.
- Symmetric probe with three-dimensional force sensitivity, unlike AFM's which are only able to measure forces in the vertical direction.

Early efforts to build a floating probe force microscope began shortly after the discovery of the optical tweezer. Led primarily by the research of Dennis Prieve and E. L. Florin [23, 61], Total Internal Reflection Microscopy (TIRM) and Photonic Force Microscopy (PFM) were some of the earliest floating probe candidates for force profile measurement and quantitative imaging, respectively.

#### 4.3.1 TOTAL INTERNAL REFLECTION MICROSCOPY

In TIRM, a microsphere is held steadily by a low numerical aperture beam— that is, an optical trap with a much higher trap stiffness in the lateral directions than in the vertical— and allowed to "explore" the local force environment in the vertical direction. The particle is tracked by the intensity of light it scatters from a second, totally-internally-reflecting "probe" beam. Since the evanescent field created by this latter beam in the rarer medium decays exponentially away from the reflecting interface, the scattered light provides exponential sensitivity to the particle-surface separation [62],

$$I(z) = I_0 e^{-\beta z} + C. \quad (4.3)$$

$I_0$  gives the intensity expected when  $z = 0$ , or when the microsphere is in contact with the surface.  $\beta^{-1}$  is the decay length of the intensity of the evanescent field, and  $C$  is a constant accounting for background. Specifically,  $\beta$  can be easily calculated by applying phase matching conditions at the reflection boundary,

$$\beta = \frac{4\pi}{\lambda} \sqrt{(n_1 \sin \theta)^2 - n_2^2} \quad (4.4)$$

where  $\lambda$  is the wavelength of incident light in free space,  $n_1$  and  $n_2$  are the refractive indices of the incident and reflecting medium, respectively, and  $\theta$  is the angle of incidence of the light.

A probability density function (PDF) is created of the particle's position at various independently sampled moments, hereafter called  $p(z)$ , see Figure 4.3.2. Assuming the system is ergodic, the local force environment can then be deduced assuming thermal equilibrium, by inverting

$$p(z) = \frac{1}{Z_0} e^{\frac{-V(z)}{k_B T}} \quad (4.5)$$

$Z_0$  here is the partition function, and  $V(z)$  the integral of a conservative force-field  $F(z) = -\frac{dV}{dz}$ . This latter relation is valid as long as the force field has

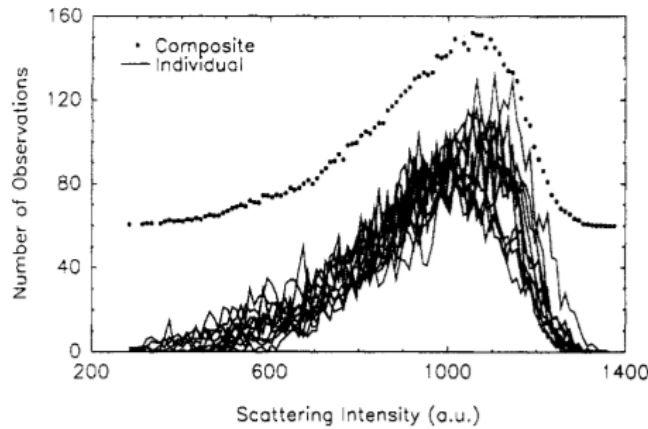


**Figure 4.3.2:** Probability density function from Prieve's 1990 paper on Total Internal Reflection Microscopy (TIRM).

zero curl. Examples of the resulting function is provided in Figure 4.3.3.

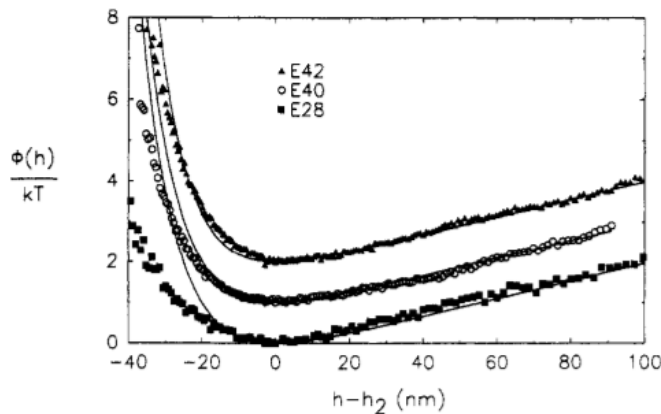


**Figure 4.3.3:** Potential energy profiles,  $V(z)$ , here labeled,  $\Phi(h)$ , from Prieve's 1990 paper on Total Internal Reflection Microscopy (TIRM).

Using this method, researchers measured various colloid-surface interaction potentials, including those for double-layer repulsion [22], van der Waals attraction [10], and the gradient forces of an evanescent field itself [73]. However, the technique was not able to achieve thermally limited sensitivity for a fundamental reason: the full statistical power of each measurement is diluted

over an array of discrete position values  $z_i$  used to generate the PDF. Thus, the theoretical limit of sensitivity for this technique includes a trade-off between the position resolution and the force sensitivity, approaching the thermal limit as the number of discrete position points used to build the PDF goes to one.

The technique has several other important limitations. The result of a TIRM measurement is a composite of all forces acting on the probe in the direct vicinity of the trap focus. As a result, small forces are not discernible against the large, ubiquitous background of the optical trap and surface repulsion. In addition, the technique lacks the capability to vertically position the probe, and thus has sensitivity usually limited to a region within a few hundred nanometers from the surface. Finally, without a vertical scanning capability, exact coefficients in Equation 4.5 cannot be determined experimentally. Knowledge of the absolute height of the probe relative to the surface is abandoned for position relative to the mean height, and measurements are subject to potentially large systematic errors.

For these combined reasons, though a floating probe technique has the opportunity to increase sensitivity by orders of magnitude over conventional AFM techniques, the promise had yet to be realized. TIRM and PFM methods have been limited to sensitivities around 50-100 femtonewtons.

The central objective of the work described in this document, therefore, aims to innovate on the basis of this promising technique, and thus, for the first time, achieve thermally limited force sensing in a floating probe.

THE NEXT THREE CHAPTERS consist of text culled from three publications [42, 43], sometimes verbatim. They will be presented chronologically, and divided into main text and supplemental information, when applicable. Over the course of my PhD, the experimental setup itself was a living instrument, of sorts, always continually modified and improved. For the sake of clarity, each chapter will present the set-up as it stood in operation at that time. The most current version of the instrument will be described in the section about ongoing and future work, as well as in the Appendix.

The first publication introduced a new scanning capability to floating probe microscopy. Using this capability, we demonstrated for the first time absolute position particle tracking using a calibrated evanescent wave.

The second publication, built on the groundwork laid by the first paper, demonstrated thermally limited sub-femtonewton force sensing in fluid two orders of magnitude more sensitive than any other technique.

The third publication added an additional detection method for particle tracking in the lateral direction, making possible simultaneous 2-D measurements of the motion of a microsphere probe. We make the surprising observation of elliptical motion—angular momentum transfer by an evanescent wave to an optically trapped microsphere, using light with no intrinsic orbital angular momentum.

*Let us not grow weary in doing good, for in due season we shall reap if we do not lose heart.*

Hillary Clinton (quoting Galatians 6:9)

# 5

## Particle Tracking with a Calibrated Evanescent Wave

WE PROPOSE AN OPTICAL TWEEZER-BASED CALIBRATION of an evanescent-wave particle tracking technique which directly measures the intensity-height profile for a given scatterer in the total internal reflection microscopy (TIRM) configuration and can be performed quickly and *in situ*. As a reminder, the intensity-height profile takes the general form,

$$I(z) = I_o e^{-\beta z} + C. \quad (5.1)$$

The optical tweezer, or single-beam gradient optical trap, holds the scatterer in three dimensions at a fixed position relative to the beam focus. By shifting the

focus, the particle can be made to approach the surface in precisely measured steps. The scattering intensity is monitored until further steps produce no change in the signal, indicating that the bead has reached the surface.

A few straight-forward changes made to the usual TIRM setup enables our *in situ* calibration. First, the collection objective is replaced by a high NA water-immersion objective capable of 3D optical tweezing of a micron-sized dielectric particle. Second, the micrometer vertical stage on which the objective is mounted is fitted with closed-loop piezo controls for finely calibrated focus adjustment. And finally, the top surface of the glass sample slide is coated with a quarter-wavelength thick layer of evaporated glass to cancel the optical tweezer reflected beam. By opening and closing an iris located in the back focal plane of the objective, we adjust trap laser power and NA and can quickly switch between 3D optical tweezing (calibration) and 2D optical trapping (measurement) modes of operation.

We confirm the precision of our absolute position particle tracking method with two experiments. The first experiment measures intensity-height calibration curves for several evanescent field penetration depths,  $\beta^{-1}$ , ranging from 90 nm to 270 nm taken with the same probe particle.

In the second experiment, we fix the angle of incidence such that the penetration depth is about 300 nm and measure the hindered perpendicular diffusion coefficient of a 3  $\mu\text{m}$  glass microsphere in steps of 50 nm out to a distance of about 1.2  $\mu\text{m}$ . Our results are in agreement with hydrodynamic theory, and represent the longest range and most accurate measurement of hindered near-wall diffusion using TIRM.

## 5.1 EXPERIMENT

### 5.1.1 SETUP

In this experiment we use plain glass microspheres with a density of 2.0 g/cm<sup>3</sup> and a nominal diameter of 3  $\mu\text{m}$  (Corpuscular, Inc C-SIOs-3.0). The beads come

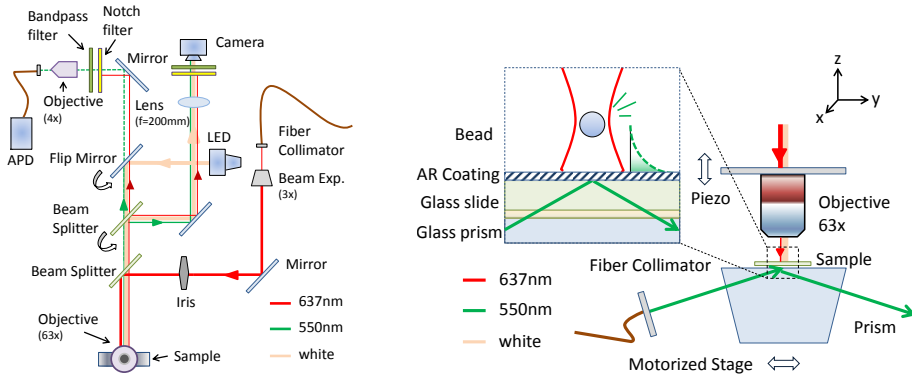


**Figure 5.1.1:** a) Top-down view of the total internal reflection microscopy (TIRM) setup with the trap, scattered and illumination paths denoted with red, green, and yellow lines respectively. b) Side-view of the TIRM setup. Inset: zoom in of a measured bead with the optical trap (red) and evanescent field profile (green) superimposed.

suspended in deionized water and are diluted by a factor of 100 and allowed to equilibrate at room temperature before being loaded into the microfluidic sample chamber. The chambers have thicknesses of 15–20  $\mu\text{m}$  for use with a short working-distance objective, please see the Appendix for details in the fabrication procedure.

The anti-reflection (AR) coating, when it is applied, is deposited onto the top surface of the glass slide via plasma enhanced chemical vapor deposition (PECVD). It consists of a quarter-wavelength thick layer of evaporated  $\text{SiO}_2$ , with index 1.45, which closely approximates the geometric mean of  $n=1.42$  for glass ( $n=1.52$ ) and water ( $n=1.33$ ).

Figure 5.1.1 shows the optical set up, views from the top and side are provided. Three light sources illuminate our sample. The collimated output from a 637 nm diode laser (Thorlabs LP637-SF70) serves as our single beam optical trap. It is expanded then focused through an objective onto the sample surface. The evanescent wave used for positional sensing is generated by total internal reflection of a 550 nm laser source (NKT Photonics SuperK) at the lower water-glass boundary of the sample chamber. A polarizer and a half-wave plate is used to control the polarization of the 550 nm source. P-polarization (or TM

polarization) was chosen for our experiments due to suppressed multiple reflections compared with S-polarization [32], and the scattered light detected without a polarizer. Lastly, for visualization and positioning, a white LED provides bright-field illumination of the sample surface over our  $50\ \mu\text{m}$  field of view.

During the experiment, our sample slides rest on a 60 degree prism made of BK7 glass in some index-matching fluid. The prism is mounted on a two-axis motorized translation stage (Thorlabs LNR<sub>50</sub>S) which controls lateral positioning of the sample with micron-precision. A vertical translation stage (Thorlabs MAX<sub>301</sub>) with closed loop piezo electronics positions the objective with better than 5 nm precision. The vertical travel range is 4 mm manually and  $20\ \mu\text{m}$  by piezo.

We use a water immersion objective (Leica 63x NA 1.25) in order to avoid the detrimental effects of spherical aberration introduced by the immersion oil and water index mismatch [65]. This also ensures that a vertical step in the piezo motor corresponds to an equal magnitude displacement of the optical trap focus in our sample fluid.

The same objective collects the photons scattered by the particle from the evanescent sensing field. The scattered light, after traversing bandpass filters, is focused by a 4x objective onto a multimode optical fiber and fed into a photon counter (Micro Photon Devices PDM APD). The photon counting interval can be set with a function generator in combination with a pulse counter (National Instrument PCI-6602) and in this experiment ranges from  $200\ \mu\text{s}$  to 1 ms. The diameter of the multimode fiber core is  $100\ \mu\text{m}$  which sets the size of the collection area on the sample surface, measured with a stuck bead, to be about  $6\ \mu\text{m}$  in diameter. Outside this area, the extinction is nearly complete, with counts at background levels.

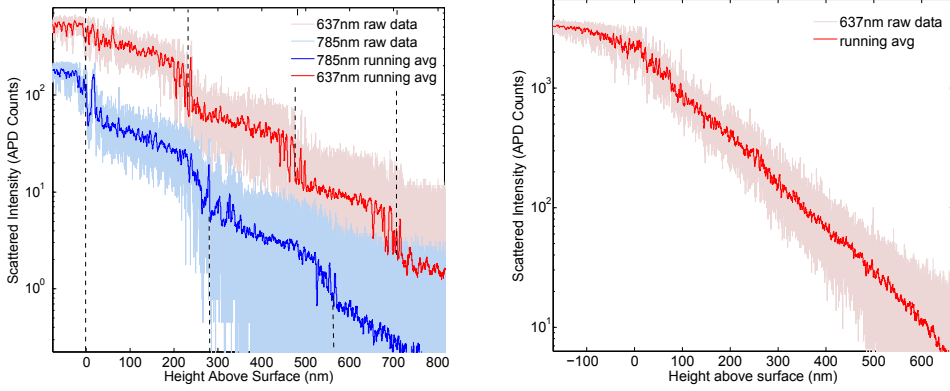


**Figure 5.1.2:** Plots of measured scattered light intensity versus height for a  $3 \mu\text{m}$  bead above the surface of a glass microscope slide. Red: using a 637 nm wavelength optical tweezer. Blue: using a 785 nm wavelength optical tweezer. (a) No AR coating: the step-like behavior is due to formation of a standing-wave component in the optical trap due to reflection from the glass-water interface. The plots are shifted vertically for clarity. (b) AR coated: the reflection is eliminated and the bead is able to step smoothly towards the surface.

### 5.1.2 DATA

We observe that the single-beam gradient optical trap [8] was sufficient to lift a  $3 \mu\text{m}$  diameter glass bead in water at powers as low as 20 mW behind the objective. Since in this experiment gravitational and radiation pressure forces act in the same direction, the bead, as expected, is trapped axially slightly below the focus of the beam [7]. The probe beam, used to generate the evanescent field for particle tracking, is kept at relatively low power (less than 1 mW at a spot size of  $300 \mu\text{m}$ ) to prevent perturbation of the bead. Background counts, taken with the bead held far (at least  $2 \mu\text{m}$ ) from the glass-water interface, are mostly due to scattering of the evanescent field by impurities on the glass slide, and contribute approximately 15 to 20 photon counts per millisecond, resulting in a signal-to-noise ratio typically better than 100 for our experiments.

The particle absolute position calibration as a function of scattering intensity is determined as follows: first, the background measurement is taken, then the bead is lowered in precisely measured steps towards the surface and the scattered intensity is monitored until contact of the bead with the surface is made. Two

abrupt changes in the collected signal are observed at the bead-surface contact point (Figure 5.1.2). First, the intensity becomes constant with further piezo steps, and second, the variance in measured counts decreases and approaches Poisson statistics. This decrease in variance is due to the fact that the bead is no longer diffusing since it is in contact with the surface. We use these features to find the location of the surface and therefore the absolute position of the bead. Since the ability of the bead to approach the surface is limited by the presence of a strong electrical double layer force [34, 61], NaCl is introduced into the sample fluid at a minimum concentration of 0.01 molar in a typical calibration scan. The effects of salt concentration on the measured intensity profile will be further discussed in Section 5.1.2.

#### AR COATING

Optical tweezing near a dielectric boundary suffers from a known complication due to interference caused by a weakly-reflected backward-traveling wave [37]. Even as the focus of the optical tweezer shifts, the interference fringes remain fixed relative to the location of the surface, resulting in step-like behavior of the trapped particle at regular intervals [35]. The effect of the standing wave modulation of our optical trap, despite the relatively low index contrast and reflectivity ( $\sim 0.4\%$ ) at the water-glass interface, can be observed in our data (Figure 5.1.2(a)). We further confirm the effect is optical by changing the wavelength of the trapping laser from 637 nm to 785 nm. The spacing of the fringes is measured to increase  $21 \pm 2\%$  which agrees with the theoretical prediction of 23%.

When an AR coating of  $\text{SiO}_2$  is deposited with thickness of 110 nm, a dramatic effect is observed. We measure a reduction by more than a factor of 10 in the standing-wave modulation of the optical tweezer. This is achieved without altering glass surface's chemical and electrical properties.

The intensity vs. height profile measured for a  $3 \mu\text{m}$  glass sphere above an AR-coated glass surface is shown in Figure 5.1.2(b).

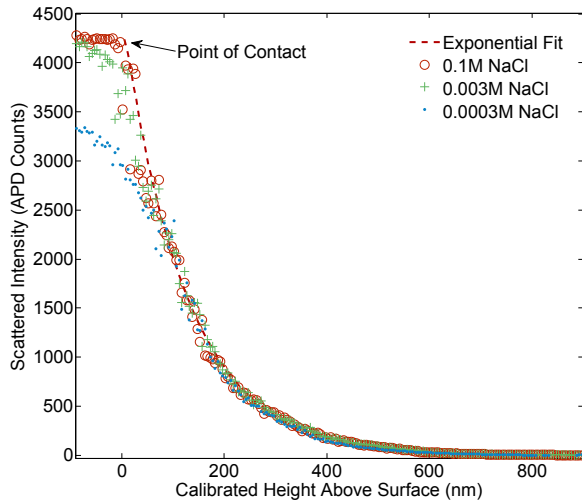


**Figure 5.1.3:** Calibration curves obtained for a  $3 \mu\text{m}$  diameter bead in water for various NaCl concentrations (corresponding Debye lengths: 1 nm, 5 nm, 20 nm). The blue curve shows a condition of insufficient screening: despite the optical tweezer focus moving beneath the surface of the glass, the negatively charged bead is repelled electrostatically at close separations and unable to actually approach the negatively charged surface. Green and red curves: additional salt brings calibration curves closer to the ideal exponential behavior.

#### ELECTROSTATIC DOUBLE LAYER

Plain glass microspheres in DI water above a glass substrate exhibit strong electrical double layer repulsion since both surfaces acquire a negative charge upon contact with the fluid. This electrostatic repulsion is partially screened by a mobile layer of positively charged counter-ions whose thickness (characterized by the Debye length) depends upon the concentration of dissolved electrolytes and can be hundreds of nanometers in extent in low molarity aqueous solutions [34]. In the case where the Debye length ( $\lambda_d$ ) and separation ( $z$ ) are small compared to the radius of the particle, the potential profile of the electrical double-layer interaction is well approximated by a decaying exponential[18],

$$V_{dl} = Ae^{-z/\lambda_d} \quad (5.2)$$

where  $A$  is a constant which depends on the surface potentials and geometries of the interacting bodies and can be quite large (on the order of 100 mV) in the case of glass in water, and the Debye length,

$$\lambda_d = \sqrt{\frac{\epsilon_r \epsilon_0 kT}{e^2 N_A \sum_i c_i z_i}} \quad (5.3)$$

is determined by the permittivity of the fluid ( $\epsilon_r$ ) and the concentration of electrolyte species in mol/m<sup>3</sup> ( $c_i$ ) with valency  $z_i$ , where  $N_A$  is the Avogadro constant.

As we lower the glass bead held in our optical tweezer in steps towards the glass surface, interaction of their double-layers can not only disturb the equilibrium position of the sphere relative to the optical tweezer focus, but can in some cases altogether prevent the sphere from coming into contact with the surface.

Figure 5.1.3 illustrates this effect. In the presence of a strong double layer, as the trapping beam focus moves towards the surface, the bead does not follow. In the data, this manifests as lower than expected APD counts. However, by increasing electrolyte concentration, by the addition of NaCl to the colloidal mixture, the double layer is thinned and its influence diminished until the resulting intensity-height curve is similar to what one would expect from a hard-wall potential. By examining the shape of the curves as a function of ion concentration, we determined 0.01M to be a reasonable lower bound on the required salt concentration for an accurate calibration. As our piezo has precision better than 5 nm, we estimate that the contact-point determined in this way has an uncertainty less than 10 nm.

## 5.2 TWO EXPERIMENTAL RESULTS

To demonstrate the effectiveness of our calibrated evanescent wave particle tracking method, we present two results, obtained with 3 μm diameter glass microspheres optically trapped in water above a glass surface.

## DIRECT MEASUREMENT OF CALIBRATION PARAMETERS

The first (Figure 5.2.1) shows our method's sensitivity to changes in angle of incidence of the totally internally reflected probe beam. The second (Figure 5.2.2), presenting a highly accurate, long range measurement of the hindered near-wall diffusion coefficient, demonstrates the high spatial and temporal resolution particle tracking which can be now achieved.

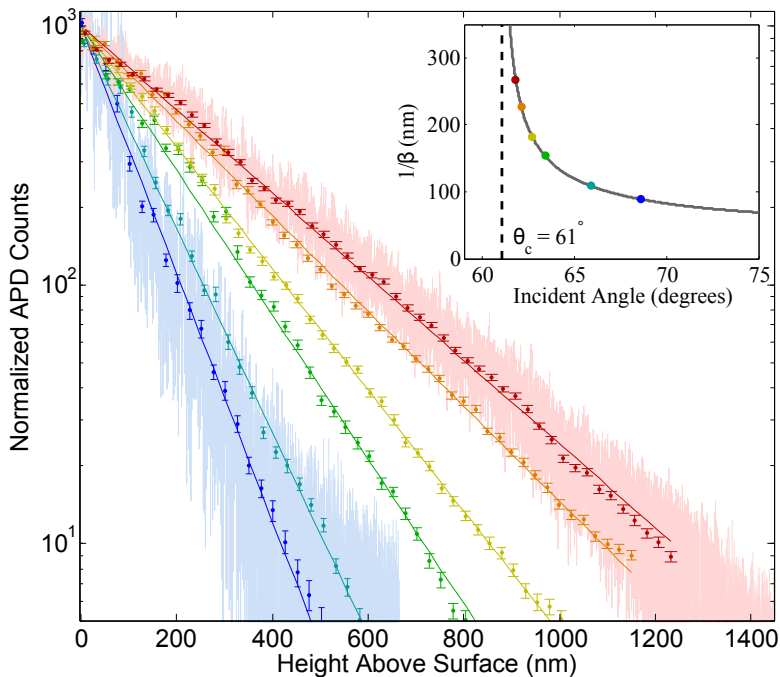


**Figure 5.2.1:** Normalized scattered intensity profiles as a function of height for a 3  $\mu\text{m}$  diameter  $\text{SiO}_2$  bead in water as angle of incidence of probe beam is varied. Fitted decay lengths of the evanescent field intensity are 90.8, 110.6, 115.6, 159.9, 185.2, 236.4, 268.9 nanometers, corresponding to angles of 68.6, 65.9, 63.4, 63.3, 62.7, 62.1, and 61.8 degrees respectively. The error on all fits is less than 1%. The critical angle is 61.0 degrees for the system. For clarity, raw data is only shown for the longest and shortest decay length measurements. Graph inset plots color-coded measured decay lengths as dots on the curve  $\beta^{-1}(\theta)$ .

The decay-length ( $\beta^{-1}$ ) of the evanescent field used for positional sensing depends upon the angle of the incident beam and diverges as the angle

approaches the critical angle ( $\theta_c = \sin^{-1}(n_2/n_1)$ ),

$$\beta = \frac{4\pi}{\lambda} \sqrt{(n_1 \sin \theta_1)^2 - n_2^2}. \quad (5.4)$$

As it is difficult, in typical TIRM experiments, to determine the angle of incidence with precision better than half a degree [41, 62], uncalibrated TIRM measurements, even in systems with well-behaved exponential intensity-distance relations, suffer from growing uncertainty in the  $\beta$  parameter. For example, assuming an index of refraction for glass slides of  $1.52 \pm 0.01$  and a half-degree uncertainty in angle, at  $\beta^{-1}$  of 150 nm, the uncertainty in  $\beta$  is approximately 13%. For a probe at a nominal height of 400 nm from the surface, this translates into an uncertainty of about 50 nm from the determination of  $\beta$  alone. As this error is systematic to the measurement, it cannot be reduced by increasing integration or data collection time. At  $\beta^{-1}$  of 250 nm, the uncertainty becomes even more dramatic ( $\sim 35\%$ ), corresponding to an uncertainty of 140 nm at a bead height of 400 nm.

One major advantage of the TIRM technique over other high-precision positional sensing techniques is the experimenter's ability to tune for sensitivity against desired range by changing the  $\beta^{-1}$  parameter. This ability is lost in a typical uncalibrated TIRM experiment, where evanescent-field decay-lengths are usually kept to around 100 nm or below to ensure a correct estimation of the  $\beta$  parameter.

Figure 5.2.1 demonstrates precise and accessible tuning of the decay-length parameter to values between 90 and 270 nm, spanning the range from that of a typical TIRM experiment to the upper limit of the validity of the exponential-intensity profile. The scans took approximately two minutes each and are fit to pure exponentials according to the least-squares method. The error on the  $\beta$  parameters do not exceed 1% on any fit and can be further improved with increased integration time.

## WALL EFFECTS ON DIFFUSION COEFFICIENTS

A sphere in fluid diffusing close to a planar surface will experience increased viscous drag as compared to its motion in the bulk. This increased drag force manifests in the Brownian dynamics of the particle as reduced diffusion. In particular, the parallel  $D_{\parallel}$  and perpendicular  $D_{\perp}$  diffusion coefficients of a sphere of radius  $R$  at height  $z$  above a substrate calculated using hydrodynamic theory are [14, 28]

$$D_{\parallel} = D_0 \left( 1 - \frac{9}{16} \Lambda + \frac{1}{8} \Lambda^3 - \frac{45}{256} \Lambda^4 - \frac{1}{16} \Lambda^5 \right)^{-1} \quad (5.5)$$

$$D_{\perp} = D_0 \left[ \frac{4}{3} \sinh \alpha \sum_{n=1}^{\infty} \frac{n(n+1)}{(2n-1)(2n+3)} \left( \frac{2 \sinh(2n+1)\alpha + (2n+1) \sinh 2\alpha}{4 \sinh^2(n+1/2)\alpha - (2n+1)^2 \sinh^2 \alpha} - 1 \right) \right]^{-1} \quad (5.6)$$

where  $\Lambda = \frac{R}{R+z}$  and  $\alpha = \cosh^{-1}\left(\frac{z+R}{R}\right)$ .

The exact dependence of the diffusion coefficients on  $z$  has been validated by experimenters with varying methods but overall success [16, 21, 59, 67].

Historically, TIRM has fallen short of the holographic, interferometric methods of particle tracking. Without a reliable calibration scheme, errors in absolute position are large and the measurement range is limited. Existing diffusion coefficient measurements based on TIRM do not extend beyond several hundred nanometers from the surface and are either sparse or systematically disagrees with hydrodynamic theory.

We performed a calibrated particle-tracking experiment where a  $3 \mu\text{m}$  diameter glass sphere held by an optical tweezer is lowered in steps of  $50 \text{ nm}$  towards the glass. At each piezo position, the scattered probe intensity is monitored for  $20 \text{ s}$  with a temporal resolution of  $200 \mu\text{s}$ . The average intensity at each point is used to build the  $I(z)$  calibration curve, and the full time-series, converted to positions, is used to generate the autocorrelation function.

The position autocorrelation function for a particle undergoing damped Brownian motion in a harmonic oscillator potential, for overdamped systems

(such as ours) where the particle is weakly trapped in a viscous fluid, is[69]

$$\begin{aligned} G(t) &= \langle z(0)z(t) \rangle \\ &= \frac{kT}{m\omega_0^2} e^{\frac{-\gamma t}{2}} \left( \cosh(\omega_1 t) + \frac{\gamma}{2\omega_1} \sinh(\omega_1 t) \right) \end{aligned} \quad (5.7)$$

where  $t$  is the time delay between two measurements of particle position,  $\omega_0$  is the resonant frequency of the trap,  $\omega_1 = \sqrt{\gamma^2/4 - \omega_0^2}$ , and  $\gamma = 6\pi R\eta/m$  is the Stokes drag coefficient divided by mass. In the limit of very small  $t$ , that is, at times shorter than the momentum relaxation time for the sphere (in our case around 1  $\mu$ s), the motion of the particle is ballistic and the autocorrelation function is quadratic. In the limit of large  $t$ , at  $t > 20$  ms, the autocorrelation function reflects that of an overdamped harmonic oscillator and is a decaying exponential. At intermediate time scales, the motion resembles that of a freely diffusing particle, and the auto-correlation can be approximated by a linear function,

$$G(t) \approx -D_{\perp}t + \text{const.} \quad (5.8)$$

whose slope is the diffusion coefficient  $D_{\perp}$ . This dependence is shown in Figure 5.2.2 (inset), which allows us to extract  $D_{\perp}$  via a linear fit of the particle's autocorrelation function at  $t$  between 200  $\mu$ s and 5 ms.

Figure 5.2.2 shows the diffusion coefficient as a function of height obtained in this manner, which agrees well with predictions from hydrodynamic theory. The measurement which produced this data took a total of 20 minutes and spans the distance range from a few nanometers to 1.2 microns above the glass surface.

As the trapping power was measured to be 40 mW behind the objective, we assume negligible heating of the fluid and particle [57]. The fitted radius of the bead assuming the measured room temperature of 22 C is  $1.26 \pm 0.02$   $\mu$ m.

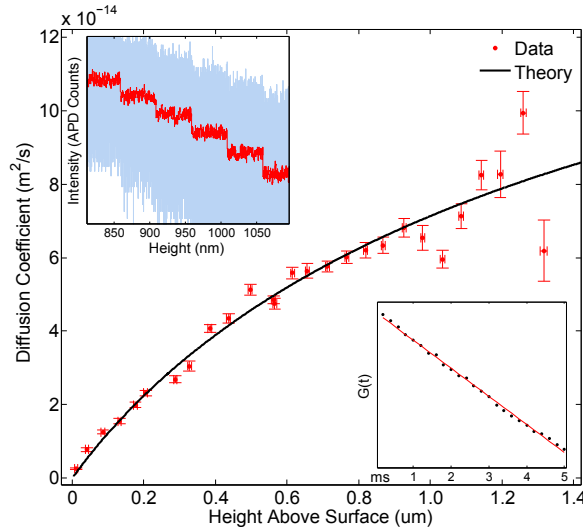


**Figure 5.2.2:** Measured diffusion coefficient as a function of height for motion in the normal direction. Temperature assumed to be room temperature (22 C). Fitted particle radius is  $(1.26 \pm 0.02) \mu\text{m}$ . *Inset top left:* Raw scattered intensity data (blue) and its moving average (red) showing 50 nm piezo steps. *Inset bottom right:* Example autocorrelation function (black dots) and linear fit (red line) in the intermediate time (diffusive) regime.

#### PRECISE MEASUREMENT OF BEAD RADIUS

To confirm the accuracy of the fit result, we undertake an independent method of determining bead radius, whereby we measure the change in effective bead mass as a function of trap radiation pressure and extract the bead mass intercept (at zero radiation power) via a linear regression.

The total potential energy profile for a glass bead above a glass surface is expected to be, combining the double layer repulsion discussed previously and the gravitational and radiation pressure effects,

$$V(z) = Ae^{-z/\lambda_d} + Bz \quad (5.9)$$

where  $B = (\rho_{\text{bead}} - \rho_{\text{water}})Vg + \varphi$ ,  $\rho_{\text{bead}}$  and  $\rho_{\text{water}}$  are the densities of glass and water,  $V$  the volume of the bead,  $g$  the gravitational acceleration, and  $\varphi$  the force due to radiation pressure. We reduce the NA of the trapping beam by closing the

iris in the back focal plane of the objective, eliminating the axial confinement of the particle, and obtain parameter B by fitting the potential for several different trapping powers. Assuming that radiation pressure scales linearly with laser power (P) for a given bead and trap configuration, i.e.  $\varphi = \alpha P$ , a linear fit of B vs. P yields from the intercept the bead mass, and therefore radius.

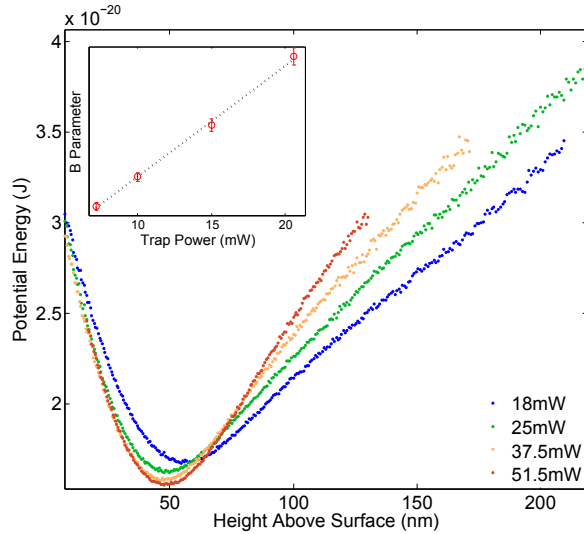


**Figure 5.2.3:** Potential energy profiles measured for four different powers of the low NA trapping beam. Curves are shifted horizontally to better visualize change in the B parameter (as defined in Equation 5.9), or the slope of the linear portion of the potential. Inset: B parameter vs. trapping power, and the linear fit used to calculate the particle's radius.

Figure 5.2.3 shows potential energy profiles obtained by the Boltzmann distribution method described in Chapter 4 for the glass sphere whose diffusion coefficient we measured in Section 5.2. The optical trap NA was reduced to less than 0.2 and the trap power varied between 18 mW and 51 mW. The bead radius we obtain by fitting the potential energy profiles, assuming room temperature, is  $1.27 \pm 0.05 \mu\text{m}$ , which is in good agreement with the  $1.26 \pm 0.02 \mu\text{m}$  result from 5.2.

### 5.3 CONCLUSIONS

We have developed a scheme for high resolution absolute position particle-tracking using the TIRM scattering method. By direct measurement of the essential calibration parameters *in situ*, we eliminate errors associated with their usual estimation or calculation.

Compared to typical TIRM experiments, we demonstrate a more than factor of ten error reduction in determining the decay-length parameter which sets the measurement range of a TIRM experiment. We show free and ready tuning of this parameter, a valuable experimental degree of freedom rarely before exploited due to prohibitively large errors. We are able to locate the point of contact, with better than 10 nm precision, yielding absolute instead of relative positional tracking. To show the extended versatility of the TIRM technique we repeated an experiment requiring high sensitivity, long range, and absolute positions that has previously proved challenging for this sensing method. Our results exceed in range that of previous experiments by a factor of 3 and show good agreement with hydrodynamic theory throughout.

# 6

## Thermally-Limited Sub-Femtonewton Resolution Force Microscopy

WE DEMONSTRATE THERMALLY-LIMITED FORCE SPECTROSCOPY using a probe formed by a dielectric microsphere optically trapped in water near a dielectric surface. We achieve force resolution below 1 fN in 100 s, corresponding to a 2 Å RMS displacement of the probe. Our measurement combines a calibrated evanescent wave particle tracking technique and a lock-in detection method. We demonstrate the accuracy of our method by measurement of the height-dependent force exerted on the probe by an evanescent wave, the results of which are in agreement with Mie theory calculations.

## 6.1 INTRODUCTION

Recall that the smallest measurable force is fundamentally limited by the presence of a fluctuating background force exerted on the probe by its thermal environment. For a probe coupled to a fluid at temperature  $T$ , with a drag coefficient  $\gamma$ , the fluctuation-dissipation theorem predicts the (single sided) power spectral density (PSD) for fluctuations of the thermal force to be [27],

$$S_F^{\text{th}}(\omega) = 4\gamma k_B T, \quad (6.1)$$

where  $k_B$  is the Boltzmann constant, and  $\gamma$  relates the dissipative drag force,  $F_d$ , to the velocity  $v$  of the probe according to  $F_d = -\gamma v$ . For a continuous force measurement with bandwidth  $\Delta\omega$  at a frequency  $\omega_0$ , thermal fluctuations add a stochastic contribution, with a standard deviation of

$$\sigma_{th} = \sqrt{S_F^{\text{th}}(\omega_0)\Delta\omega}. \quad (6.2)$$

High sensitivity measurements require conditions which minimize  $S_F^{\text{th}}$ . Damping can be reduced by operating in high vacuum and using high-Q (low internal damping) oscillators, while  $T$  can be minimized by cooling the system to cryogenic levels. Such measures, however, cannot be implemented for aqueous systems, in which the temperature is restricted to be near room temperature, and the viscosity of water results in damping orders of magnitude greater than in air. Force detection in an aqueous environment, however, is vital for measurement of biological systems, investigation of forces mediated by fluids, or to eliminate capillary effects present during measurements in atmosphere.

As discussed in Chapter 4, optically trapped microspheres have an advantage over AFM cantilevers for measurements in water due to their small size. A  $1 \mu\text{m}$  diameter sphere in water has a damping coefficient below  $10^{-8} \text{ kg/s}$ , corresponding to a thermally-limited sensitivity of  $\sim 10 \text{ fN}/\sqrt{\text{Hz}}$ , much smaller than that of a typical AFM tip, especially when it is near a surface [27]. However, attaining thermally limited sensitivity in DC force measurements using trapped

microspheres is technically difficult due to the presence of  $1/f$  noise sources.

Forces as small as 20 fN (with averaging times of at least 10 minutes) have been measured using a method known as photonic force microscopy (PFM) [23, 33], in which the force is determined from the statistics of the thermal motion of the particle. However, PFM involves a trade-off between position resolution and force sensitivity: the thermally-limited force sensitivity of PFM scales with  $n^{3/2}$ , and approaches Eq. 6.2 for  $n = 1$ , where  $n$  is the number of points along which the thermally sampled potential is differentiated. The details of this calculation are discussed in the following Additional Information Section 6.7.7.

In this work, we measure height-dependent forces exerted by an evanescent field on an optically trapped probe near a dielectric surface, in water. We achieve thermally limited force measurement, and avoid  $1/f$  noise by using a lock-in detection method in which the external force is modulated during the measurement. The position of the particle is read out using a previously described calibrated total internal reflection microscopy (TIRM) [61] method, enabled by the addition of an anti-reflection (AR) coating to the surface which eliminates standing-wave modulation of the optical trap [42]. Probe height is scanned by displacing the trapping objective (the trap focus) relative to the chamber. Each force measurement corresponds to a spatial average over the trapping volume, giving a height resolution of about 10 nm.

## 6.2 FORCE MEASUREMENT WITH A COMPLIANT PROBE

The linear response of a compliant probe to an external force, discussed previously in Chapter 2, can be described by its mechanical susceptibility  $\chi(\omega)$ , which, for an optically trapped sphere in liquid, can be approximated as,

$$\chi(\omega) = \frac{1}{\kappa - m\omega^2 + i\gamma\omega}, \quad (6.3)$$

where  $m$  is the mass of the probe,  $\kappa$  is the spring constant of the harmonic

potential and  $\gamma$  is the drag coefficient. For a sphere of radius  $r$ , in a fluid with viscosity  $\eta$ , the drag is given by Stokes law,  $\gamma_\infty = 6\pi\eta r$ . The presence of a planar boundary near the sphere results in an increased, height-dependent drag coefficient and requires a modification to Stokes law which was described in Chapter 5. Knowledge of  $\chi(\omega)$  allows one to infer the force on such a probe from a measurement of its displacement, according to the relation  $\tilde{F}(\omega) = \tilde{x}(\omega)/\chi(\omega)$ . For time scales longer than the momentum relaxation time,  $\tau_p = m/\gamma$ , the mass term in Eq. 6.3 is negligible, and the forces are dominated by viscous damping and the restoring force of the harmonic trap. This is the case in our experiment, where  $\tau_p$  is below 1  $\mu$ s.

The magnitude of fluctuations of the thermal force, given by Eq. 6.1, is determined only by the dissipative component of the mechanical response, and is spectrally flat. A series of repeated time-averaged measurements of duration  $t_m$ , of a constant force, with such background noise, will have a variance of  $S_F^{\text{tot}}(0)/t_m$ . In practice, however, measurement noise at low frequencies is typically dominated by additional 1/f noise sources, the presence of which causes the variance of repeated measurements to diverge. For a detailed noise discussion, please refer to Section 6.7.5.

The effect of low frequency noise can be reduced by modulation of the driving force at a constant frequency  $\omega_0$ , at which the noise is dominated by thermal noise. In order to extract the signal from the noise, a lock-in algorithm is used. The lock-in signal is generated by time-averaging of the product of the position measurement  $x(t)$  and a normalized reference signal  $r(t)$ , proportional to the external force. Repeated measurements using this method will have a variance of  $S_x(\omega_0)/t_m$ , allowing the measurement to be shifted to a spectral range where 1/f noise is negligible.

### 6.3 OPTICAL FORCE ON A SPHERE IN AN EVANESCENT FIELD

The optical force exerted by an evanescent field on matter has attracted significant attention in recent decades[2, 39, 51], and though general qualitative agreement

has been found between Mie theory and observations, due to instrumental limitations, precise quantitative tests have not been made as of yet.

The force on a dielectric sphere in such an optical environment consists of two terms: a gradient force and a scattering force. The gradient force pulls the particle towards the surface and is proportional to the gradient of the field, whereas both the direction and amplitude of the scattering force depend on the scattering properties of the sphere. In the Rayleigh approximation, i.e., when the size of the particle is much smaller than the wavelength of light ( $k_o a \ll 1$ ), this scattering force is directed parallel to the surface. In the Mie regime ( $k_o a \geq 1$ ), on the other hand, the incident field can be scattered in every direction, so the scattering force contains components both parallel and perpendicular to the surface. In our experiments,  $k_o a \approx 1$ . Therefore, we must analytically evaluate the scattered fields of the dielectric sphere using Mie Theory to calculate the resulting optical force by means of an algebraic combination of the Mie scattering coefficients, following the formalism derived in Ref. [6]. A more detailed view of Mie theory and the relevant analytical calculations can be found in Chapter 1 and Section 6.7.8.

#### 6.4 SETUP

A simplified schematic of the experimental setup is shown in Fig. 6.4.1. The setup is similar to that in Chapter 5 with a few key changes. The experiment continues to be performed in a  $25 \mu\text{m}$  deep microfluidic chamber with one inlet and one outlet with AR coating on the lower surface. Again, the method for fabricating these chambers is discussed in the Appendix.

The chamber is mounted on a  $60^\circ$  BK-7 glass prism with refractive-index matching fluid in the interface, providing optical access to the lower water-glass interface of the chamber for the detection and actuation beams at angles of incidence beyond the critical angle.

Trapping is achieved using a single-beam optical tweezer formed by a 10 mW, 660 nm laser (Newport LQC660-110C) focused inside the chamber, from above,

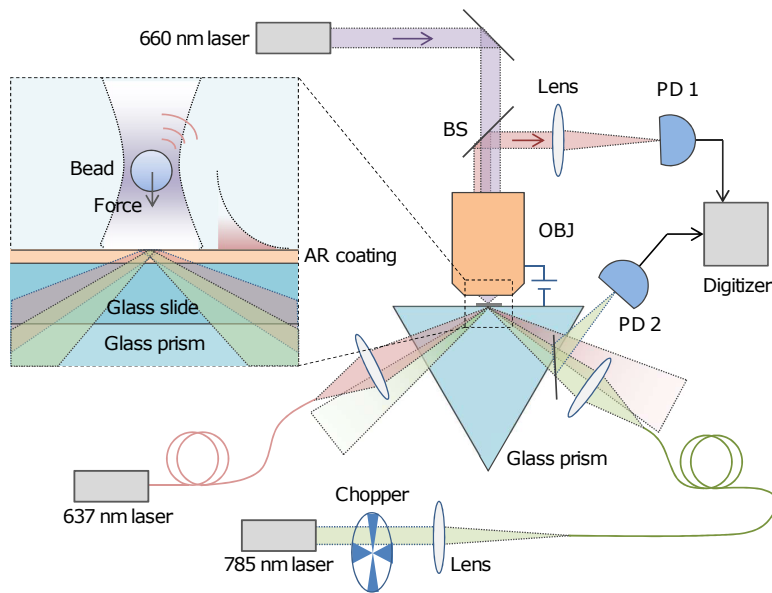


**Figure 6.4.1:** An optical trap is formed by a 660 nm laser beam focused by a high-NA water immersion objective (OBJ). The trap confines polystyrene microspheres in water near an AR coated glass surface. The bead-surface separation is controlled by vertical translation of the objective. A low-intensity evanescent wave used for detection is produced by total internal reflection of a 637 nm (probe) beam. Probe light scattered by the particle is collected by the objective and sent to a low-noise photodiode (PD1). A second, high intensity, 785 nm (pump) evanescent wave exerts a downward gradient optical force on the particle. A chopper modulates the intensity of the pump beam, which is monitored by PD2. This signal and the detection signal are digitized and recorded by a computer for lock-in signal processing.

by a water-immersion objective (Leica PL APO  $63\times/1.20$  W CORR) with numerical aperture (NA) of 1.2.

The evanescent detection field is formed by a low power ( $< 1$  mW) *p*-polarized 637 nm wavelength beam from a fiber-pigtailed laser (Thorlabs LP637-SF70). This probe beam reflects at the glass-water interface below the trapping area at an angle above critical ( $\theta_c = 61.04^\circ$ ). The spot-size of this detection beam was measured to be about  $0.13\text{ mm}^2$ , corresponding to an intensity of  $0.75\text{ W/cm}^2$  at the surface. Probe light scattered by the particle is collected by the objective and coupled into a  $60\text{ }\mu\text{m}$  diameter multi-mode fiber, which defines an aperture with an effective diameter of  $4\text{ }\mu\text{m}$  in the image plane. The fiber output is sent to a

high-sensitivity photodetector (New Focus 2151) with a transimpedance gain of  $2 \times 10^{10}$  V/A. This signal is used to track the particle's separation from the surface.

Actuation of the microsphere is performed using a second, higher power,  $\sim 100$  mW, 785 nm “pump” laser (Thorlabs LD785-SH300) whose beam enters the other side of the prism. It is focused onto an area of about  $0.014\text{ mm}^2$ , resulting in typical intensities of several kW/cm<sup>2</sup>. The pump amplitude is modulated by a chopper upstream of the fiber coupler. A 2% beam splitter is used to deflect a part of the beam into a monitor photodiode, providing the reference signal for lock-in measurement.

Since the intensity of the pump field is about 1000 times higher than that of the probe, any optical force from the probe beam can be neglected.

A capacitive displacement sensor mounted between the objective mount and sample holder is used to implement an active, low frequency feedback loop to stabilize the lens-sample separation, which is controlled by a piezo-actuated translation stage. In the presence of feedback, fluctuations in focal position of the optical trap were reduced from that of order 100 nm in 10 min to below 5 nm in 60 min.

## 6.5 DATA ACQUISITION AND ANALYSIS

Measurements reported below were acquired with optically trapped non-functionalized polystyrene (PS) microbeads suspended in de-ionized water. Typical trap lifetimes were observed to be several hours, limited by eventual diffusion of additional particles into the trapping volume. Stable trapping enabled multiple repeated acquisitions for the same microsphere. A typical data acquisition procedure for a given trapped bead consists of an initial calibration scan [42] followed by lock-in force measurements for different values of trap position and pump beam intensity.

During force measurements, the particle tracking photodiode signal is recorded simultaneously with that of the pump beam monitor photodiode, which

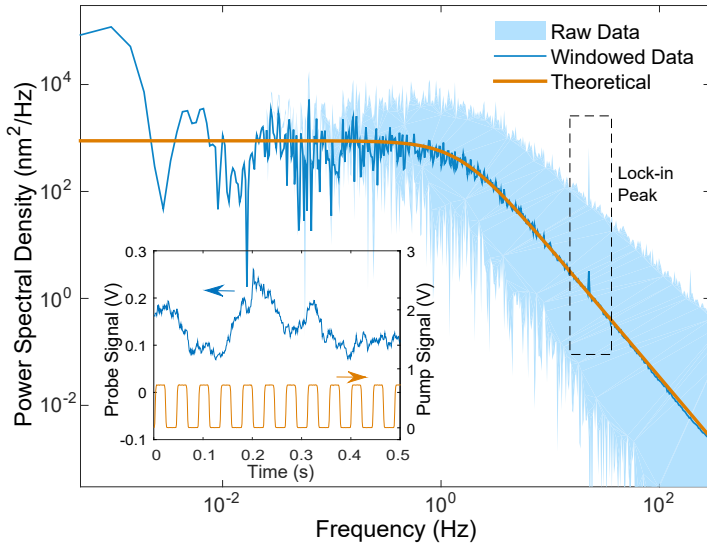


**Figure 6.4.2:** Power spectral density (PSD) of the position fluctuations of an optically trapped and optically driven Brownian probe. At low frequencies  $1/f$  noise dominates and the PSD deviates from theory. A lock-in peak centered at approximately 23 Hz is visible in the frequency domain though the driven motion is obscured by thermal fluctuations in the time domain, as illustrated by the inset. The lock-in amplitude is determined algorithmically using the pump reference signal.

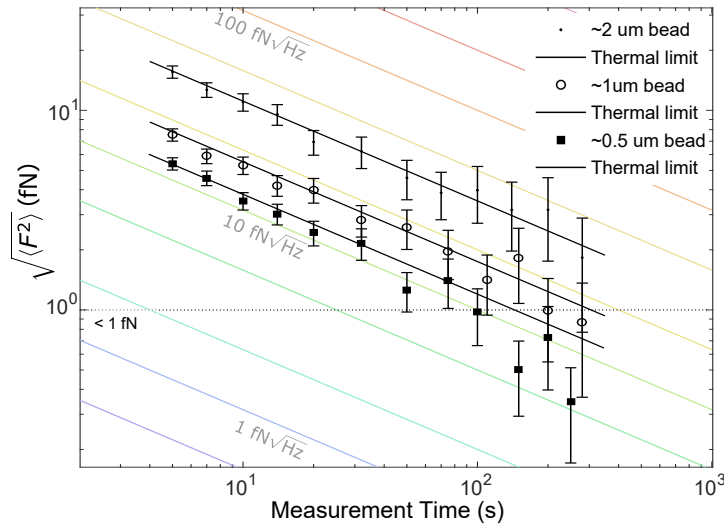
forms the reference signal for the lock-in measurement described above. The output of the lock-in algorithm is the phase and amplitude of the driven oscillation of the probe's position. In order to convert to force, an additional calibration step must be performed to determine the  $\chi(\omega)$  in Eq. (6.3). The height-dependent susceptibility is found using  $S_z(\omega, z)$ , the PSD of the Brownian motion of the probe acquired at different heights, as exemplified by Figure 6.4.2. Additionally, the resulting  $\gamma(z)$  is used to determine the diameter of each microsphere by fitting to a near-wall hindered diffusion model, with diameter and point of contact as fitting parameters.

## 6.6 RESULTS

In order to quantify the statistical fluctuations of force measurements, and to compare them to the predicted fluctuations due to the thermal force, we perform

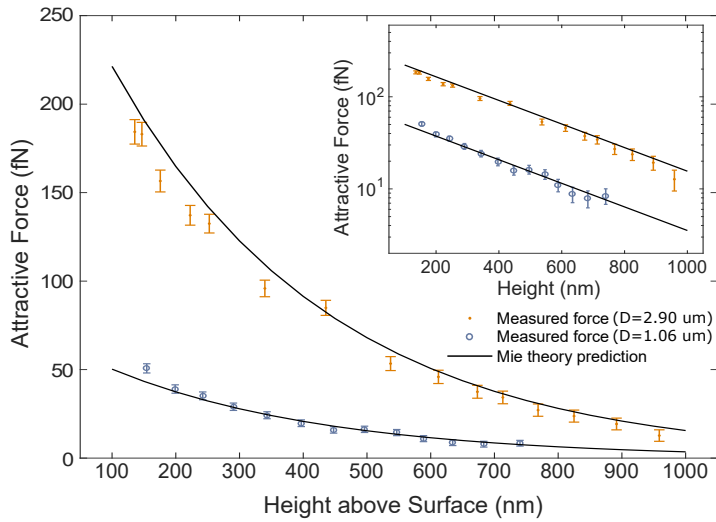
successive measurements of a constant force.

Figure 6.6.1 shows the RMS force fluctuations as a function of measurement time ( $t_m$ ) for three microspheres with nominal diameters of 500 nm, 1  $\mu\text{m}$ , and 2  $\mu\text{m}$ , trapped 700 nm from the surface in the presence of a constant (oscillating), attractive optical force. The solid curves give the prediction of Eq. 6.2, and demonstrate that the fluctuations observed in our experimental data are primarily thermally limited. The thermal limit for a smaller particle is itself smaller due to the reduced value for  $\gamma$ , which is, to first order, proportional to the particle diameter. For measurement times near and above 100 s, the RMS error for the smallest particle drops below 1 fN.



**Figure 6.6.1:** Measured RMS uncertainty in force as a function of measurement time for three beads of different radii. Each data point is obtained by calculating the standard deviation of a series of repeated independent measurements resampled from a 1000 second time series. The maximum number of independent measurements used is 25 (for the shortest time points) and minimum is 5 (for the longest time points). Comparisons are made with the predicted thermal noise limit calculated from measured damping coefficients (solid lines). Contour lines of constant damping strength ( $\gamma$ ) are shown in the background in color. Dotted line indicates 1 fN level.

Figure 6.6.2 shows results of measured (attractive) optical force exerted by the near-field of the totally internally reflecting 785 nm pump beam. Each data point



**Figure 6.6.2:** Measured optical force on a  $2.90 \mu\text{m}$  and a  $1.06 \mu\text{m}$  diameter polystyrene bead in the presence of an evanescent field. The angle of incidence of the pump beam used to generate the optical force was measured to be  $62.1^\circ \pm 0.1^\circ$  from normal for both measurements (above the critical angle of  $61.04^\circ$ ). Solid lines represent analytical Mie theory prediction of the attractive optical force in the corresponding system. The inset displays the same data on semilog axes.

was obtained from a 100 s long measurement at fixed bead-surface separation. The error bars show the thermal limit, confirmed to be equivalent to our force resolution in Figure 6.6.1. The measured force is shown alongside the results of Mie theory calculations (solid curves) based solely on measured parameters. These parameters are, specifically, the microsphere diameter, the pump laser angle of incidence and field intensity at the surface.

The microsphere diameters, determined by fitting to the hindered diffusion model, were  $1.06 \pm 0.02 \mu\text{m}$  and  $2.90 \pm 0.06 \mu\text{m}$ . The pump angle of incidence,  $\theta_p$ , is determined by measurement of the decay length of the evanescent field via confocal detection of the scattered light (blocked by a bandpass filter during normal acquisition). It was determined to be  $62.1^\circ \pm 0.1^\circ$ . The field intensity at the surface was estimated from measurement of the laser power incident on the prism, the beam profile at the lower surface of the chamber, and the reflection and propagation losses through the prism. The resulting peak intensities are (1.49

$\pm 0.16$ ) and  $(1.66 \pm 0.17)$  kW/cm<sup>2</sup> for the larger and smaller beads, respectively. Uncertainty in the power meter measurement and beam waist determination are the main sources of error.

Data for the 1.06  $\mu\text{m}$  microsphere are a near exact match with theory and results for the 2.90  $\mu\text{m}$  microsphere are close to predicted as well, scaled by a factor of 0.85, which may be attributed to a small pump beam misalignment. Within uncertainties, our experiment confirms Mie theory predictions, and is, to our knowledge, the first such experiment to find precise quantitative agreement between predicted and measured optical forces from an evanescent field.

## 6.7 CONCLUSION

We have developed a novel technique for conducting thermal-limited force spectroscopy using optically trapped microspheres. We have used it to measure the height dependence of the attractive force of an evanescent wave on a dielectric microsphere, demonstrating quantitative agreement with Mie theory. We have demonstrated resolution of angstrom-scale probe displacements and the detection of sub-femtonewton optical forces in aqueous environments at room temperature, surpassing the sensitivity (in N/ $\sqrt{\text{Hz}}$ ) of existing techniques by two orders of magnitude.

The improvement makes accessible many optical phenomena of interest, including measurement of lateral spin momentum forces, chiral-sorting forces [11, 31, 76]. Though our demonstrations were limited to optical forces at visible wavelengths, the technique is broadly applicable to near-IR wavelengths suitable for biological samples and to any force which can be externally modulated, that is, turned on and off. This modulation can be achieved, for example, by optical, mechanical, or electrical activation of biological or chemical systems. That the method is also minimally invasive, contact-free, and can be performed in fluid at room temperature is of particular interest to the biological community. It may enable exploration of the potentially important role played by femtonewton forces in DNA structure formation and cellular function and

motility [1, 5, 17].

# Additional Information

## 6.7.1 LOCK-IN ALGORITHM

The lock-in algorithm was implemented using MATLAB and is used to estimate the amplitude and phase of a sinusoidal signal obscured by noise, using a reference signal - in this case the output of the monitor photodiode which records the intensity of the chopper-modulated pump beam.

The first step of the algorithm is to generate a sin wave which is in-phase with the square wave and has unity amplitude. The zero-crossings of the square wave are determined by locating the peaks of the time-derivative of the square wave. These peaks are used to infer the phase as a function of time  $\varphi_i$ ; a sawtooth wave with amplitude  $2\pi$  whose phase matches that of the reference wave.

The noisy (discrete) signal  $z_i$  is multiplied by a complex reference signal,  $\exp[i\varphi_i]$ , resulting in the complex lock-in signal  $l_i = z_i \exp[i\varphi_i]$ . For times  $t_m \gg 2\pi/\omega_L$ , the amplitude of the signal is estimated by taking the time-average of the lock-in signal.

In order to correct for the phase delay caused by differences in the signal pathways between the pump monitor photodiode and the TIRM detection photodiode, the delay was directly measured and compensated in the data analysis. This was achieved by removing the 638 nm notch filter in front of the collection fiber for the TIRM signal. A stuck bead was positioned into the detection area, such that the scattered pump light was directly measured by the TIRM photodiode. The pump beam was chopped at several different

frequencies, and the collected signal was used to determine the frequency-dependent phase delay between the two signals.

The output of the lock-in algorithm corresponds to the amplitude of the signal at the frequency corresponding to the fundamental frequency of the square wave with which the pump beam is modulated. The coefficient of the first term of the Fourier series expansion of a square wave is larger than the amplitude of the square wave, by a factor of  $\pi/4$ . The force we report in our results corresponds to the amplitude of this fundamental component. It is larger than the amplitude of the square wave, but smaller than the peak-to-peak height of the square wave, which corresponds to the DC force of an un-modulated beam, by a factor of  $2/\pi$ .

### 6.7.2 FITTING THE MEAN SQUARE DISPLACEMENT (MSD)

The position power spectral density (PSD),  $S_x(w)$ , is defined as the Fourier transform of the auto-correlation function  $\langle x(t)x(0) \rangle$ ,

$$S_x(w) = \int_{-\infty}^{\infty} dt e^{i\omega t} \langle x(t)x(0) \rangle \quad (6.4)$$

The position autocorrelation function is then related to the mean-squared displacement (MSD) by,

$$\text{MSD} = \langle (x(t) - x(0))^2 \rangle = 2\langle x^2 \rangle - 2\langle x(t)x(0) \rangle \quad (6.5)$$

where  $\langle x^2 \rangle$  is the variance of the function  $x(t)$ .

For a Brownian particle driven by an oscillating force, ignoring inertial effects, the mean square displacement is given by

$$\text{MSD}(t) = \frac{2k_B T}{\kappa} [1 - e^{t/\tau_c}] + (2A)^2 [1 - \cos(\omega_L t)], \quad (6.6)$$

where  $\tau_c = \gamma/\kappa$ .

The damping coefficient  $\gamma$  and trap stiffness  $\kappa$  are extracted from the time-series data using a least-squares fit to the MSD of the Brownian particle. The

lock-in amplitude  $A$  and frequency  $\omega_L$  are set to the values determined using the lock-in algorithm described above. Figure 6.7.1 shows an example of such a fit. One fit is performed per measurement at a given height.

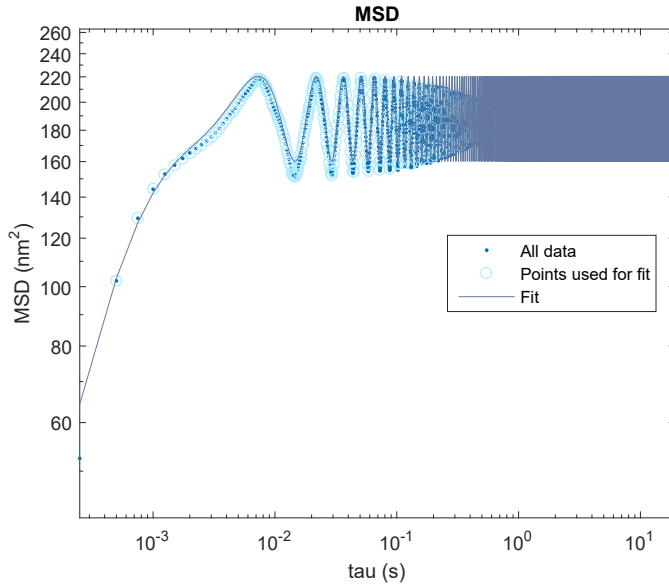


**Figure 6.7.1:** Fit to MSD of a  $2 \mu\text{m}$  PS particle in fluid. Measurement time is approximately 100 s. The particle is confined in an optical tweezer and driven by a 17 Hz optical force.

### 6.7.3 HEIGHT-DEPENDENT TRAP SPRING CONSTANT

There is also a dependence of the optical tweezer spring constant on the particle's separation from the surface, see Figure 6.7.2. This dependence has two contributions.

The first, at intermediate heights above the surface ( $\sim 300\text{-}1000 \text{ nm}$ ), manifests itself as a periodic modulation of the spring constant around some average value, and is due to residual reflection of the trap at the glass-water interface. In a sense, by measuring the modulation of the trap stiffness in this manner, we are able to judge the relative effectiveness of our AR coating.

In the second region, at very close separations less than 300 nm from the surface, the spring constant increases sharply. It is at this height that, typically, the particle's electrostatic repulsion from the surface due to interacting double layers begins to modify the trap potential. As the particle is brought closer to the surface in this regime, the double layer interaction shifts the equilibrium position of the probe, potentially away from the objective's focus. We can quantify the magnitude of this shift by comparing the expected bead height (assuming it moves in step with the trap focus) with the actual bead height (measured using the calibrated evanescent wave). Usually, when this shift becomes greater than 25 nm, or the typical RMS variation of bead position while trapped, the measurement is stopped. In this way, analytical problems which may arise working with an asymmetric potential are also avoided.

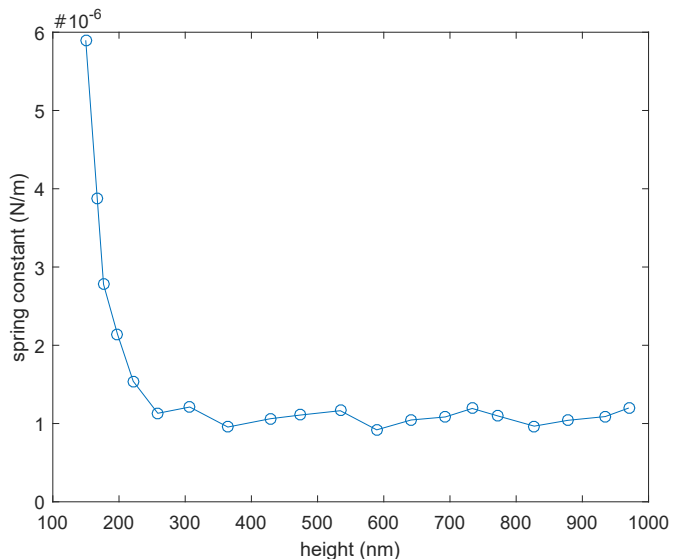


**Figure 6.7.2:** Fitted trap stiffnesses,  $\kappa$ , in the vertical direction as a function of height. The line is to guide the eye.

#### 6.7.4 FORCE NOISE SPECTRUM OF A BROWNIAN PROBE

The fluctuation dissipation theorem relates the equilibrium thermal fluctuations of a system to its linear response to an external force. Dissipation of kinetic energy of the probe is mediated by coupling to the many mechanical modes of the fluid. Thermal excitation of these mechanical modes results in the reverse process, transfer of kinetic energy from the fluid to mechanical motion of the probe. Both phenomena are mediated by the same mechanism, and in fact the magnitude and dynamics of one can be written in terms of the other.

The response of a probe's motion to an external force can be described by the mechanical susceptibility,  $\chi(\omega)$ . For a monochromatic force turned on at  $t = -\infty$ ,  $F(t) = \text{Re}[F_0 \exp(-i\omega t)]$ , the resulting motion of the particle will be at the same frequency, with a phase shift:  $x(t) = \text{Re}[\chi(\omega) F_0 \exp(-i\omega t)]$ .

The dynamics of a trapped microsphere in fluid can be described by the equation of motion of a damped harmonic oscillator:

$$m\ddot{x} = -\kappa x - \gamma \dot{x} + F_{ext}, \quad (6.7)$$

where  $m$  is the effective mass of the particle, taking into account the inertial mass of the displaced fluid, and changes in velocity are assumed to occur at time scales larger than  $\tau_f$ , the vortex diffusion time in the fluid, such that the damping force of the fluid can be approximated to respond instantaneously to changes in velocity [40]. The resulting mechanical susceptibility is:

$$\chi(\omega) = \frac{1}{\kappa - m\omega^2 + i\gamma\omega} \quad (6.8)$$

For timescales longer than  $\tau_c$  and  $\tau_p$ , one can neglect the inertial term  $m\omega^2$  since it is dominated by the damping and harmonic force.

The statistics of the fluctuations of a stationary process  $u(t)$  can be described by the power spectral density (PSD),

$$S_u = 2 \lim_{t_m \rightarrow \infty} \langle \hat{u}_{t_m}(\omega) \hat{u}_{t_m}^*(\omega) \rangle \quad (6.9)$$

where  $\hat{u}_{t_m}(\omega)$  is the truncated Fourier transform of  $u(t)$  over time  $t_m$ :

$$\hat{u}_{t_m}(\omega) = \int_{-t_m/2}^{t_m/2} u(t) e^{i\omega t} dt \quad (6.10)$$

and  $\langle \dots \rangle$  denotes the expected value over many realizations of the stationary process.

The factor of 2 in equation 6.9 corresponds to the single sided PSD convention; for real  $u(t)$ ,  $\hat{u}_{t_m}(\omega) \hat{u}_{t_m}^*(\omega)$  is symmetric in  $\omega$ , and thus

$S^{(1)}(\omega) = S^{(2)}(\omega) + S^{(2)}(-\omega) = 2S^{(2)}(\omega)$  for  $\omega \geq 0$ , where  $S^{(1)}$  and  $S^{(2)}$  denote the single- and double-sided PSD, respectively.

The fluctuation dissipation theorem relates the mechanical susceptibility  $\chi(\omega)$  of the particle to the thermal fluctuations of its position,  $S_x^{th}(\omega)$  or of the thermal force which drives those fluctuations,  $S_F^{th}(\omega) = S_x^{th}(\omega) |\chi(\omega)|^{-2}$ :

$$S_x^{th}(\omega) = \frac{4k_B T}{\omega} \text{Im} [\chi(\omega)] \quad (6.11)$$

$$S_F^{th}(\omega) = \frac{4k_B T}{\omega} \text{Im} \left[ \frac{1}{\chi(\omega)} \right]. \quad (6.12)$$

The resulting single-sided thermal noise PSD for our system is  $S_F^{th}(\omega) = 4\gamma k_B T$ . In the case that time-dependent damping must be taken into account, which is the case for velocity fluctuations at time scales on the order of  $\tau_f$ , the damping term has frequency dependence and the thermal force deviates from that of flat white noise.

### 6.7.5 NOISE IN A DC FORCE MEASUREMENT

The effect of a low pass filter on a signal  $x(t)$  can be written as a convolution with a window function  $B(t)$

$$w(t) = x(t) \otimes B(t) \quad (6.13)$$

It can be shown that the variance of a low-pass filtered signal is

$$\text{var}(w) = \int_0^\infty |\hat{B}(\omega)|^2 S_x \frac{d\omega}{2\pi}, \quad (6.14)$$

Where  $\hat{B}(\omega)$  is the Fourier transform of the window function, while  $S_x$  is the power spectral density of the un-filtered signal.

If  $B(t)$  is a rectangular window function with width  $t_m$  and area 1, then  $\hat{B}(\omega) = \text{sinc}(\omega t_m / 2)$ . For an unfiltered variable with a white noise PSD,  $S_x(\omega) = S_x(0)$ , the variance of  $w$  will be  $S_x(0)/2t_m$ .

In the case of a DC force measurement with an over-damped compliant probe, the signal is  $F = \kappa x_{avg}$ , while the noise, given as the standard deviation of repeated measurements is  $\sigma_F = \kappa \sqrt{\text{var}(x_{avg})}$ . In the presence of only Brownian motion noise, if averaging time  $t_m$  is such that the measurement bandwidth  $2\pi/t_m$  is below the corner frequency  $\omega_c = \gamma/\kappa$ , the white noise approximation is valid in the frequency range selected by the filter, and thus the thermal noise will be  $\sigma_F = \sqrt{2\gamma k_B T / t_m}$ .

While the thermal force noise spectrum is effectively frequency independent, low frequency technical noise sources are almost impossible to eliminate.  $1/f$  noise can contribute orders of magnitude more noise than the thermal limit, and cannot be eliminated by a low-pass filter.

#### 6.7.6 NOISE IN A LOCK-IN FORCE MEASUREMENT

In a lock-in measurement, an oscillating force is applied to the probe:

$$F(t) = F_0 \sin(\omega_l t) \quad (6.15)$$

resulting in motion of the particle

$$x(t) = x_0 \sin(\omega_l t + \theta) + x_n \quad (6.16)$$

where  $x_o = F |\chi(\omega_l)|$ ,  $\theta = \arg(\chi(\omega_l))$ , and  $x_n$  is the thermal (non-deterministic) component of the motion of the particle.

The in-phase lock-in signal is determined by low-pass filtering the lock-in signal  $l(t)$ , where

$$l(t) = 2x(t) \sin(\omega_l t + \theta) \quad (6.17)$$

The low-passed lock in signal,  $L(t) \equiv l(t) \otimes B(t)$ , has mean of  $x_o$ . Writing  $l(t) = l_s + l_n$ , where  $l_s = 2x(t) \sin^2(\omega_l t + \theta)$  and  $l_n = 2x_n \sin(\omega_l t + \theta)$ , the standard deviation of  $L$  can be found by determining  $S_{l_n}$ , the PSD of the random component of  $l(t)$ .

The PSD of  $l_n$  can be written in terms of the PSD of  $x_n$ . By noting

$$l_n = x_n (e^{i\omega_l t + i\theta} + e^{-i\omega_l t - i\theta}) \quad (6.18)$$

It follows that the Fourier transform of  $l_n$  is

$$\tilde{l}_n = e^{i\theta} \tilde{x}_n(\omega - \omega_l) + e^{-i\theta} \tilde{x}_n(\omega + \omega_l) \quad (6.19)$$

The PSD becomes

$$S_{l_n} = 2\tilde{l}_n \tilde{l}_n^* = S_x(\omega + \omega_l) + S_x(\omega - \omega_l) \quad (6.20)$$

The two cross terms vanish because  $x_n$  is a stationary process. The variance of the lock-in force measurement is

$$\text{var}(L) = S_{l_n}(\omega = 0)/2t_m = S_x(\omega_l)/t_m. \quad (6.21)$$

Thus it follows that the standard deviation of the force is

$$\sigma_F = \sqrt{4\gamma k_B T/t_m} \quad (6.22)$$

### 6.7.7 NOISE IN A PFM FORCE MEASUREMENT

Photonic force microscopy (PFM) takes advantage of the result of Boltzmann statistics and the ergodic theorem to relate the distribution of points in space visited along a Brownian particle's trajectory to the local potential energy landscape. In the one-dimensional case, this is given by

$$p(z) = C \exp \left[ \frac{-V(z)}{k_B T} \right] \quad (6.23)$$

where  $p(z_i)dz$  is the fraction of time spent within the region  $z_i < z < z_i + dz$ ,  $V(z)$  is the position-dependent potential energy, and  $C$  is a normalization constant.

The probability density is estimated from a recorded, discretized trajectory of Brownian motion, consisting of consecutive samples  $z_i$  of the average position of the particle during time interval  $t_i < t < t_{i+1}$  of duration  $t_{i+1} - t_i = \tau_s$ . The result is a histogram  $N_j$ , where  $N_j$  is the number points along the trajectory which lie between  $z_j < z < z_{j+1}$ . This is used to estimate a discretized probability density,  $p_j\Delta z = N_j/N_{tot}$ , where  $N_{tot}$  is the total number of position samples,  $p_j$  is the average of  $p(z)$  for  $z_j < z < z_{j+1}$  and  $\Delta z$  is  $z_{j+1} - z_j$ . The potential energy landscape is then determined by equation 6.23:

$$V_i = k_B T [\log(p_i) + \log(C)], \quad (6.24)$$

where  $C$  is an arbitrary offset. The force field is then estimated by numerical spatial differentiation of  $V_i$ . The simplest method is to use the single-point derivative, resulting in

$$F_i = \frac{V_{i+1} - V_i}{\Delta z}, \quad (6.25)$$

where  $F_i$  is the spatial average of  $F(z)$  between  $z_i$  and  $z_{i+2}$ .

For many repeated trajectories of duration  $t_m$ , the experimental histograms  $N_j$  will fluctuate about the mean value. In the case that the consecutive  $z_i$  are uncorrelated, the variance of  $N_j$  will be given by  $\sqrt{N_j}$ . This is the case if the

averaging time is much larger than the correlation time of the position fluctuations of Brownian motion  $\tau_k \equiv \gamma/\kappa$ . If the averaging time is smaller than  $\tau_k$ , consecutive position samples will be correlated; the rate of acquisition of information about the potential landscape will be limited not by the experimental sampling rate but by the rate at which the particle samples new regions of space. As a result, the variance in each histogram bin will be larger than  $\sqrt{N_j}$ , approaching  $\sqrt{N_j\tau_s/\tau_k}$  for  $\tau_s \ll \tau_k$ . We have

$$N_j = N_{tot}p_j\Delta Z \quad (6.26)$$

and

$$N_{tot} = t_m/\tau_s \quad (6.27)$$

which gives the relative error on each  $p_j$

$$\frac{\Delta p_j}{p_j} = \frac{\Delta N_j}{N_j} = \sqrt{\frac{\tau_k}{t_m p_j \Delta z}} \quad (6.28)$$

where we note that the denominator inside the square root is the fraction of time spent by the particle inside the measurement volume. This propagates to an absolute error in  $V_j$ , according to equation 6.24, of

$$\Delta V_j = k_B T \frac{\Delta p_j}{p_j} = k_B T \sqrt{\frac{\tau_k}{t_m p_j \Delta z}} \quad (6.29)$$

and thus an error of the force of equation 6.25 of

$$\Delta F_j = \frac{2k_B T}{\Delta z} \sqrt{\frac{\tau_k}{t_m p_j \Delta z}} \quad (6.30)$$

In PFM force measurement there is a tradeoff between position resolution and force sensitivity. The uncertainty in the force measured by PFM scales as  $\Delta z^{-3/2}$ , where  $\Delta z$  is the width of each histogram bin and the position resolution of the force. The highest force sensitivity is achieved by defining only two histogram bins (and thus one single force measurement averaged over the entire trapping

volume) and choosing  $\Delta z$  near  $z_{th} = \sqrt{k_B T / \kappa}$  (the rms width of the probability distribution of the trapped particle's thermal motion). In this case,  $p_i \Delta z$  approaches  $1/2$ , and  $\Delta F = 2\sqrt{2\gamma k_B T / t_m}$ . Thus, the best force sensitivity achievable using PFM is comparable to that of DC or AC single-point force measurement.

For a given trap, PFM provides a method to resolve the spatial dependence of forces at length scales far smaller than  $z_{th}$ , given sufficient measurement time or sufficiently strong forces. However, in some situations it may be advantageous to instead increase the trap stiffness (thus reducing  $z_{th}$ ) and perform several single-point measurements while scanning the trap position.

In the former case, an  $N$ -point force measurement performed with spatial resolution of  $\Delta z = z_{th}/N$  will have an average uncertainty of  $N^{3/2} \sqrt{4\gamma k_B T / t_m}$ . In the latter case,  $N$  consecutive measurements, each with duration  $t_m/N$ , will each have a force uncertainty of  $N^{1/2} \sqrt{8\gamma k_B T / t_m}$  – an  $N$ -fold improvement of SNR.

#### 6.7.8 ANALYTICAL CALCULATIONS USING MIE THEORY

The sizes of particle in our experiment are comparable to the wavelength of the incident light. Therefore, we cannot resort to the Rayleigh approximation or ray theory, but rather need to use full Mie theory to calculate the optical force acting upon the spheres. In general, one would need to calculate the total field surrounding the dielectric particle, i.e., the incident and the scattered/reflected field from the particle, and subsequently integrate the Maxwell stress tensor to obtain the optical force that acts upon the sphere. However, this approach is computationally extremely complex and only converges very slowly. Therefore, Barton et al. integrated the Maxwell stress tensor as a function of general Mie scattering coefficients. In this way, they developed a method that allows for the calculation of the optical forces using an algebraic combination of the Mie scattering coefficients. Following their algorithm, the time-averaged attractive

force (towards the surface) was calculated using

$$\begin{aligned}
\frac{\langle F_z \rangle}{a^2 \epsilon_0 E_o^2} = & \operatorname{Re} \frac{i\alpha^2}{4} \sum_{l=1}^{\infty} \sum_{m=-l}^l \sqrt{\frac{(l+m+2)(l+m+1)}{(2l+1)(2l+3)}} l(l+2) \\
& \times (2n_w^2 a_{l,m} a_{l+1,m+1}^* + n_w^2 a_{l,m} A_{l+1,m+1}^* + n_w^2 A_{l,m} a_{l+1,m+1}^* \\
& + 2b_{l,m} b_{l+1,m+1}^* + b_{l,m} B_{l+1,m+1}^* + B_{l,m} b_{l+1,m+1}^*) \\
& + \sqrt{\frac{(l-m+1)(l-m+2)}{(2l+1)(2l+3)}} l(l+2) \\
& \times (2n_w^2 a_{l+1,m-1} a_{l,m}^* + n_w^2 a_{l+1,m-1} A_{l,m}^* + n_w^2 A_{l+1,m-1} a_{l,m}^* \\
& + 2b_{l+1,m-1} b_{l,m}^* + b_{l+1,m-1} B_{l,m}^* + B_{l+1,m-1} b_{l,m}^*) \\
& - \sqrt{(l+m+1)(l-m)} n_w \\
& \times (-2a_{l,m} b_{l,m+1}^* + 2b_{l,m} a_{l,m+1} - a_{l,m} B_{l,m+1}^* \\
& + b_{l,m} A_{l,m+1}^* + B_{l,m} a_{l,m+1}^* - A_{l,m} b_{l,m+1}^*).
\end{aligned} \tag{6.31}$$

The Mie scattering coefficients  $A_{l,m}$ ,  $B_{l,m}$ ,  $a_{l,m}$  and  $b_{l,m}$  in the previous equation are related to the incident (superscript  $(i)$ ) and the scattered (superscript  $(s)$ ) fields and are defined by:

$$E_r^{(i)} = \frac{a^2 E_o}{r^2} \sum_{l=1}^{\infty} \sum_{m=-l}^l l(l+1) A_{l,m} \psi_l(n_w k_o r) Y_{l,m}(\theta, \varphi), \tag{6.32}$$

$$H_r^{(i)} = \frac{a^2 H_o}{r^2} \sum_{l=1}^{\infty} \sum_{m=-l}^l l(l+1) B_{l,m} \psi_l(n_w k_o r) Y_{l,m}(\theta, \varphi), \tag{6.33}$$

$$E_r^{(s)} = \frac{a^2 E_o}{r^2} \sum_{l=1}^{\infty} \sum_{m=-l}^l l(l+1) a_{l,m} \xi_l^{(1)}(n_w k_o r) Y_{l,m}(\theta, \varphi), \tag{6.34}$$

$$H_r^{(s)} = \frac{a^2 H_o}{r^2} \sum_{l=1}^{\infty} \sum_{m=-l}^l l(l+1) b_{l,m} \xi_l(n_w k_o r) Y_{l,m}(\theta, \varphi), \tag{6.35}$$

where  $a$  is the radius of the spherical particle,  $Y_{l,m}(\theta, \varphi)$  are the spherical harmonics,  $\psi_l(r) = r j_l(r)$  with  $j_l(r)$  the spherical Bessel function, and

$\xi_l(r) = rh_l^{(1)}(r)$  with  $h_l^{(1)}(r)$  the spherical Hankel function of the first kind.

The value of these scattering coefficients was determined using a traditional Mie scattering algorithm and the infinite series was truncated at a value  $l$  for which the relative magnitude of the optical force contribution dropped below  $10^{-7}$ .

### 6.7.9 FINITE-ELEMENTS NUMERICAL SIMULATIONS

A central assumption in the preceding calculation is that the effect of back-reflected waves between the surface and particle are negligible to the magnitude of the optical force. This assumption was verified using two-dimensional finite-elements numerical simulations (COMSOL multiphysics). In a rectangular simulation domain, an evanescent wave was excited using a plane monochromatic wave that propagates at an angle of  $62^\circ$  and total internally reflects at the interface between the prism—with AR coating—and the surrounding water. The intensity of the incident wave was normalized using the intensity extracted from the experiment and the simulation domain was terminated using perfectly matched boundary conditions that absorb the scattered fields without reflection. In order to avoid enhancement of the evanescent tails inside the perfectly matched layers, the width of the simulation domain was set at  $15 \mu m$ .

The optical force that acts upon the dielectric particle was evaluated at different heights using the Maxwell Stress tensor formalism. The numerically retrieved attractive forces are shown in figure 6.7.3. The exponential decay of the forces with distance confirms the fact that multiple reflected waves do not contribute to the total force in our setup. Indeed, multiple reflections typically generate deviations from the exponential decay of the force as a function of the height. These results justify the assumption to neglect multiple reflections in the analytical calculations.

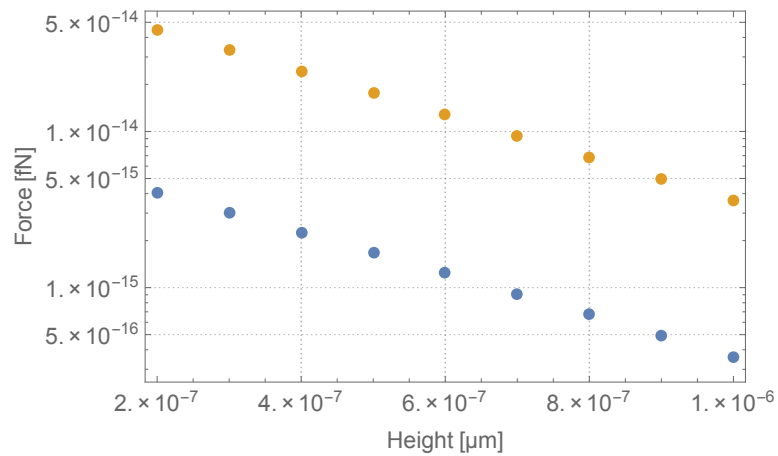


**Figure 6.7.3:** The numerically simulated attractive force (log scale) as a function of height above the surface for a 2  $\mu\text{m}$  (orange) and a 1  $\mu\text{m}$  (blue) diameter PS microcylinder. The exponential decay of the force confirms that there is no contribution of multiple reflected waves between the surface and the particles.

# 7

## Elliptical Motion of Microspheres in an Evanescent Field

WE EXAMINE THE MOTION of periodically driven, optically trapped microspheres in fluid and find a rich variety of dynamic regimes. We demonstrate, in experiment and in theory, that mean particle motion in 2D is rarely parallel to the direction of the applied force, and can even exhibit elliptical orbits with non-zero orbital angular momentum. The behavior is unique in that it depends neither on the nature of the microparticles nor that of the excitation; rather, angular momentum is introduced by the particle's interaction with the anisotropic fluid and optical trap environment. The mean angular momentum generated is measured to be comparable to what is typically achievable using structured beams, and we find overall this motion to be highly tunable and predictable.

## 7.1 INTRODUCTION

Recently, much work has gone into the investigation of optical forces on micro- and nanoparticles near surfaces, primarily in the context of an electric field localized by a micro-structured surface [4, 47, 75]. Surface-based geometries have raised theoretical excitement due to, for instance, their ability to significantly enhance optical forces [58, 72], as well as the emergence of lateral forces due to the extraordinary momentum and spin in evanescent waves [11, 31, 64]. From an applied point of view, such geometries can enable miniaturization and parallelization of efficient optical traps enabling integration into optofluidic devices [29, 49]. Moreover, light-controlled microspheres near surfaces have found applications as force transducers [23, 43, 61], pumps and switches [3], and in general their collective manipulation is an advancing field [25, 45].

However, in the case where a microparticle is within several diameters of a surface, optical and hydrodynamic surface effects cannot be neglected. Effects arising from optical coupling or reflections can complicate trapping and detection schemes [37], and hydrodynamic interactions can cause the motion of a microparticle to become highly nontrivial [66]. Despite this, little quantitative study has been done on the dynamics of optically driven particles near a surface. In studies introducing new schemes to optically manipulate matter, the particle's response function is often ignored [9, 31, 64, 77].

In this work, we investigate the dynamics of a system with both near field optical forces and surface-induced hydrodynamic effects (see Fig. 7.2.1). By driving the particle with an oscillating force from a modulated evanescent field and tracking the particle's motion closely in two dimensions, we map out a range of dynamics which can arise from the interplay of optical and hydrodynamic surface effects. We find that the magnitude and direction of the optical force depends on particle size. We also observe that the trajectory of the particle in general does not follow the direction of the force, but that its shape and orientation varies with modulation frequency and distance from the surface, a result of the anisotropy in both the hydrodynamic drag and the optical trap

spring constant.

*In particular, we discover the surprising result that elliptical motion of a microsphere can be achieved using light which does not carry orbital angular momentum.* By utilizing the inherently anisotropic mechanical environment, a linearly polarized totally internally reflecting beam is able to efficiently generate orbital angular momentum in a trapped microsphere in its evanescent field.

The measured mean intrinsic angular momentum of these trajectories agrees with linear theory predictions and is within an order of magnitude of what has been thus far reported in studies using structured light [24, 44, 71].

## 7.2 FORCES ON A DRIVEN, TRAPPED MICROSPHERE

An optically trapped microsphere in fluid, as noted in Chapter 2, is well-modeled as a stochastically driven, damped harmonic oscillator. For the purposes of this work, we generalize the result to two dimensions:

$$m^* \ddot{x}_i(t) = -\kappa_{ij}x_j(t) - \gamma_{ij}\dot{x}_j(t) + B_i(t) + F_i(t). \quad (7.1)$$

The terms on the right of Eq. 7.1 correspond, in order, to the restoring force of the optical trap, the dissipative drag in fluid, the stochastic force due to thermal fluctuations, and an externally applied force. Here, we apply a force and consider motion only in the two measured ( $x$  and  $z$ ) dimensions.

Due to the symmetries in our system, the trap stiffness,  $\kappa_{ij}$  is a diagonal tensor. For a single beam optical trap, its diagonal elements are not equal,  $\kappa_x \neq \kappa_z$ , that is, the harmonic potential is anisotropic. Usually, magnitude of the spring constant in the lateral direction is several times that of the axial one [50]. In our model describing the particle motion, we approximate that  $\kappa_i$  is a constant in  $z$ , an assumption that is generally valid until the separation becomes smaller than the Debye length in water (see Chapter 5).

In the absence of boundary effects, viscous drag,  $\gamma$ , is isotropic, given by Stokes' Law,  $\gamma_o = 6\pi\eta R$ , where  $\eta$  is the viscosity of the fluid and  $R$  is the radius of

a sphere. The presence of the boundary results in an anisotropic, height-dependent drag coefficient, discussed earlier in Chapter 5. The predicted drag in the direction perpendicular to the surface ( $z$ ) is always larger than that in the lateral direction ( $x$ ) (see Additional Information Section 7.4.3). Due to the spherical symmetry of the particle, in low Reynolds number hydrodynamics ( $\text{Re} \ll 1$ ), we may assume that the drag forces parallel and perpendicular to a plane boundary are uncoupled, such that  $\gamma_{ij}$  is diagonal with unequal elements [48].

$\vec{B}(t)$  is the fluctuating thermal force due to collisions between the microparticle and molecules of the fluid. In each dimension, the fluctuations are expected to be uncorrelated, with  $\langle B_i(t) \rangle = 0$ , where  $\tilde{B}(\omega)$  is spectrally flat. Its mean-squared magnitude is predicted by the fluctuation-dissipation theorem, discussed in Chapter 2, to be  $\langle B_i(t)^2 \rangle = 2\gamma_i k_B T$ , where  $k_B$  is the Boltzmann constant.

Lastly, the external force, which drives the periodic motion of the particle, is an optical force produced by the interaction of the microsphere with the evanescent field of a totally internally reflected TM-polarized plane wave. This force is the same optical force discussed in detail in the previous chapter (Chapter 6 Section 6.3 and Additional Information).

In summary, for small, lossless particles ( $\text{Im}[\alpha] \ll \text{Re}[\alpha]$ ), the optical force is predominantly oriented along the  $z$  direction. But as the particle increases in size, its interaction with the evanescent wave becomes more complex. In this regime, called the Mie regime, light is scattered into every direction in the  $xz$  plane. As a result, the direction of the net applied force is observed to rotate towards the horizontal direction. This can be seen in Section 7.4.6 of Additional Information.

**MICROPARTICLE MECHANICAL RESPONSE** The mechanical response of our microsphere to an applied force is frequency-dependent and can be found by solving Eq. 7.1. We continue to neglect the particle's inertia while working at time scales much larger than the momentum relaxation time,  $\tau_p = m^*/\gamma$ , as

previously discussed. Inserting a time-harmonic solution, we then find that

$$\tilde{x}_i(\omega) = \chi_{ij}(\omega) \tilde{F}_j(\omega), \quad (7.2)$$

in which we identified the mechanical susceptibility  $\chi_{ij}(\omega)$  of the system as  $(\chi^{-1}(\omega))_{ij} = \kappa_{ij} + i\omega\gamma_{ij}$ .

The motion is separable, with two different cutoff frequencies,  $f_c = \kappa/2\pi\gamma$ , in the  $x$  and  $z$  directions.

Eq. 7.2 implies that though  $F_x(t)$  and  $F_z(t)$  may be in phase, as is the case with our optically driven system,  $x(t)$  and  $z(t)$  need not. The maximum phase lag between motion in the two directions is  $\pi/2$ , making possible elliptical trajectories of the particle. Furthermore, the linearity of the system ensures that Eq. 7.2 applies whether the force is random or periodic. Thus, in our case, where the external force on our particle is composed of both a driven and a stochastic component, the thermal motion of the microsphere may be considered separately from the time evolution of the particle's mean position.

**EXPERIMENT** A schematic of the experiment is shown in Fig. 7.2.1 (also see Fig. 7.4.1 for details). The set-up is similar to that discussed in Chapter 6. All experiments are performed at room temperature in a water-filled, closed,  $25\text{ }\mu\text{m}$  deep microfluidic chamber. An anti-reflection (AR) coating is applied to the bottom glass-water interface of the chamber. Each polystyrene microsphere is optically trapped by an expanded  $660\text{ nm}$  beam from a CW laser focused through a high numerical aperture ( $\text{NA}=1.2$ ) water-immersion objective. The vertical position of the focus, and consequently the height of the trapped bead, is adjusted using a piezo. In addition to the trap beam, which enters the chamber from above, two lasers, both  $p$ -polarized, are incident from below at greater than critical angle ( $\theta_c=61^\circ$ ): a low power ( $<1\text{ mW}$ ),  $637\text{ nm}$  beam acts as the probe for the vertical ( $z$ ) position of the particle and a second laser ( $785\text{ nm}$ , around  $100\text{ mW}$  power) generates the periodic optical forces which pull on the microparticle. The second beam, which we refer to as the pump beam, is on/off

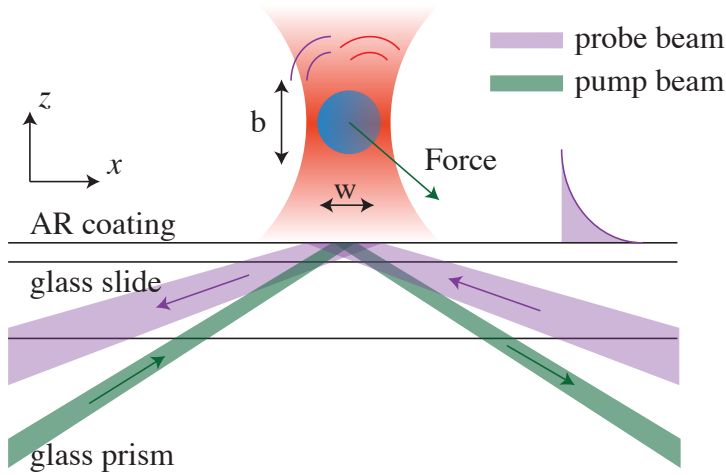


**Figure 7.2.1:** The optically trapped microsphere in its anisotropic environment. The optical trap (660 nm) has a Rayleigh length,  $b$ , larger than the beam waist,  $w$ , resulting in a restoring force approximately five times stronger in the lateral direction. Additionally, near-wall hydrodynamic coupling results in anisotropic drag which is consistently larger in the vertical direction. As a result, the particle has a different response function in the two directions. The optical force of the pump beam has components in  $z$  and  $x$ . At a driving frequency between the two cut-off frequencies, the particle's response can have large phase differences between the two directions, generating elliptical orbits. For a detailed description of the setup, see Section 7.4.1.

modulated by a chopper set to a desired frequency.

While the vertical position of the probe particle is read out in the same manner as previously described [42], for the purposes of this experiment, we modified the set-up to include, additionally, lateral position tracking. The lateral ( $x$ ) position of the particle is measured, relative to its mean position, by the displacement of the back-scattered trap beam.

The difference signal between two photodiodes of a balanced detector, each receiving, on average, half the beam, quantifies this displacement in volts. For displacements much smaller than the beam focal spot size, the relationship between the particle's lateral position and the voltage read by the balanced detector is roughly linear, that is,  $V = C_o x$ , where  $C_o$  is the  $x$ -direction calibration constant in units of V/nm [26].

Since  $C_o$  is a quantity that depends on the total power of the reflected beam as

well as the axial position of the bead relative to the trap focus, its value needs to be determined independently for each bead height [60]. We deduce  $C_o(z)$  by taking advantage of the established relationship between the diffusion coefficients in the two directions. Since at each height  $z$  the relation between  $\gamma_z(z)$  and  $\gamma_x(z)$  is known, and  $\gamma_z(z)$  can be deduced from the axial motion of the sphere [43],  $C_o$  is simply fixed at the value necessary to give the correct  $\gamma_x(z)$  for each height. A more detailed explanation of the analysis, as well as a diagram to illustrate the process, may be found in the Additional Information Section 7.4.2.

### 7.3 RESULTS

Fig. 7.3.1 plots the predicted and observed 2D trajectories of a  $2 \mu\text{m}$  PS microsphere under the influence of a periodic optical force. Predictions were made based on the optical force, mean trap stiffnesses, and bead radius fitted to experimental data. The measured trajectories are mean trajectories, extracted from 100 s measurements where each point is the averaged 2D position of the particle at a certain phase in the chopper actuation cycle.

As the frequency of the modulation is increased, several distinct behaviors are observed which can be understood in relation to the cutoff frequencies in the two spatial directions.

Below both cutoff frequencies, the position of the particle is in phase with the applied force. In this case, the particle's motion in  $x$  and  $z$  are in phase with one another and it undergoes linear oscillations with a direction determined primarily by the ratio of the trap stiffnesses  $\kappa_x/\kappa_z$ . In our case, the ratio is about 5.

Above both cutoff frequencies, the motion is again linear as the oscillations are now out of phase with the applied force in both directions. However, the direction of motion is now determined by the ratio of the damping coefficients  $\gamma_x/\gamma_z$ . As the particle nears the surface,  $\gamma_z$  diverges while  $\gamma_x$  approaches a constant value, and the motion becomes more and more parallel to the wall.

But between the two cutoff frequencies, the motions in the two spatial

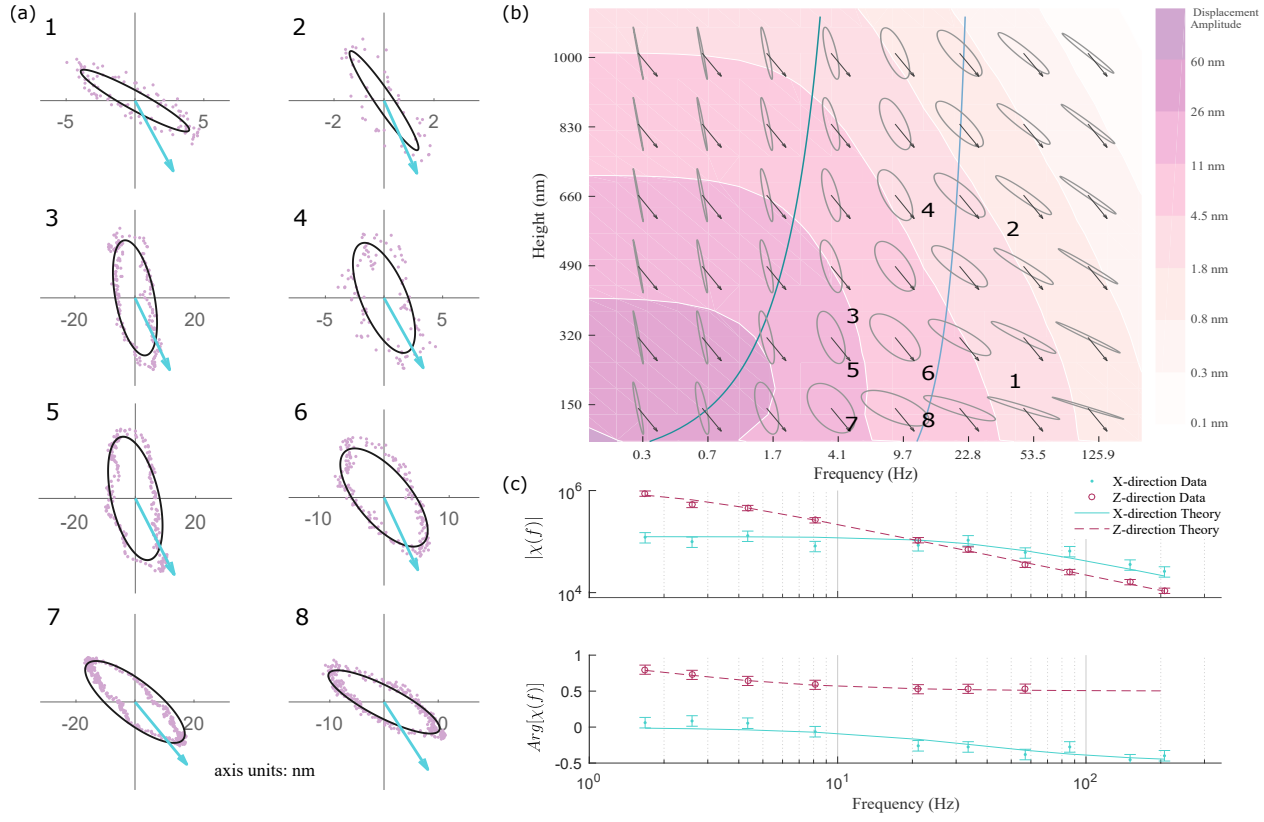


**Figure 7.3.1:** (a) Predicted and measured 2D motion of a  $1 \mu\text{m}$  radius bead when driven by a periodic optical force from an evanescent field. The blue arrows indicate the direction of the optical force. Each tile in (a) corresponds to a particular height ( $z$ ) and modulation frequency ( $\omega_0$ ), and are numbered corresponding to their location on the grid (b). The details of the measurement parameters are given in the Suppl. Mat. (b) Grid of predicted particle trajectories where the horizontal axis represents the driving frequency, and the vertical axis is the height above the surface. The displacement amplitude in nanometers is defined as the length of the semi-major axis of each orbit. Calculated cutoff frequencies in the  $x$  and  $z$  directions are drawn as blue lines. At all heights, the cutoff frequency in the  $z$  direction is lower than that in the  $x$  direction, due to a larger trap stiffness in the lateral direction. (c) Measured amplitude and phase of frequency-dependent mechanical susceptibility,  $\chi(f)$ , at a height of 400 nm, compared with predictions.

directions go out of phase with one another and stable, elliptical orbits are established.

In Fig. 7.3.2 we compare our measurements against Mie theory predictions for

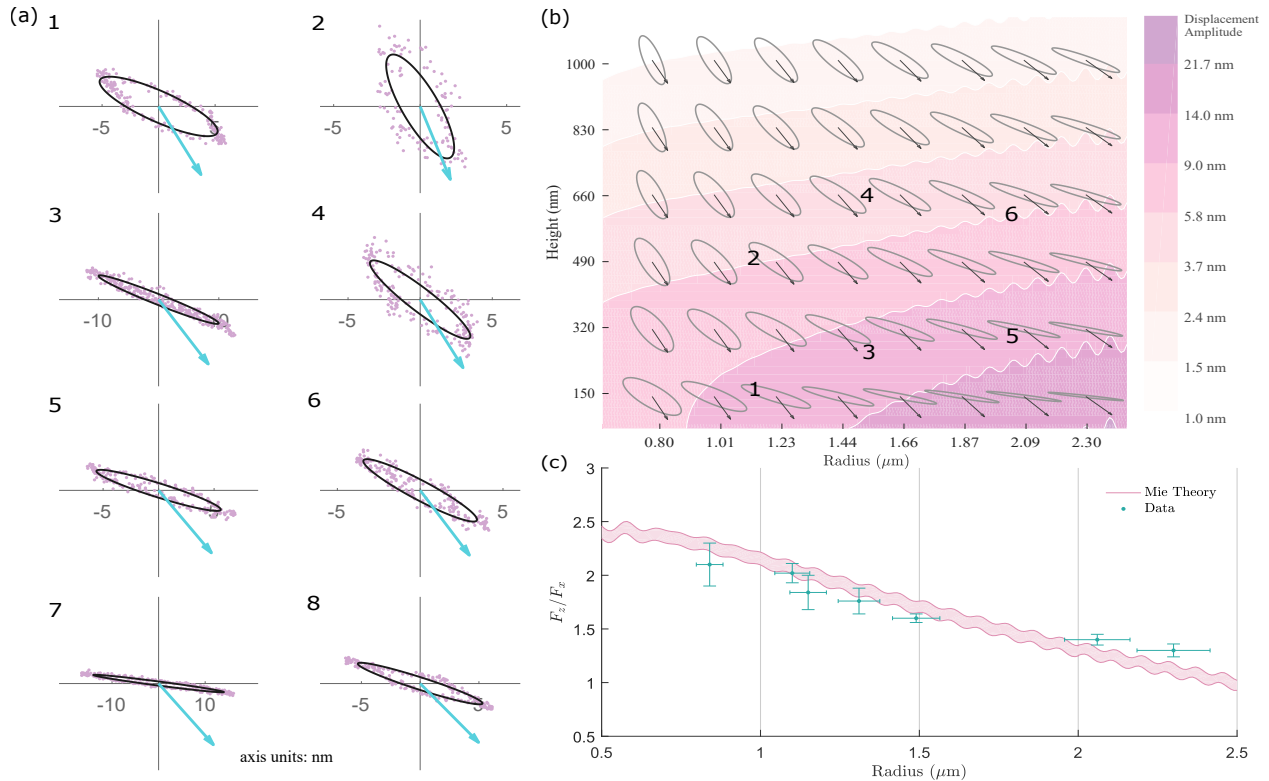


**Figure 7.3.2:** (a) Predicted and measured motion of  $0.6\text{-}2.5\ \mu\text{m}$  radius beads when driven by a periodic optical force from an evanescent field that is switched on and off at 20 Hz. The blue arrows indicate the direction of the optical force. Each tile in (a) corresponds to a particular height and bead radius, and are numbered corresponding to their location on the grid (b). The details of the measurement parameters are given in a table in the Suppl. Mat. (b) Grid of predicted particle trajectories based on Mie theory calculations, where the horizontal axis represents bead radius and the vertical axis is the height above the surface. The displacement amplitude in nanometers is defined as the length of the semi-major axis of each orbit. The trajectories labeled 7 and 8 are for a  $2.85\ \mu\text{m}$  radius bead, outside the scope of our Mie theory calculations. (c) Ratio of measured optical forces in the  $z$  and  $x$  directions compared with Mie theory. Shaded area shows the uncertainty in the microsphere index of refraction ( $n=1.575\pm0.005$ ). Generally, as microparticle radius increases, the direction of the optical force rotates towards the horizontal.

a fixed modulation frequency. As the microparticle radius increases, the net optical force from the evanescent field increases for a given field strength and configuration, and the direction of the force rotates slowly towards the horizontal. In addition, since hindered diffusion theory predicts drag near a

surface to increase as a function of the ratio  $z/R$ , where  $z$  is the separation and  $R$  is the radius, increasing radius has similar effects as decreasing separation.

Therefore, large beads tend to move parallel to the surface, regardless of their direction of excitation.

We note that the calculations performed in this section assume that the particle motion, together with the gradient of spring and damping constants, at each fixed height are sufficiently small that the parameters  $\gamma, \kappa$ , as well as the amplitude and direction of applied optical force may be treated as constants and the equations of motion considered linear. This is not generally the case, as evidenced by previous studies in detailed microsphere Brownian dynamics, e.g.[66], which reported a probability current in the position of an optically tweezed microsphere due to a non-zero curl of the force field. However, we distinguish our results from the results of the previous studies in that we measure a time-dependent, periodic shift in the particle's equilibrium position, not only a circulation of probability. As such, the measured phenomenon of our study would persist even in the absence of thermal fluctuations. In this respect, it's important to stress that in our experiment, the amplitude of measured response is about the same as the RMS position noise due to thermal fluctuations, for a signal-to-noise ratio of about 1. However, aspects of this analysis are applicable to larger amplitude oscillations and even freely moving particles near a surface.

One manner of quantifying angular motion is to consider the torque applied by the particle to the fluid,  $\tau_{app}(t) = \vec{r}(t) \times \gamma \vec{v}(t)$ , where  $\gamma$  is the tensor described in Eq. 7.1. For a particle undergoing steady-state, elliptical motion in fluid, this quantity is on average the same as the torque applied to the particle.

Fig. 7.4.8 shows  $\tau_{app}$  accumulating over 100 s for a bead driven at two different frequencies, which agree well with predictions. Another method of quantifying this angular motion is to calculate the constant, non-zero intrinsic orbital angular momentum in the steady state, given by,

$$\langle L_{in} \rangle = \omega |\tilde{x}| |\tilde{z}| \sin(\varphi_z - \varphi_x), \quad (7.3)$$

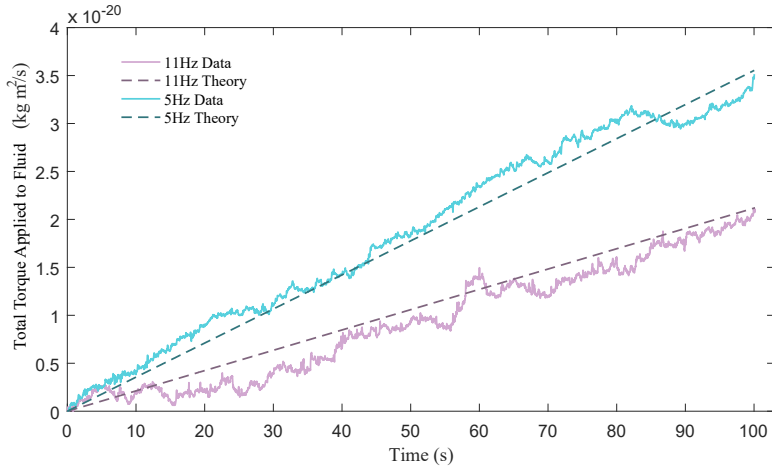


**Figure 7.3.3:** Measured and predicted torque applied to fluid integrated over time for a  $2\mu\text{m}$  PS bead driven at 11 Hz and 5 Hz frequency at a height of about 200 nm, corresponding to points [5] and [6] in Fig. 7.3.1. The force on the bead is the same in both curves.

where  $\varphi_x$  and  $\varphi_z$  are the phases of the complex mechanical susceptibilities  $\chi_x$  and  $\chi_z$  in the  $x$  and  $z$  directions, respectively, and  $\langle L_{in} \rangle$  is normalized by mass. This quantity is useful in allowing direct comparison with existing reports in literature, where we do not have access to values of the damping parameter,  $\gamma$ , but can estimate velocity and orbital radius.

In our unoptimized set-up, the largest  $L_{in}$  was measured to be  $4.9 \times 10^{-15}\text{m}^2/\text{s}$ , where  $\varphi_z - \varphi_x$  was closest to  $\pi/2$ . The configuration for this measurement was a  $2\mu\text{m}$  diameter bead driven at 4.6 Hz at a separation of around 200 nm from the surface (corresponding to point [5] in Fig. 7.3.1). In comparing this value with previous reports for dielectric particles driven by structured light, such as by optical vortices [24, 44, 55, 71], we find our value comparable when normalized by laser power. With optimization of driving frequency and bead radius, or changes in the power or wavelength of the pump beam, further gains may be expected. For details, please consult the Additional Information which follows.

## 7.4 CONCLUSION

Using a highly sensitive detection scheme, we investigated the dynamics of trapped microspheres under the influence of a periodic force. We find good agreement between our model and the measured motion and demonstrate a novel method of generating elliptical orbits with sustained, non-zero orbital angular momentum.

# Additional Information

## 7.4.1 EXPERIMENTAL SET-UP

Please see Figure 7.4.1.

## 7.4.2 ANALYSIS FLOW

The unknown parameters in our experiment (calibrated positions, lock-in amplitudes, damping coefficients and trap stiffnesses in the two spatial directions) are determined sequentially in the procedure diagrammed in Figure 7.4.2.

Calibrated positions in  $z$  follow a logarithmic relation to scattered light intensity, and are determined according to the procedure detailed in Chapter 5. In panel o of Fig. 7.4.2 the parameters are defined, the known values in black and the unknown values in red. As the analysis progresses, parameters determined in each step turn black in color, in this way, the logical progression of our process is revealed.

## 7.4.3 HEIGHT-DEPENDENT DAMPING COEFFICIENT

The below is the result from Chapter 5 on hindered diffusion generalized to perpendicular and parallel directions.

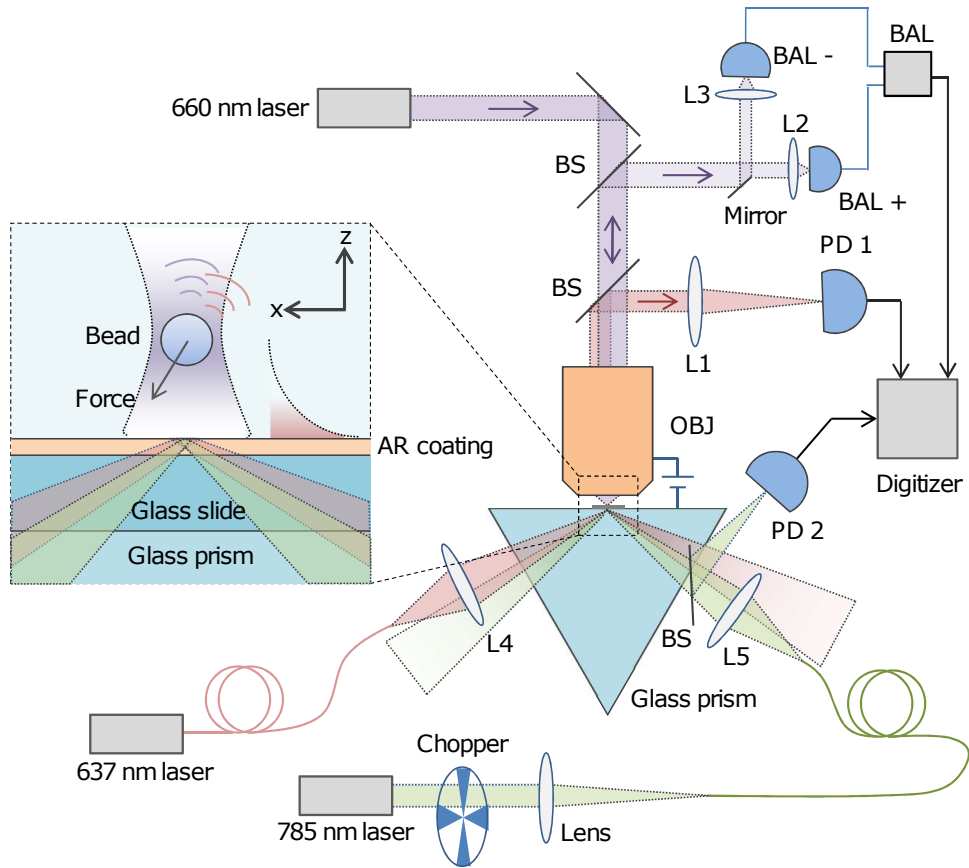


**Figure 7.4.1:** An optical tweezer is formed by the 660 nm laser beam focused by a high-NA water immersion objective (OBJ). The trap confines polystyrene micro-spheres in water near an AR coated glass surface; the back-scattered trap beam is used to determine its lateral position via a balanced detector (BAL). The bead-surface separation is controlled by vertical translation of the objective. A low-intensity evanescent wave used for vertical position detection is produced by total internal reflection of a 637 nm (probe) beam. Probe light scattered by the particle is sent to a low-noise photodiode (PD1). A second, high intensity, 785 nm (pump) evanescent wave exerts an optical force on the particle in the x-z plane. A chopper modulates the intensity of the pump beam, which is monitored by PD2. This signal as well as the signals from BAL and PD1 are digitized and recorded by a computer for lock-in signal processing.

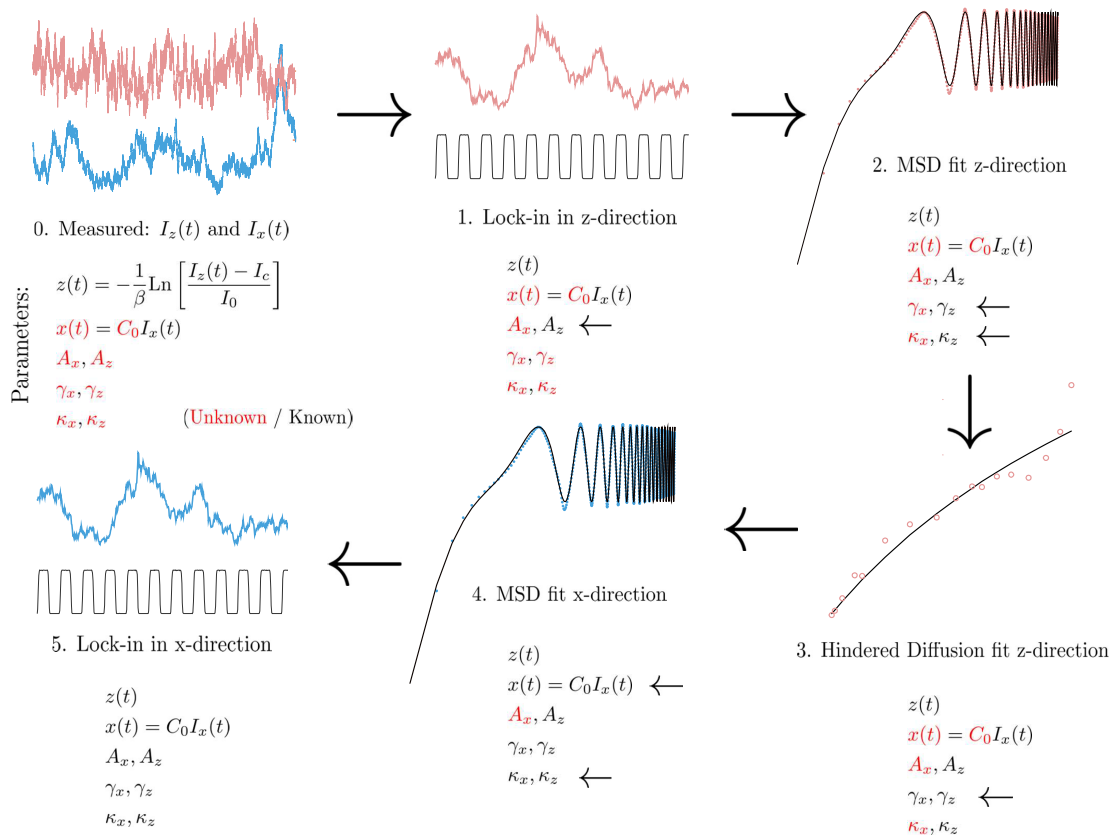


**Figure 7.4.2:** Analysis flow for determination of unknown parameters. Panel 0 describes what is known at the start of this analysis. Panels 1 and 5 refer to the lock-in algorithm described in Chapter 6. Panels 2 and 4 refer to the best fit to mean-squared-displacement (MSD) of particle position, described in the same chapter. Panel 3 references the fit to hindered diffusion model described in Section 7.4.3

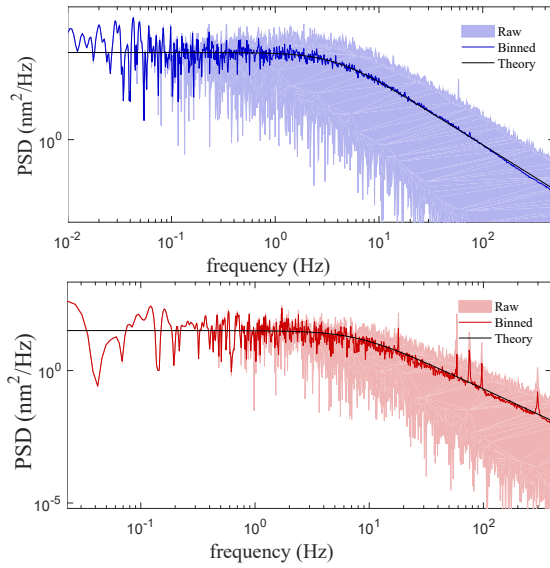


**Figure 7.4.3:** Power spectral density (PSD) in the  $z$ - and  $x$ - directions. Pictured are raw data, running average, and the predicted PSD based on fit to mean-squared displacement.

For slow motion of a microsphere in fluid in close proximity to a hard surface with no-slip boundary conditions, Brenner and Goldman derived expressions for the height-dependent viscous drag in the direction perpendicular to the wall,  $\gamma_z(z)$  [14], and in the direction parallel of the wall,  $\gamma_x(z)$  [28], as correction to the Stokes law result  $\gamma_o = 6\pi\eta R$ .

The drag is generally larger than the case with no boundary present due to hydrodynamic coupling between the sphere and the wall, and generally larger in the perpendicular direction than the parallel direction. On contact with the wall, the correction coefficient diverges for the perpendicular direction, that is,  $\gamma_z \rightarrow \infty$ , while the correction coefficient for the parallel direction reaches a constant value  $\gamma_x \rightarrow C$ . Far from the wall, the boundary's influence diminishes and  $\gamma_x(z)$  and  $\gamma_z(z)$  approach each other and the isotropic result of Stokes law. The diffusion coefficient depends inversely on the drag as  $D(z) = k_B T / \gamma(z)$ .

Although the height-dependent damping complicates force measurement, since it results in height dependence of the mechanical susceptibility and the

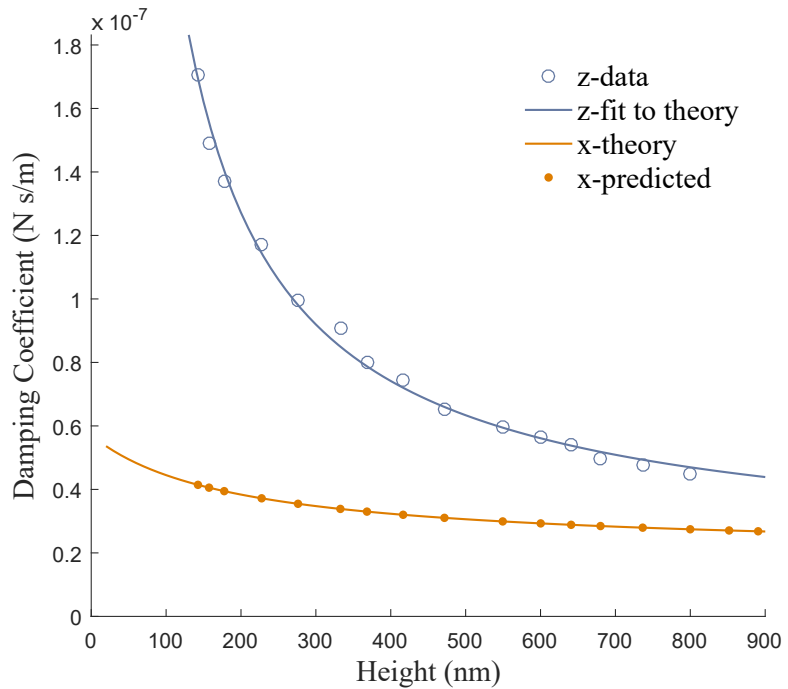


**Figure 7.4.4:** The measured perpendicular damping coefficient as a function of height above surface  $\gamma(z)$  for a PS microsphere is fit to theoretical hydrodynamic predictions [14]. The fitted radius is then used to predict the damping coefficient in the lateral direction, which is generally smaller. Fitted results yields a radius of 1.1  $\mu\text{m}$  for the sphere at a temperature of 22C.

thermal noise, we take advantage of the relationship between damping in the two directions in order to perform the calibration between signal intensity and position in the  $x$ -direction, and to better estimate the  $z = 0$  point or the point-of-contact (POC) in the  $z$ -direction.

#### 7.4.4 HEIGHT-DEPENDENT TRAP SPRING CONSTANT

In predicting the trajectories, the spring constant was assumed to be a constant independent of height. This assumption is roughly valid in the lateral direction but begins to break down in the axial direction near the surface.

At very close separations, less than 350 nm from the surface, the spring constant in the axial direction of the beam increases sharply. This is due to the particle's electrostatic repulsion from the surface arising as an additional confining force. The trap potential narrows and the particle becomes more tightly confined. Refer to Chapters 5 and 6 for discussions.

This effect is neglected in the trajectory figures in the main paper. For this reason, the trajectory predictions very close to the surface are expected to disagree somewhat from the measured results.

#### 7.4.5 NET FORCE ON MICROPARTICLES FOR VARIOUS TRAJECTORIES

Figure 7.4.6 shows the computed net force acting on a  $2.2\mu\text{m}$  radius PS microsphere under periodic forcing at various stages of its orbit. The figure shows the physical origin of these elliptical trajectories.

#### 7.4.6 OPTICAL FORCE ON A DIPOLAR PARTICLE IN AN EVANESCENT FIELD

In the dipole approximation, the force on a small, polarizable particle can be calculated analytically. The time-averaged Lorentz force acting upon a dipolar particle with radius  $a$  and permittivity  $\epsilon_p$ , surrounded by a background with permittivity  $\epsilon_b$ , consists of three terms:

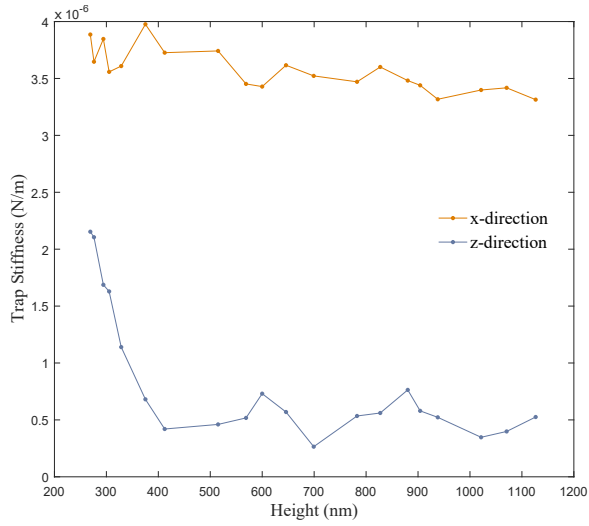


**Figure 7.4.5:** Fitted trap stiffnesses,  $\kappa_x$  and  $\kappa_z$ , in the horizontal and vertical directions as a function of height for a  $2\mu\text{m}$  radius PS particle. The line is to guide the eye.

$$\vec{F} = \frac{\text{Re}[\alpha]}{4} \vec{\nabla} |\vec{E}_o|^2 + \frac{\text{Im}[\alpha]}{2} \vec{k} |\vec{E}_o|^2 - \frac{\text{Im}[\alpha]}{2} \text{Im}[\vec{E}_o \vec{\nabla} \vec{E}_o], \quad (7.4)$$

where  $E_o$  is the amplitude of the electric field with wave vector  $k$ , and  $\alpha$  is the polarizability of the particle in the fluid. For small particles ( $ka \ll 1$ ) this polarizability can be approximated by  $\alpha = \alpha_o (1 + 2/3ik^3|\alpha_o|^2)$  with  $\alpha_o = a^3(\epsilon_r - 1)/(\epsilon_r + 2)$  and  $\epsilon_r = \epsilon_p/\epsilon_b$ .

The first term in Eq. 7.4 corresponds to the gradient force, whereas the second and the third term are scattering forces. In our setup, we consider an evanescent field generated by an internally reflected TM-polarized plane wave. In this case, the first term pulls the particle towards the surface, the second one pushes the particle along the surface in the direction of propagation, and the final term vanishes.

The ratio of these forces perpendicular to and longitudinal along the surface is

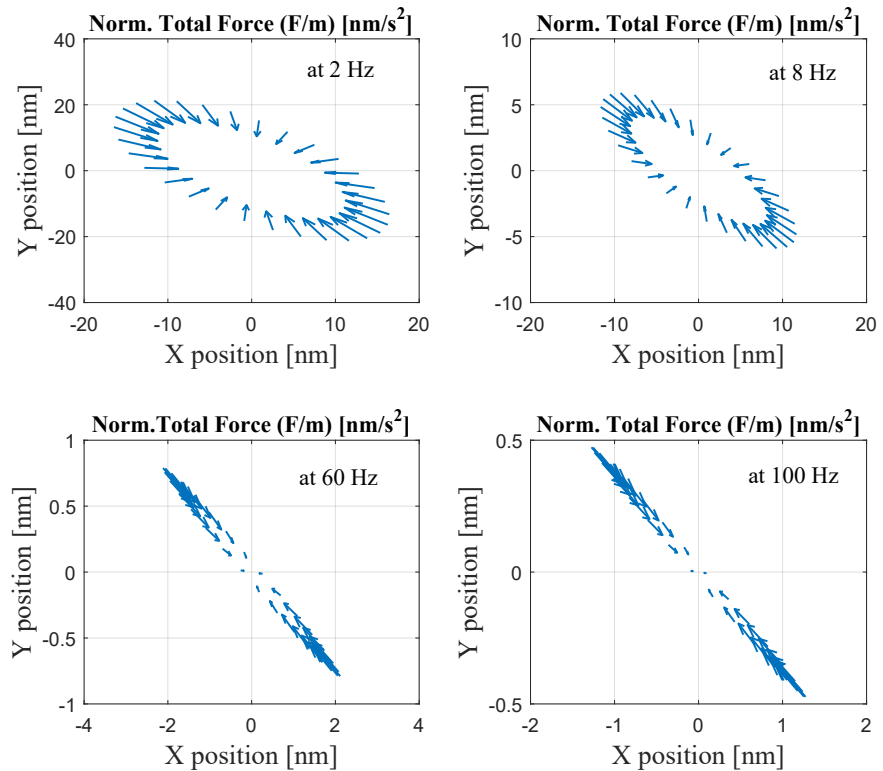


**Figure 7.4.6:** Net force normalized by effective mass of particle in  $\text{nm}/\text{s}^2$  for a few select trajectories of a 2.2  $\mu\text{m}$  radius particle actuated at frequencies between 2 and 100 Hz. Force direction and relative magnitude plotted on top of particle position at each point in the particle's orbit.

thus given by:

$$\left| \frac{F_z}{F_x} \right| = \frac{1 \operatorname{Re}[\alpha] \vec{\nabla} |\vec{E}_o|^2}{2 \operatorname{Im}[\alpha] k_x |\vec{E}_o|^2}, \quad (7.5)$$

where  $\vec{E}_o = E_o \vec{i}_E \exp[ik_x x - qz]$ .  $|F_z/F_x|$  is thus entirely determined by the ratio of the real and the imaginary parts of the particle's polarizability  $\alpha$  and the evanescent field's wave vector:

$$\left| \frac{F_z}{F_x} \right| = \frac{q}{k_x} \frac{\operatorname{Re}[\alpha]}{\operatorname{Im}[\alpha]}. \quad (7.6)$$

For a given angle of incidence,  $q$  and  $k_z$  remain fixed. The polarizability  $\alpha$  of a small particle is related to its static polarizability  $\alpha_o$  using Draine's radiation correction:

$$\alpha = \alpha_o \left( 1 - \frac{2}{3} ik^3 \alpha_o \right)^{-1} \approx \alpha_o \left( 1 + \frac{2}{3} ik^3 \alpha_o^* \right). \quad (7.7)$$

For lossless particles, the ratio of the real and the imaginary parts of the polarizability thus equals

$$\frac{\operatorname{Re}[\alpha]}{\operatorname{Im}[\alpha]} = \left( \frac{2}{3} k^3 \alpha_o \right)^{-1}. \quad (7.8)$$

The ratio of the force in the  $z$  and the  $x$  direction grows to infinity for decreasing particles radius  $a$ , as the static polarizability  $\alpha_o$  is proportional to  $a^3$ . This effect is shown in the small particle regime ( $a < 0.1\mu m$ ) of Fig. 7.4.7(b).

#### 7.4.7 OPTICAL FORCE ON A MIE PARTICLE IN AN EVANESCENT FIELD

As discussed in Chapter 1, the dipolar regime is merely a simplifying approximation of the full Mie calculation, dropping higher order terms. For the full Mie coefficients, please consult the Supplemental Information of Chapter 6.

For this experiment, the optical force was calculated in the  $x - z$  plane. The result is shown in Fig. 7.4.7(a). It is interesting to note that in the Mie regime, the longitudinal force along the surface approaches the same amplitude as the attractive force towards the surface. This is clear in the large particle regime

( $a > 0.5\mu m$ ) in Fig. 7.4.7(b) and the inset.

#### 7.4.8 DETAILS OF EXPERIMENTAL PARAMETERS IN FIG. 7.3.1 AND FIG. 7.3.2

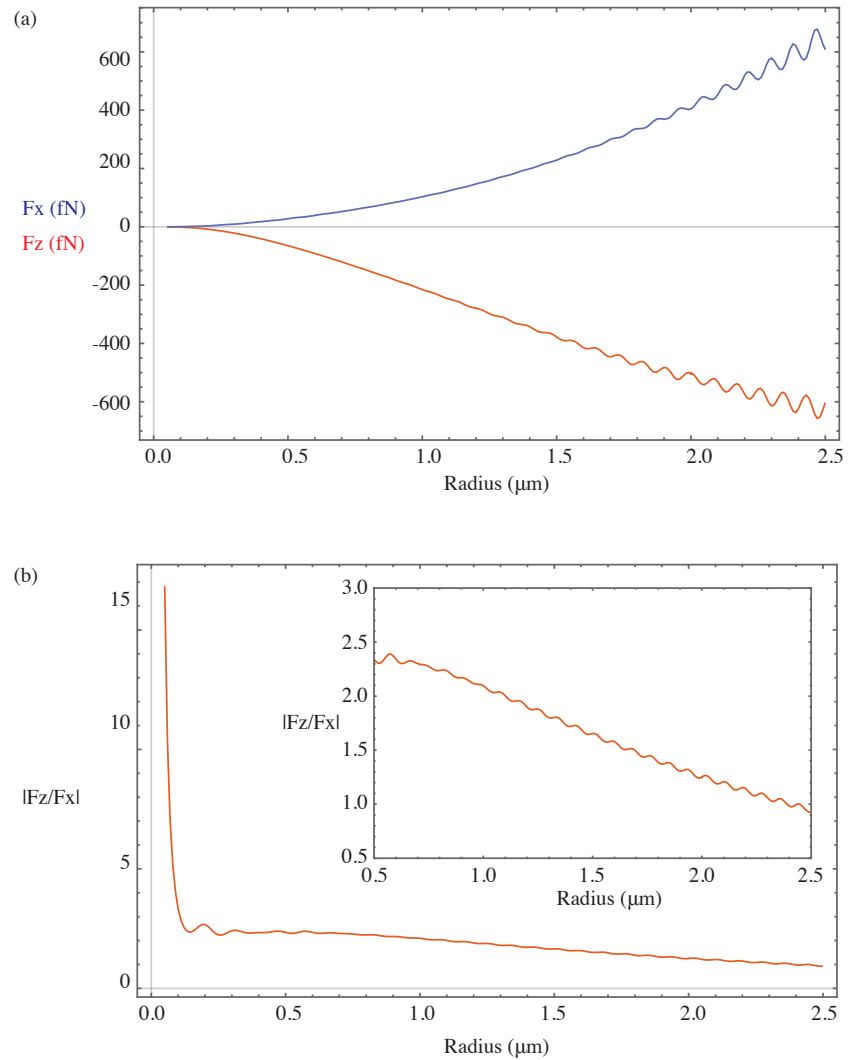
Fig 7.3.1, number	Frequency (Hz)	Height (nm)
1	46	175
2	46	500
3	5	300
4	11	600
5	5	220
6	11	220
7	5	130
8	11	150

Fig 7.3.2, number	Radius ( $\mu m$ )	Height (nm)
1	1.1	150
2	1.1	475
3	1.5	230
4	1.5	650
5	2	280
6	2	560
7	2.8	120
8	2.8	550

#### 7.4.9 ANGULAR MOMENTUM ANALYSIS

In this section, we discuss how we extract the angular momentum from the experimental data and how we compare it to our analytical model. The intrinsic angular momentum—the angular momentum per unit kg—was calculated directly by evaluating  $L = \vec{r} \times \vec{v}$ , both for the experimental data and the analytical model.



**Figure 7.4.7:** Optical forces in an evanescent field. (a) In the dipole regime ( $a < 0.1\mu\text{m}$ ), the amplitude of both the lateral and the perpendicular force monotonically increase with increasing particle size. In the Mie regime, the forces continue to grow, with signature Mie oscillations superimposed. (b) The relative amplitude of the attractive force versus the longitudinal force grows to infinity in the dipole regime. In the Mie regime, the forces in both directions are comparable in amplitude.

However, one needs to be cautious when extracting the mean angular momentum from the experimental data. The differentiation of the displacement to calculate the velocity causes a blue-shift in the noise spectrum, amplifying high-frequency noise. The data, as a result, needs to be low-pass filtered in order to be interpreted correctly. This is achieved using a triangular windowing of the velocity data in the time-domain. The resulting calculated angular momentum as a function of the windowing width is shown in Fig. 7.4.8.

In these graphs we can clearly distinguish different regimes. For low windowing widths (high frequency) noise dominates the signal. As the windowing width increases this noise is filtered out, but undersampling of the ellipse begins to affect the angular momentum resolved, causing a systematic underestimate of the true angular momentum.

To resolve this issue, we fit the curve in the low frequency regime—where the high frequency noise is filtered out—to an equivalently undersampled analytical orbit that does not contain any noise. We then extract the angular momentum of the experimental data as the angular momentum of the fitted ellipse at zero windowing width. As shown in Fig. 7.4.8, the predicted values of the angular momenta (red curves) are in excellent agreement with the experimentally fitted ones (yellow curves).

In the main text we provide an analytical estimate for the intrinsic angular momentum expected from such an analysis, which depends only on the angular frequency,  $\omega$ , amplitudes of oscillation,  $|\tilde{x}|$  and  $|\tilde{z}|$ , and the response phase difference in the two directions,  $\varphi_z - \varphi_x$ . A brief derivation is provided below:

$$\langle L/m \rangle = \langle \vec{r} \times \vec{v} \rangle \quad (7.9)$$

where the position and velocity vectors are given by,

$$\begin{aligned}\vec{r} &= |\tilde{x}| \cos(\omega t - \varphi_x) \hat{x} + |\tilde{z}| \cos(\omega t - \varphi_z) \hat{z}, \text{ and} \\ \vec{v} &= \frac{d\vec{r}}{dt} = -|\tilde{x}| \omega \sin(\omega t - \varphi_x) \hat{x} - |\tilde{z}| \omega \sin(\omega t - \varphi_z) \hat{z}.\end{aligned}\tag{7.10}$$

Taking their cross-product, simplifying, and taking the time average over each cycle then gives,

$$\langle L/m \rangle = \omega |\tilde{x}| |\tilde{z}| \sin(\varphi_z - \varphi_x)\tag{7.11}$$

We note that the calculations performed here assume that the particle motion, together with the gradient of spring and damping constants, at each fixed height are sufficiently small that the parameters  $\gamma$ ,  $\kappa$ , as well as the amplitude and direction of applied optical force may be treated as constants and the equations of motion considered linear.

#### 7.4.10 THE EVANESCENT WAVE TECHNIQUE AS A METHOD OF ANGULAR MOMENTUM GENERATION

A potentially useful application of the phenomenon observed here is the efficient generation of angular momentum without the use of structured light, or light carrying any orbital angular momentum. While we do not suggest that this method should supplant the study and use of structured light beams in colloidal systems, here we provide a detailed comparison and discuss some trade-offs between the two methods.

In our setup, we measure an intrinsic angular momentum,  $L_{in} = \vec{r} \times \vec{v}$ , of  $4.89 \times 10^{-15} \text{ m}^2/\text{s}$ . We cite two results in the literature for comparison [44, 71]. The first citation reports using a 700 mW beam to generate rotation with angular frequency 0.07 rad/s, the beads were seen to rotate within an ellipse around 5 μm in radius. Scaling down to the powers used in our experiment (80 mW), the intrinsic angular momentum equals  $2.28 \times 10^{-14} \text{ m}^2/\text{s}$ , which is about 4.7 times

our result.

The second citation reports particles rotating at 0.06 Hz around an inner ring of a Bessel beam of 2.9  $\mu\text{m}$  radius at a power of 600 mW at the sample surface. Rescaling to our power levels, this intrinsic angular momentum equals  $5.64 \times 10^{-14} \text{ m}^2/\text{s}$ , which is about 11 times our result.

Thus, our un-optimized system produced angular momentum in optically driven microparticles within an order of magnitude of previous structured-light results. If desired, the angular momentum generation in our system can be greatly enhanced by performing some simple optimizations. For instance, two orders of magnitude improvement can be expected, if, simply, the pump beam is focused so that the spot-size is shrunk by a factor of three. Currently, the low-intensity beam used for excitation has a semi-major axis of around 100  $\mu\text{m}$ . Focusing to a spot size of around 30  $\mu\text{m}$  would increase the field intensity by a factor of 10, and the angular momentum generated by a factor of 100.

In addition, our method circumvents a subtle trade-off that is associated with the use of structured light. In the case of orbital angular momentum using structured light beams, the orbital rotation rate is inversely proportional to the cube of the ring's radius [24]. In our case, however, both parameters are decoupled: our orbital rotation rate is determined by the chopping frequency, whereas the radius is predominantly determined by the beam intensity and the drag coefficients. Along the same lines, it is interesting to note that in experiments involving structured light beams the minimal radius of orbital motion is limited. Indeed, the trapping radii of a Laguerre-Gaussian mode are given by  $r_{\text{trap}} = (z_R * l/k)^{1/2}$ , where  $z_R$  is the Rayleigh range of the beam. As a result, there is a lower limit on the trapping radius and, for a fixed input power, an upper limit for the orbital rotation rate. In this way, the technique presented in our manuscript is complementary to those described in references [24, 44, 55, 71] and the ideas underlying both can be combined to extend the parameter range—radii and frequencies—of orbital angular momentum generation of microparticles using optical forces.

Finally, we must be careful to distinguish our results from that of Roichman, et.

al. [66], which reported a probability current in the Brownian motion of an optically tweezed microsphere due to a non-zero curl of the force field. We, instead, measure a deterministic, time-dependent, periodic shift in the particle's mean position. As such, the measured elliptical motion in our study can be readily tuned in orbital radius, frequency, and ellipticity, and would persist even in the absence of thermal fluctuations.

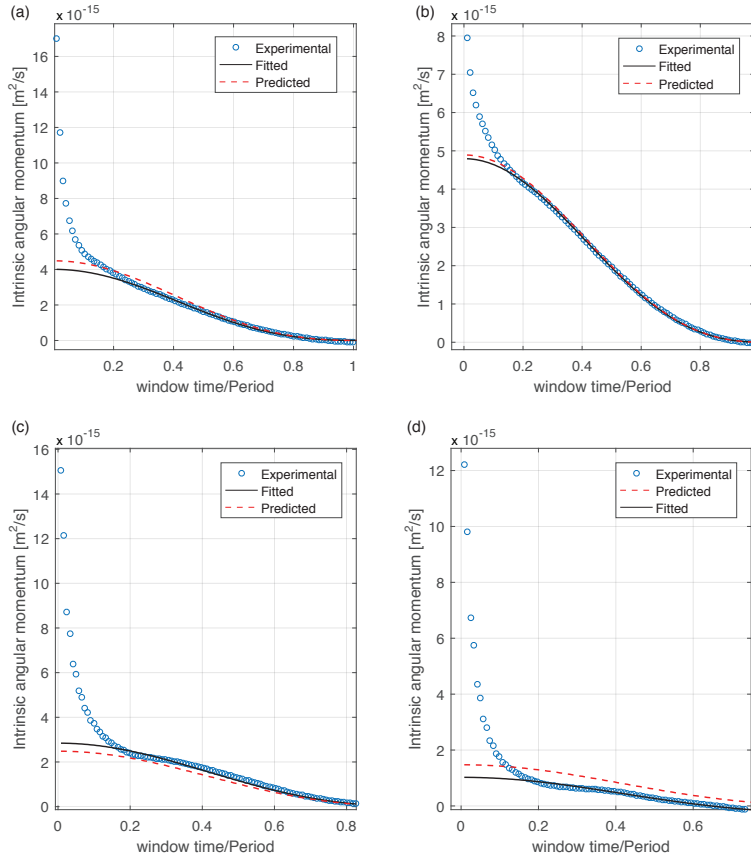


**Figure 7.4.8:** The angular momentum as a function of the windowing width of the velocity data. At small windowing widths, the angular momentum rapidly drops as the high frequent noise is filtered out. The angular momentum of the experimental data (blue circles) is extracted by fitting the curve in the region of large windowing widths to the analytical curve of a windowed noiseless ellipse (red curve) and by evaluating that fit at zero windowing width. The result is in excellent agreement with the value predicted from our analytical model (orange curve). (a) Frequency = 4.6 Hz, height = 170 nm. (b) Frequency = 4.6 Hz, height = 230 nm. (c) Frequency = 11 Hz, height = 160 nm. (d) Frequency = 11 Hz, height = 360 nm. The aforementioned results were obtained with particle having a radius equal to 1.1  $\mu$ m.

# 8

## Appendix

STARTING AUGUST 15 OF THIS YEAR, we began a re-build of the optical forces measurement set-up. The work was done together with Andrea Di Donato and Arman Amirzhan, who were both new to the project. Rebuilding step-by-step inspired me to begin documenting some basic alignment and troubleshooting procedures which I had begun to take for granted. The documentation has since evolved into a kind of practical guide to the optical force microscope. This section of my thesis is this guide, and is likely to be the most useful section for those continuing this work in my group or those interested in reproducing this work elsewhere.

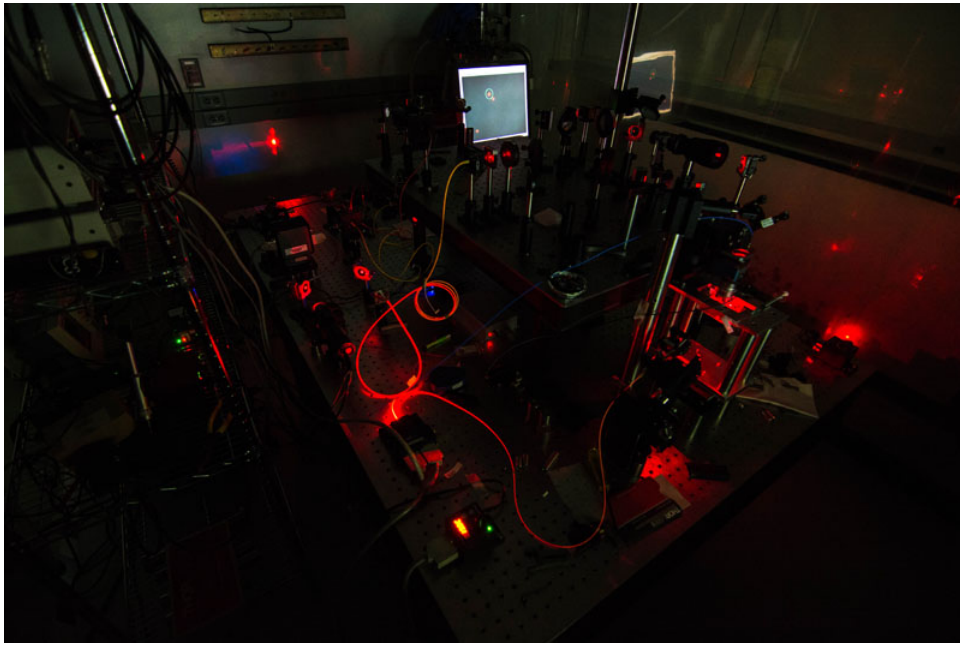


**Figure 8.0.1:** Photo showing the force microscope in operation. Photo credit: Arman Amirzhan

## 8.1 COMPONENTS

### 8.1.1 LIGHT SOURCES

As noted in previous chapters, the set-up is similar in its core to a classic total internal reflection microscopy (TIRM) set-up. Such a set-up requires optical access of the sample from both the top and bottom of the chamber. The laser beam (660 nm CW) incident from above must be focused by a high-NA water-immersion objective for single-beam optical tweezing. A white LED, focused through the same objective, provides dark-field lighting over the entire objective field of view (FOV).

The detection laser beam (637 nm CW) incident from below must be at an angle such that the light totally internally reflects at the glass-water interface of the chamber. For this purpose, a 60-degree glass prism is often used to couple light into the glass.

For measurements of optical forces from an evanescent field a second totally-internally reflecting beam (785 nm CW) is incident on the bottom of the sample chamber from the opposite direction. The total number of laser light sources on this set-up is therefore, currently, three. All are fiber-coupled for easy maneuvering and realignment.

#### 8.1.2 DETECTORS

Three detectors track the three dimensional displacement of the trapped microsphere. The motion of the particle perpendicular to the glass-water interface is tracked by a photodiode which monitors the intensity of the light it scatters from the totally internally reflecting detection beam, also called the probe beam.

Motion in the two lateral directions parallel to the surface is monitored by tracking the displacement of the reflected trap beam which has been back-scattered by the particle. In a method similar to a quadrant photodiode, for each axis, the reflected beam is divided spatially into two halves, and the difference between the intensities of these two signals is reported by a balanced detector and converted into displacement.

#### 8.1.3 THE OBJECTIVE ASSEMBLY

The current design of the objective assembly, seen in Figure 8.1.1 uses a piezo objective scanner from Piezosystems Jena designed for microscopy applications. This should afford us significantly more stable positioning and reduced vibrational noise compared to a Thorlabs flexure stage on which our objective was originally mounted.

The goal of this design is to allow macro-movements with the vertical translation stage and micro-positioning with the piezo scanner. The 4 mm travel of the translation stage enables loading, unloading, and manual objective focusing. The piezo scanner is a part of a closed loop involving a capacitive sensor

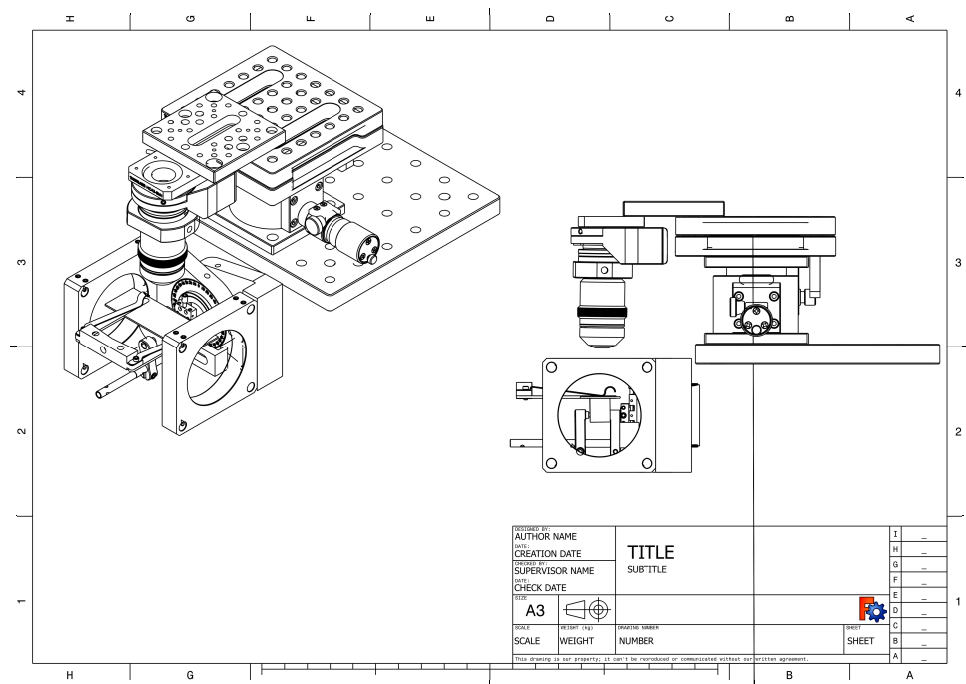


**Figure 8.1.1:** Current design of the objective and prism assembly. For a list of parts please see Table 8.1.1.

<b>Part</b>	<b>Description</b>	<b>Vendor</b>
Leica PL APO 63×/1.20 WCORR	Water-Immersion NA 1.2 Objective	Leica (belongs to Weitz Group)
MIPOS 100 PL O-323-00	Piezo Objective Scanner	Piezosystems Jena
TSD- 653DMUU	Micrometer vertical stage	Optosigma
KBM1	Switchable Magnetic Kinematic Breadboard	Thorlabs
SM1A11	Adapter with External M <sub>25</sub> Threads and Internal SM1 Threads	Thorlabs
SM1A12	Adapter with External SM1 Threads and Internal M <sub>25</sub> Threads	Thorlabs
SM1Lo5	SM1 Lens Tube	Thorlabs
SM1RC	Slip Ring for SM1 Lens Tubes 832 Tap	Thorlabs
HCA3-SM1	SM1 Adapter for Mounting Objective	Thorlabs
XT34HP	Dovetail Mount used as right-angle adapter	Thorlabs
9101NF	Right Angle Bracket	Newport

**Table 8.1.1:** Parts for current design of objective assembly mount.

(not pictured) to detect and correct for thermal expansion and drift of the objective focus.

For a full list of parts see Table 8.1.1.

## 8.2 SET-UP AND ALIGNMENT

### 8.2.1 TWO-LEVEL OPTICS BENCH

The set-up is built on two levels. Top level is reserved for beam paths to and from the back aperture of the objective, as shown in Figure 8.2.1, while the bottom level holds the sample stage, optics for accessing the sample back-side, and mounted utility optics such as fiber couplers and the LED. The top surface of the

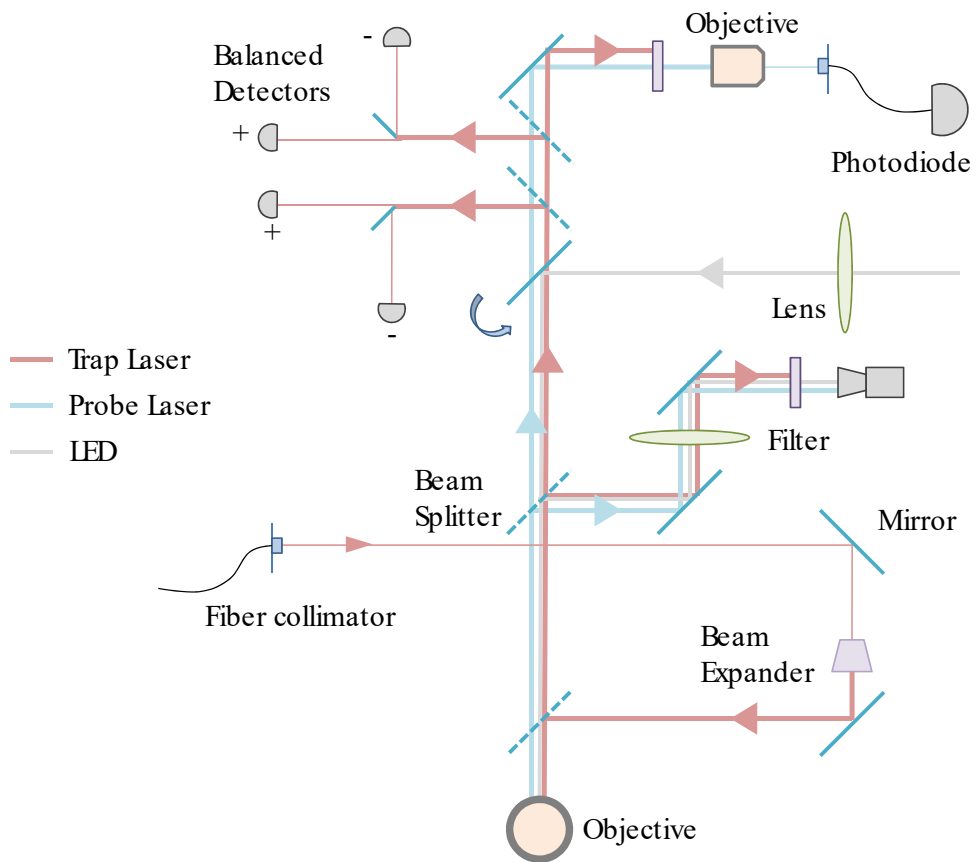


**Figure 8.2.1:** The current optical paths and equipment on the top level of our optical set-up.

raised breadboard is eleven inches above the optical table top. The optical table is itself floated on four actively-stabilized hydraulic legs for isolation from vibrations of the lab itself, which is on the ground floor of our building.

#### 8.2.2 45-DEGREE MIRROR

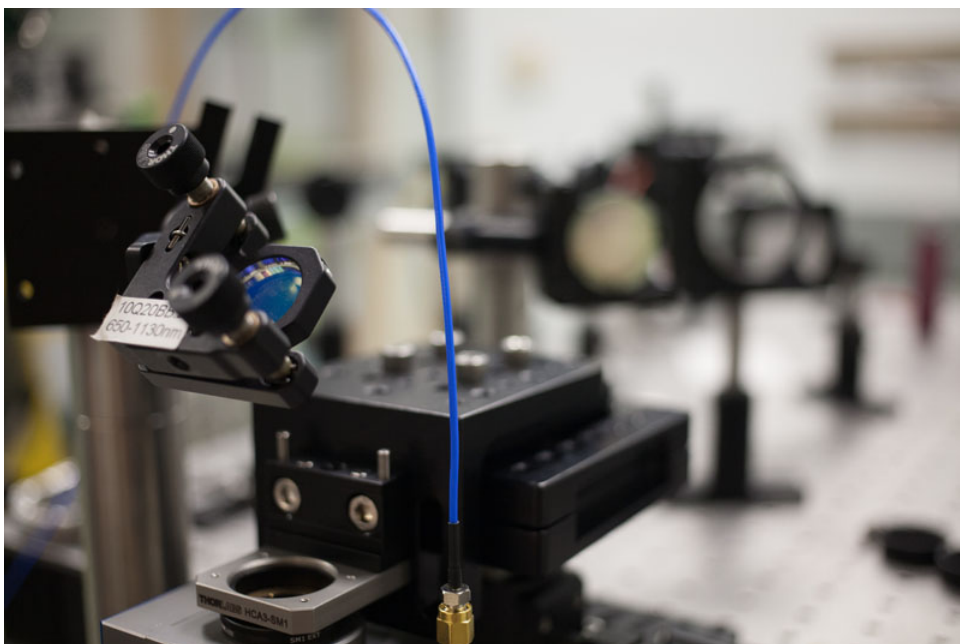


**Figure 8.2.2:** Photo showing the 45-degree mirror in our set-up above the back aperture of the objective.

Besides the objective, the most important piece of optics, which affects the alignment of the whole system, is the 45-degree mirror above the back aperture of the objective, which redirects the laterally traveling beams perpendicularly down into the objective and sample. An improperly aligned 45-degree mirror will introduce stigmation which will negatively affect particle trapping, tracking, and imaging.

To ensure that the mirror is centered properly above the objective and angled at 45 degrees, a temporary alignment beam is set up with the 637 nm

fiber-coupled laser and two mirrors. The two mirrors are used to send the laser light straight and flat down the bolt line centered on the objective, using irises as aids. The 45 degree mirror, to be aligned, is inserted into the beam line and put roughly in place in order to direct the beam down towards the objective. A mirror laid flat on the back aperture of the objective returns the laser light along the beam line.

The aim is then the following: to overlap the reflected and incident beams by adjusting only the position and tilt of the 45-degree mirror while ensuring that the laser spot is centered on both the 45-degree mirror and the objective aperture. If the objective is mounted squarely, that is, with its back focal plane parallel to the ground, this procedure ensures the proper centering and orientation of the 45-degree mirror.

All other beams will be roughly aligned to this temporary alignment reference beam.

### 8.2.3 IMAGING LED LIGHT

The mounted, collimated LED light is about 100 mW at full power. In the current configuration, the LED collimator is set to a distance which produces a beam with a divergence of about 20 degrees. A 2 inch diameter, 500 mm focal length lens (which must be placed out of the central beam path), focuses the LED light into a spot about 0.8 cm in diameter at the back aperture of the objective. The long focal length lens allows the white light to be joined onto the central beam line behind the other beams, therefore, causing the least power loss, and the least disturbance to the more important beam lines for trapping and imaging.

The distance between the LED and the 500 mm FL lens is around 130 cm, and the distance between that same lens and the objective is around 90 cm. The beam starts off on the lower level of the optical set-up and is sent to the upper level by a periscope and two 2 inch mirrors. Only approximately 5% of the total power of the LED reaches the back aperture of the objective in this scheme. Although this is more than enough power for our needs, a redesign—including, perhaps, a



**Figure 8.2.3:** Photo of the LED beam path on the lower level of our optical set-up.

different focal length choice for the LED collimator—may dramatically improve power efficiency.

A flip-mounted mirror ultimately joins the white LED light onto the central beam line. However, for initial alignment, it's recommended that a beam-splitter is used instead. A beam-splitter allows the alignment reference beam to be viewed juxtaposed with the white illumination light. Place and orient this beam-splitter such that the reference beam is centered on the white LED spot and they travel collinear to the back aperture of the objective. This ensures that the white light is also approximately aligned along the optical axis of the objective.

#### 8.2.4 IMAGING AND CAMERA

The objective is infinity-corrected for use with a tube lens of focal length 200 mm, and is coverslip corrected for a #1.5 glass coverslip with precisely 170  $\mu\text{m}$  thickness. To set-up the correct position of the camera and tube lens, first place

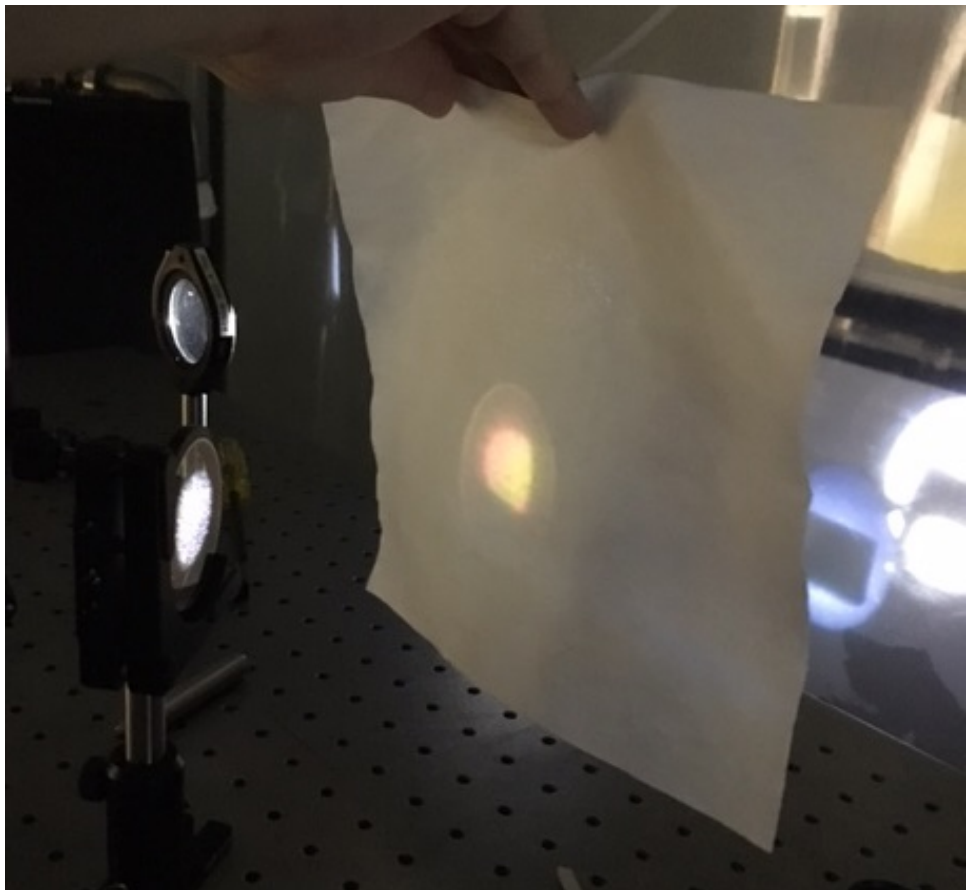


**Figure 8.2.4:** Finding the objective focus without an existing imaging mechanism is possible by monitoring the imaging light reflected from the sample surface. It should reach a maximum when focus is approached.

the 8% reflective pellicle beam-splitter in the central beam path according to Figure 8.2.1. This beam-splitter aims to pick off a portion of the light coming from the objective to send to the CCD camera.

Approach the water-immersion objective to the sample surface while monitoring carefully the LED light coming from the objective lens. The focal height of the objective is determined by the position where the back-reflected beam is brightest, see Figure 8.2.4. Direct this beam along the bolt lines to a 200 mm tube lens and CCD camera, placed at the lens focus. Verify that image looks sharp and clean, resembling Figure 8.2.5.

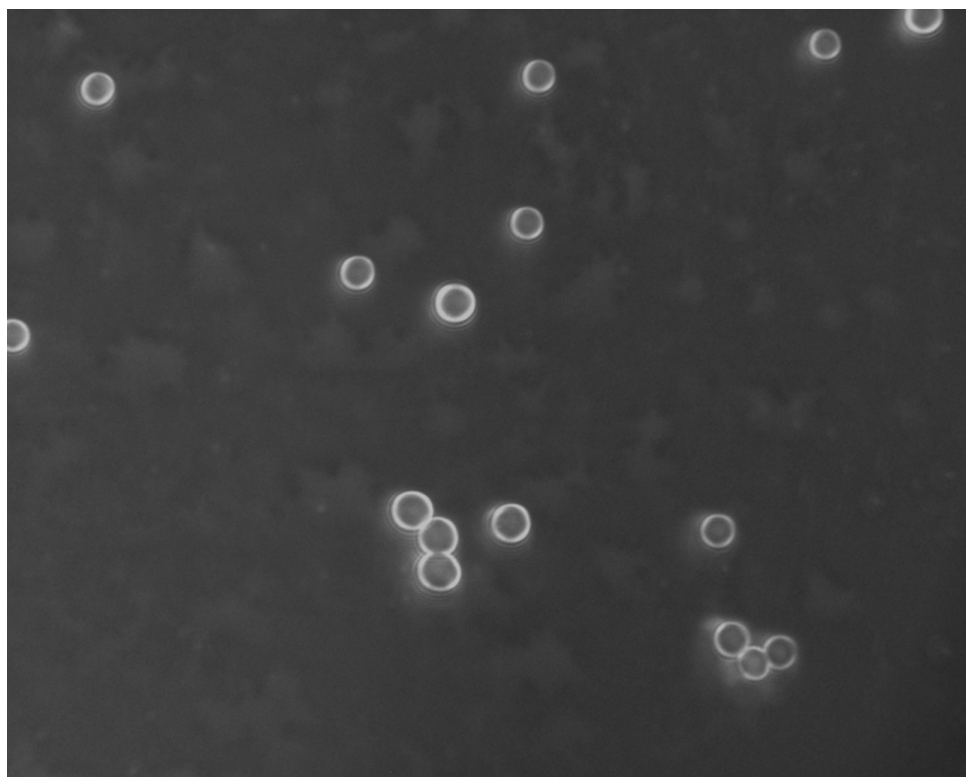


**Figure 8.2.5:** Dark-field image of polystyrene beads in water-filled chamber. Reference for proper focus and resolution.

### 8.2.5 CAPACITIVE SENSOR

The capacitive sensor is to be mounted onto the objective assembly. The sensitivity range of the capacitive sensor is between approximately 5 and 15 microns. The sensor should be mounted vertically to the part of the objective assembly which moves with the objective during focusing and scanning.

Currently, it is mounted directly to the objective adapter ring by a custom-tapped 8-32 threaded hole, as shown in Figure 8.2.6.

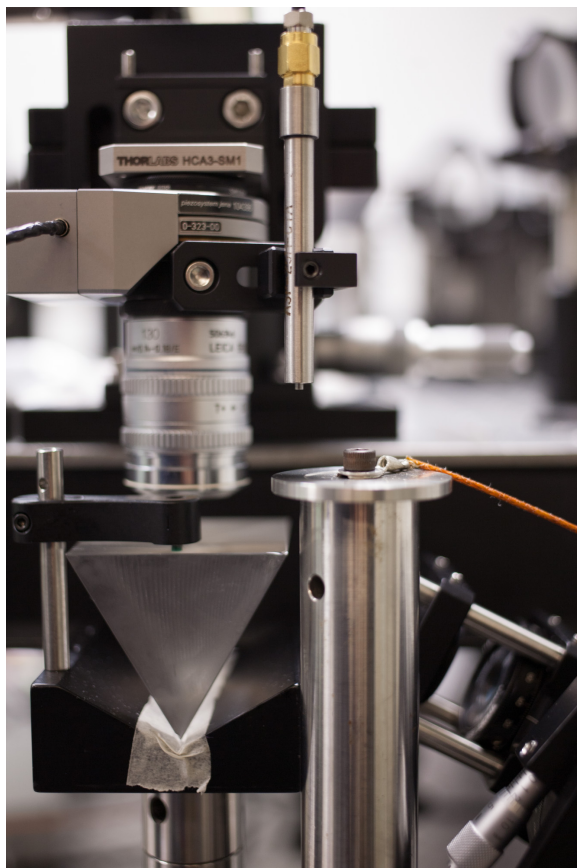


**Figure 8.2.6:** Photo showing capacitive sensor attachment to objective.

The purpose of the capacitive sensor is to act in a PID feedback loop along with the piezo scanner in order to correct for low frequency drift in the system.

Low frequency drift comes primarily from thermal expansion of the various metallic components in the objective assembly and stage. Focal spot drift on the order of magnitude of 200 nm is not uncommon in a ten minute measurement, even in a temperature controlled setting. After activating capacitive feedback circuit, the drift should be reduced to less than 10 nm.

A key consideration when mounting the sensor is the choice of attachment point to the objective assembly. Consider a small increase in temperature, corresponding to a small expansion of optical and mechanical components. Generally, the effect would be to bring the objective closer to the stage, or to shift downward the focal point. Ideally, the capacitive sensor will measure, and correct for, a change in separation representative of the true change in focal spot position. However, its position is unaffected by the thermal expansion of the objective itself, since the attachment point is bound to be higher than the objective.

To roughly compensate for the additional thermal expansion of the objective, the rod's own thermal expansion should be matched, to first order, with that of the objective. To do this, adjust the length of rod below the attachment point, and verify that the drift is correctly compensated over a long time measurement.

Capacitive sensor should be raised in its holder except during actual operation of the microscope. This prevents damage to the rod itself through scratching or collision with the stage surface. However, after loading the microspheres into the sample chamber and finding the focus at its bottom surface, the capacitive sensor must be dropped into position within its operating range. We typically use the micrometer knobs on the vertical translation stage. With the sample surface in focus we drop the objective by 5 microns. We then lower the probe so it gently touches the surface of the grounded stage, and restore the original height of the objective.

#### 8.2.6 OPTICAL TWEEZER

Fiber couple the 660 nm CW laser. If unfamiliar with fiber coupling, please reference Section 8.3 for a general procedure. Use the fiber collimator and the

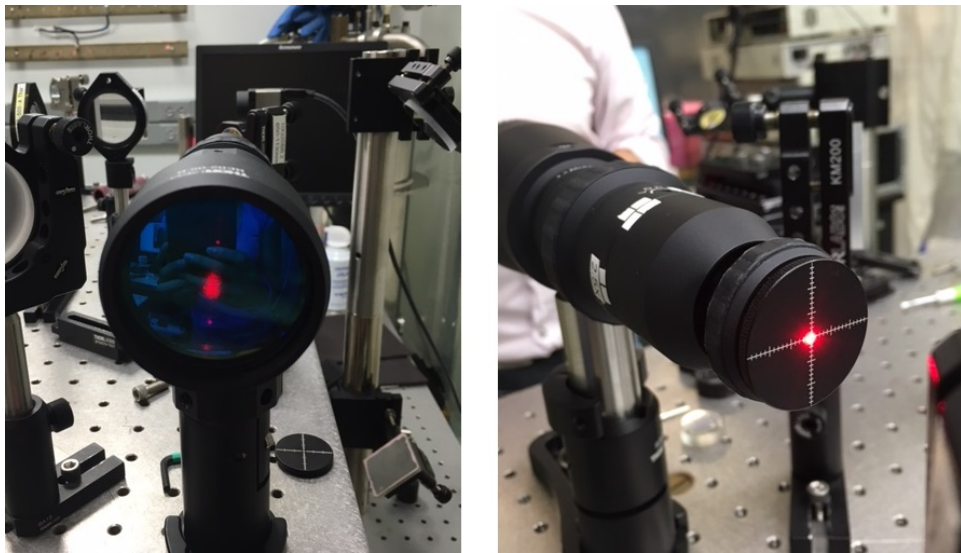


**Figure 8.2.7:** Ensuring that the trap beam goes through the optical axis of the beam expanding telescope minimizes stigmation.

2-5x adjustable beam expander to create a collimated spot with a full width half max (FWHM) of about 3 mm. A screw-on target may be used at the back aperture of the adjustable beam expander, and a set of two mirrors are necessary to direct the beam such that it is passing through the optical axis of the telescope. For a demonstration of proper alignment, see Figure 8.2.7.

The trap beam is joined onto the central beam path by a 50-50 pellicle beam splitter. The pellicle should be placed and oriented such that the trap beam is collinear with the imaging and reference beams.

At this point, with the imaging system in place, view the trap beam (at low power) under the microscope. The spot should be diffraction-limited, roughly centered in the camera field of view, and should spread out symmetrically when de-focused. If the beam is asymmetric, adjust one of the two mirrors after the beam expander.

If the beam is off-center in the camera FOV, "walk" the spot towards the desired location adjusting the two closest mirrors. First, adjust the back mirror slightly so that the spot moves in the direction opposite to what is desired. The

beam should start to look asymmetric. Then, use the closest mirror, which is, in our case, the 50-50 beam splitter, to restore the symmetry of the beam. Repeat as needed for the two dimensions. When the spot is in the required position, use a semi-transparent lens tissue at the objective back aperture to check that the beam is centered. Also, if necessary, at this point, re-align the imaging beam to the optimized trap beam. This ensures that the LED light is also aligned to the optical axis of the objective.

Place a notch filter on a flip-mount in front of the CCD camera which blocks the wavelength of light associated with the optical trap. Ensure that the single beam optical tweezer is functional by introducing glass beads into the sample chamber.

#### 8.2.7 THE TOTALLY INTERNALLY REFLECTING PROBE BEAM

The probe beam, pictured in Figure 8.2.1, is a fiber-coupled 637 nm laser. It needs to have access to the bottom-side of the sample chamber to totally internally reflect from the glass-water interface. The evanescent field created, at the position of the trapped bead, offers a highly sensitive detection of particle motion perpendicular to the surface.

The probe beam, after exiting the fiber, is focused by an adjustable collimator to a spot of around 300 $\mu\text{m}$  in diameter. It must pass through a half-wave plate, followed by an ND filter, before reaching the surface of the prism. The half-wave plate controls the angle of linear polarization. The ND filter prevents saturation of our photodiode. To hold all optics in place, a 30mm cage system is used. It is mounted on a rotation platform for angle adjustments and two translation stages for lateral and vertical adjustments.

To align the probe beam, begin by finding horizontal. Use an iris set at a fixed height or a ruler to ensure the beam is traveling parallel to the table. Mark the spot on the rotation stage as 0°. Then, rotate to 30° to horizontal, the beam should now be perpendicular to the surface of the prism. Align probe beam assembly such that beam spot overlaps its own reflection from the prism. The

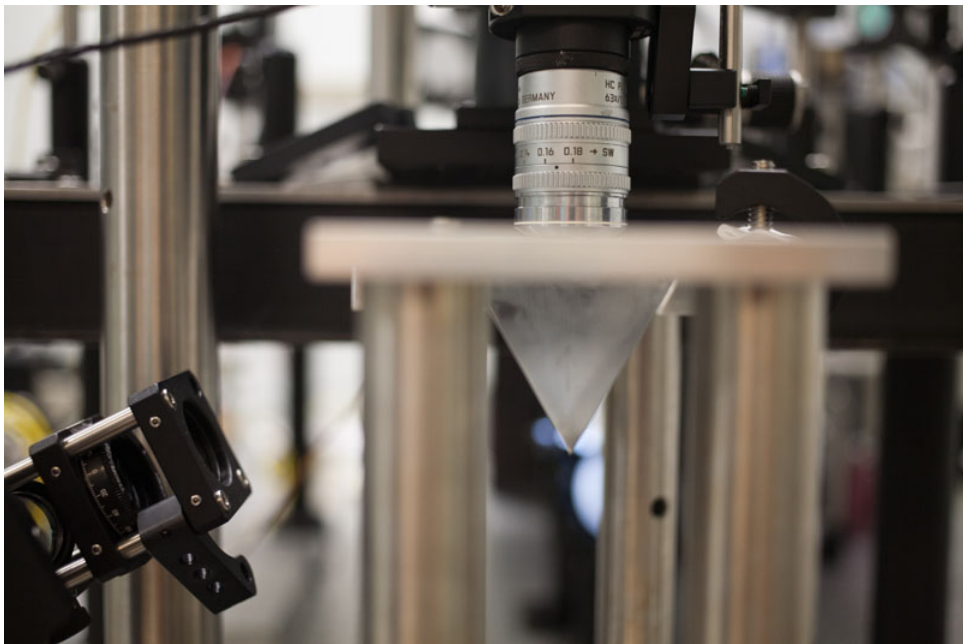


**Figure 8.2.8:** Probe beam entering the prism on the backside of the sample chamber.

ensures the beam is entering the prism at normal incidence.

Fill a sample chamber with water and polystyrene beads and place on the prism, careful to use enough index-matching fluid to optically join the two glass surfaces. Lower the water-immersion objective until the sample is in focus. Under white light illumination, looking from below through the prism, you should be able to see a white spot where the LED light is focused onto the sample surface. This is the spot where you will aim to align the probe beam. Without adjusting angle, using only the translation stage in the two dimensions, move the probe beam until a spot is visible in the chamber from light scattered at the glass-water interface. You will often see two dimmer spots on either side of this brighter spot, from scattering at the imperfectly index-matched fluid at the sample-prism interface.

When alignment is achieved, polystyrene particles in the field of view of the objective should begin to glow red in the microscope image. However, the probe

light is most likely not totally internally reflecting. To check for total internal reflection, trap a bead and begin to raise it using the optical tweezer, lifting it with the translation stage away from the surface. If the scattered probe light diminishes quickly to zero within a few microns of travel, the bead is scattering light from an evanescent field. Otherwise, the bead is scattering light propagating in the watery chamber.

If an evanescent field is not produced, "walk" the probe beam towards the critical angle. Alternately move the rotation stage and the vertical translator to keep the spot in the field of view at all times. Repeatedly check for total internal reflection using the method above.

#### 8.2.8 CONFOCAL DETECTION SET-UP

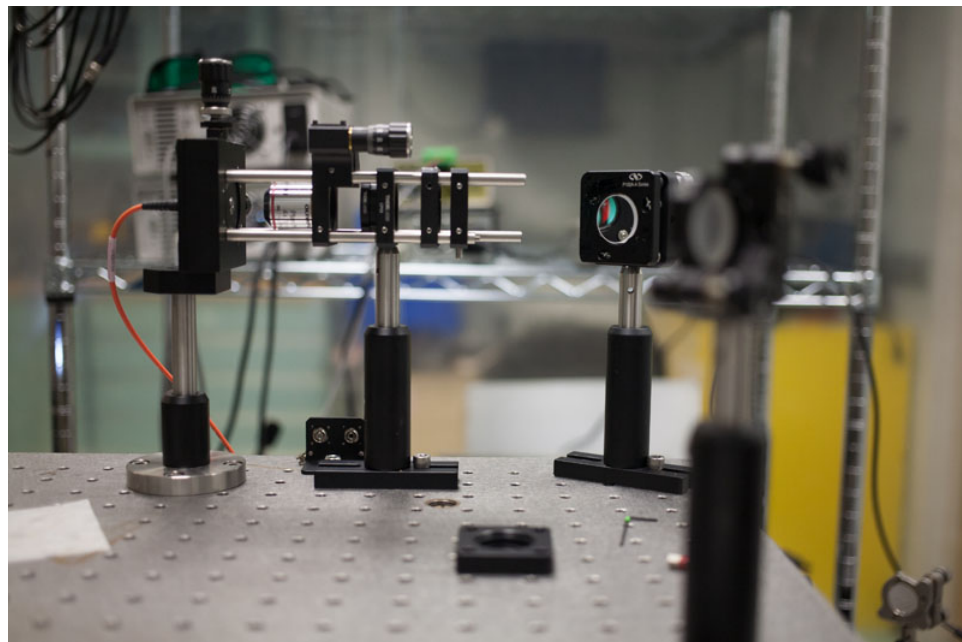


**Figure 8.2.9:** Photo showing the confocal collection scheme. A 4x objective is used to focus bandpass-filtered light from the sample onto a  $60\ \mu\text{m}$  diameter optical fiber. The output of this fiber is read by a photo-receiver.

With the scattered probe light visible in the camera, it's time to set up the

photo-receiver which will collect this light. We chose a confocal collection scheme, or, an apertured collection scheme, to cut down on background noise by limiting the collection area on the sample surface to a diameter of around  $4 \mu\text{m}$ .

The most straight-forward way of aligning the confocal sensitivity region, is, as usual, by sending light backwards through this system. The 637 nm probe laser is end-to-end coupled into the output of the multi-mode collection fiber. This light, representing the collection path of the confocal, needs to be aligned to the objective optical axis. The trap light, already aligned and reflecting from a mirror placed in the back focal plane of the objective, can be used as an alignment reference.

When rough alignment is achieved, the light from the multi-mode fiber should form an image on the sample surface. The image should be a speckled circle about  $4 \mu\text{m}$  in diameter. Slightly defocus the objective and observe how the circle expands. If it expands asymmetrically, move the two confocal mirrors to remove the stigmatism. Now, using the method discussed in Section 8.2.6, walk the collection area toward the optical trap until the two overlap, keeping the stigmatism minimal.

Remove the in-coupling probe laser fiber from the end of the multi-mode fiber, attach the multi-mode fiber to the photoreceiver, and replace the probe beam in its assembly. There should now be signal in the photo-receiver. Because a multi-mode fiber is used for light collection, there should be a region where sensitivity is flat. Move the two confocal mirrors to "center" the signal in this collection area.

Optically tweeze a particle and collect the power spectrum of its motion in the vertical direction. Confirm that the spectrum exhibits the typical Lorentzian shape associated with Brownian motion in an optical trap.

#### 8.2.9 PUMP BEAM SET-UP AND ALIGNMENT

A similar procedure may be used to align the pump beam. The hardware for the pump and probe beams would be symmetric but for one key difference: the

pump beam is focused by an aspheric lens, and it's important to begin by finding the focal distance.

Since the pump beam is ultimately a 785 nm wavelength beam, which is only barely visible to the human eye, for the sake of safety and sanity, most of the alignment should be done with the 637 nm fiber-coupled beam fed through the pump beam optics.

The pump beam optics, pictured in Figure 8.2.10, also mounted on the rails of a 30 mm cage, are in order: an FC/PC fiber collimator, a 95% transmissive beam splitter, a half-wave plate on a rotation mount, and a lens with focal length of 25 mm.

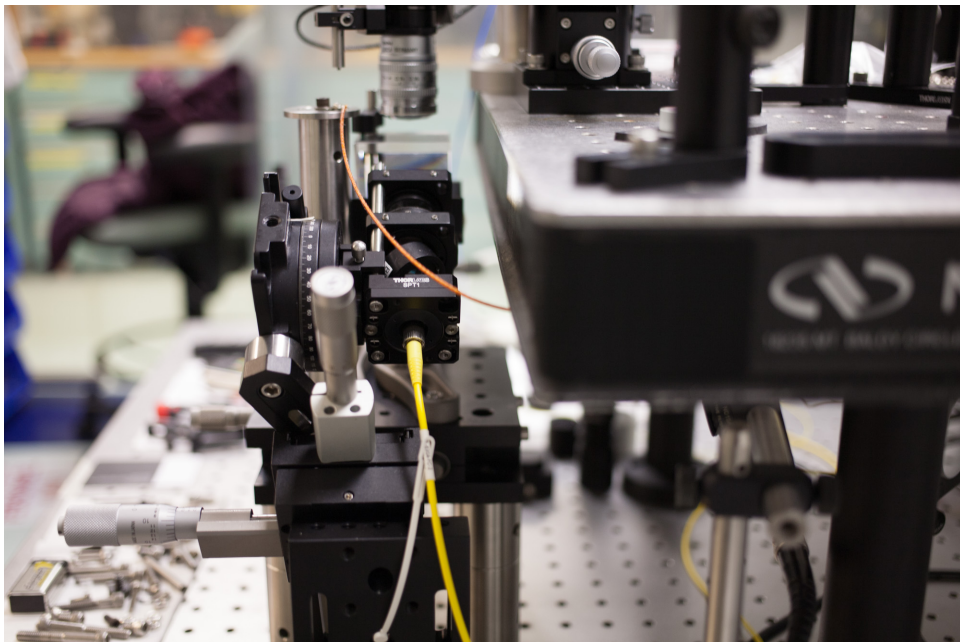


**Figure 8.2.10:** Photo of pump beam optics entering from the right side of the  $60^\circ$  prism.

First, use a black card to determine the rough focal position of the beam once it has passed through all the optics. Place the pump beam hardware at the appropriate distance from the prism such that the focus will be formed at the point of total internal reflection, i.e. at the bottom surface of the water-filled

chamber. If a finer adjustment is needed, check Section 8.5 for instructions.

Perform the alignment procedure described in Section 8.2.7 with the 637 nm laser. Once alignment has been achieved, introduce the 785 nm beam. Slight misalignment is to be expected on changing wavelength. Realign by adjusting the translation stage only.

#### 8.2.10 THE PUMP MONITOR PHOTODIODE

The pump monitor photoreceiver collects the reference signal for our lock-in detection. It is on an independent stand and connected via a BNC cable to the fourth channel of the analog-to-digital converter. It should be positioned such that the diverted light from the beamsplitter is able to squarely illuminate the photodiode. Confirm that a square wave is recorded with the chopper turned on with amplitude of at least 1V.

#### 8.2.11 BALANCED DETECTION SET-UP

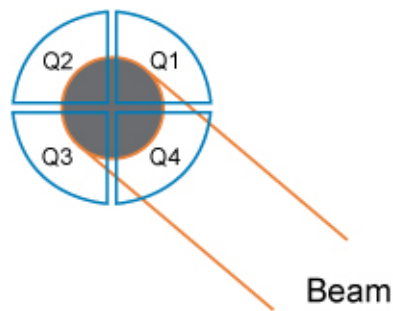


**Figure 8.2.11:** Schematic of a quadrant photodiode (QPD). Image from Thor-labs.com.

Lateral position tracking relies on measuring the deflection of the back-scattered trap beam when a particle is present. Often, a quadrant photodiode (QPD), pictured in Figure 8.2.11 is used for 2-dimensional detection. In our case, we use two balanced detectors sensitive to motion in the two orthogonal directions parallel to the sample surface.

A portion of the back-scattered beam, picked off by a 50-50 beam-splitter, is divided first laterally in half using a D-shaped mirror. Each half of the beam sent to one of the two photodiodes of a balanced detector. The difference between these two signals is recorded in volts, related to the particle's lateral displacement in nanometers by a proportionality constant,  $C_o$ . The remainder of the beam is then divided vertically in half for measurement in the other lateral direction.

A properly aligned balanced detection system should report a mean voltage, or mean displacement, of zero when the D-shaped mirror is symmetrically dividing the back-scattered beam.

The alignment procedure starts at the identification of the back-scattered beam from the trapped bead. See Figure 8.2.12.

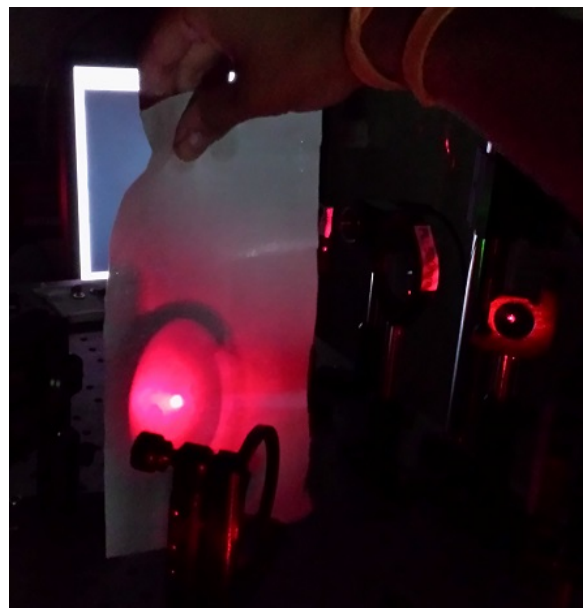


**Figure 8.2.12:** Back-scattered trap beam from a trapped polystyrene microsphere. It's recommended to align the balanced detector with PS microspheres. Their higher index contrast results in more reflected, or back-scattered, light.

Use a 50-50 beam splitter to pick off a portion of the back-scattered light ahead of the confocal detection. Use the position of the bolt holes to ensure the beam is scattering at 45 degrees from the beam splitter.

Place the D-shaped mirror so that the full beam is entirely reflected. Direct this beam to one of the input photodiodes of the balanced detector using a half-inch mirror. Turn down the gain on the balanced detector and observe on the oscilloscope the intensity readout of the full beam. Move the mirrors until the signal is maximized. There is a range of acceptable angles since the sensor area will be large compared to the beam spot.

Translate the D-shaped mirror on the mini translation stage until it is entirely out of the beam path. Use the remaining two half-inch mirrors to direct this beam towards the second input photodiode of the balanced detector. Maximize the intensity reading in the same way, this time, looking for a maximum signal that is equal to the negative of the first photodiode signal during the previous step.



**Figure 8.2.13:** Photo of balanced detector and optics.

If the alignment is correct, you should be able to move the D-shaped mirror until it reflects only half the beam. Increase the gain to maximum on the balanced detector and look for a signal with a mean of zero. If the signal is occasionally

saturating the balanced detector at either +10V or -10V, place the necessary neutral density filters in order to obtain a peak-to-peak signal of no more than  $\pm 3\text{V}$ .

Note: the balanced detector signal is highly sensitive to environmental noise! Be careful when choosing optical components to optimize for low mechanical vibrations!

### 8.3 FIBER COUPLING

All free space lasers are fiber coupled on our set-up. Fiber coupled lasers can easily be moved and swapped, facilitating alignment and troubleshooting. In choosing a fiber-lens pair for single-mode coupling, one aims to match the focused beam spot diameter and the mode field diameter of the fiber. The appropriate optics have already been chosen on this set-up. 50% coupling should be achievable.

Fiber coupling can be thought of as a three-step process, most efficiently performed with two lasers of similar wavelength: the free-space laser you wish to couple, and an already fiber coupled laser. Use two low-drift mirrors on kinematic mounts, for control over all four degrees of freedom of the beam.

#### 8.3.1 PROCEDURE

1. Set up laser, mirrors and fiber coupler so that the beam travels roughly on bolt lines and is reflected at 45 degrees.
2. Attach the fiber coupled alignment laser to the fiber port of the fiber coupler, so that a guidance beam comes out of the fiber and travels in reverse along the intended beam path. Turn on the free space laser and overlap the two beams at all points along the beam path. One reliable scheme for achieving this uses two semi-transparent lens tissues. Place a lens tissue between each laser source and the mirror nearest to it, such as in Figure 8.3.1. Both beams should be visible on each tissue. Start with one

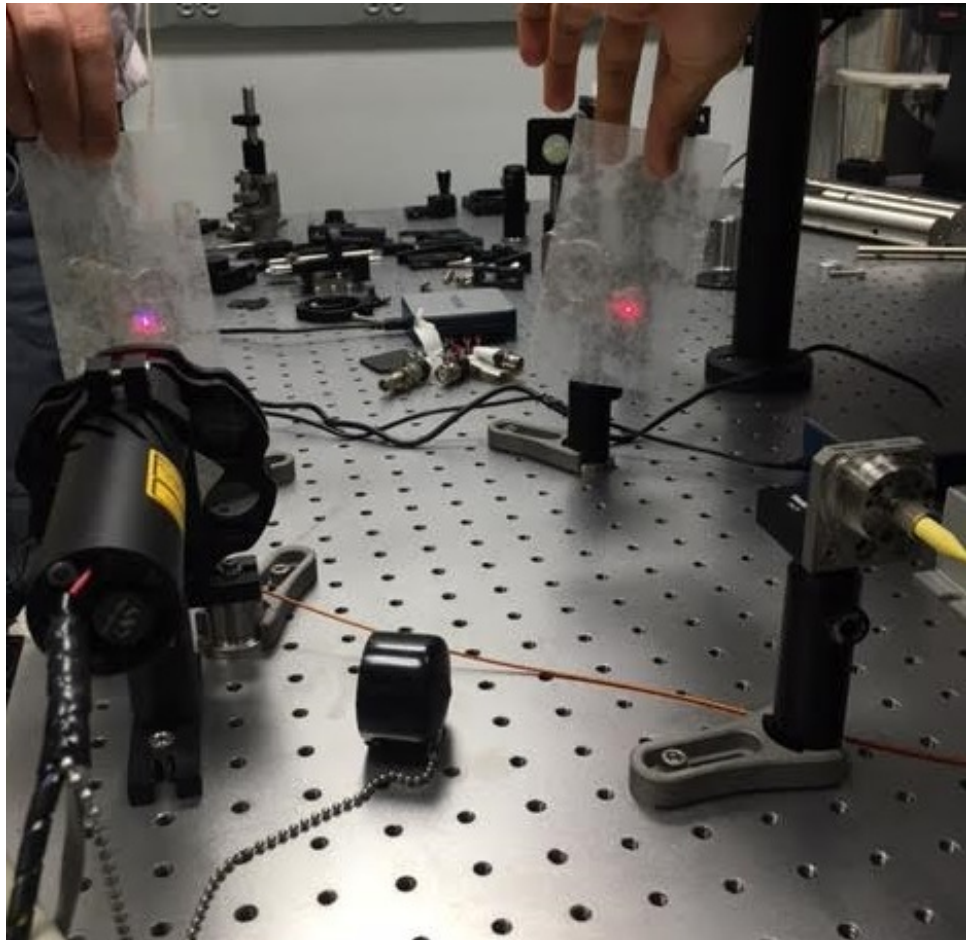


**Figure 8.3.1:** Roughly aligning the output of the guidance beam and the free space laser is essential to start the fiber coupling process. Use two semi-transparent lens tissues to align the spots at two points in the beam path. For each tissue, align the spots using only the farthest mirror.

tissue, use the mirror farthest from the tissue to overlap the two laser spots. Repeat with the other. Iterate, alternating between the two tissues and the beams should converge.

3. Once rough alignment is established, there should be some light coming out of the fiber coupler from the free-space beam. Remove fiber-coupled laser and attach a new optical fiber (FC/PC connector). Connect the free end of fiber to an optical power meter with an FC/PC adapter. Turn on free space laser, and record the power measured. Walk the beam using the two mirrors until the power is maximized:
  - Adjust each of the four degrees of freedom of the mirrors individually, maximizing the power by moving one at a time.
  - Adjust the two lateral degrees of freedom on the two mirrors simultaneously. Similar to fixing stigmation, move the first mirror in some direction until the power is about  $1/3$  of maximum, and restore the beam's alignment with the second mirror to find the new maximum power. If the new maximum is higher than the previous, continue walking beam in the same direction. If not, change directions. Repeat with vertical dimension.
4. Adjust the internal degrees of freedom of the fiber coupler. The objective here is to place the tip of the fiber exactly at the focal length of the collimating lens. In the case of the compact fiberport fiber coupler from Thorlabs, this is achieved by alternately adjusting 5 screws in the back of the coupler. In the objective coupler, the longitudinal degree of freedom is separated from the others, and should be the only one to be adjusted.

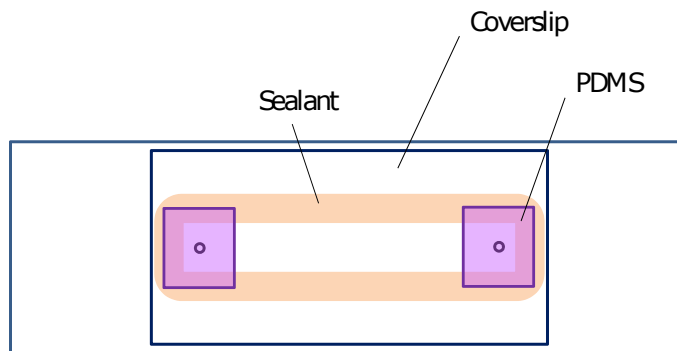


**Figure 8.4.1:** Fully constructed microfluidic sample chamber.

Part	Description	Vendor
BK7 Glass Slide	75mm x 25mm x 1mm	VWR
Glass Coverslips 1.5H	60mm x 24mm x 0.17mm	Schott Nexterion
Meltonix Sealant	25 um thick	Solaronix
BD-309628	1 mL Syringe w/ Luer-Lok Tip	BD / VWR
Z192481-100EA	BD PrecisionGlide Needle 21 gauge	Sigma-Aldrich
EW-06406-60	FEP Tubing 1/16in OD	Cole Parmer
PDMS	Polydimethylsiloxane	Soft Materials Clean Room

**Table 8.4.1:** Parts for microfluidic sample chamber.

## 8.4 MICROFLUIDIC SAMPLE CHAMBERS

### 8.4.1 PROCEDURE



**Figure 8.4.2:** Coverslip with laser drilled holes.

1. Deposit AR coating on BK7 slides. Use the NEXX PECVD tool in CNS clean room. The target index is 1.445, target thickness, for 660 nm AR in water, is 112 nm. According to the current process on the tool, the deposition time should be 10 minutes and 40 seconds, corresponding to a rate of 10.5 nm/min.
2. Drill Holes in 1.5H Coverslips. Use the VersaLaser in Go6 and the template saved under LuluLiu\_Coverslip. The settings should be, after focusing the laser, 31.5% power, 48% speed, 165 PPI, 1mm Z axis, and the cut should be performed four times for each hole.
3. Cut Solaronix Sealant into shape, using a razor. The sealant should not exceed 60 mm in length or 24 mm in width.

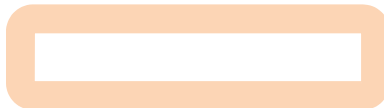


**Figure 8.4.3:** Sealant cut into shape.

4. In a hot press, or oven, gently press the sealant between coverslip and slide. Careful not to crack the coverslip. Align holes on inside of channel. Heat

should be applied for 20 minutes minimum at 110°C in the hot press. In the oven, the chamber needs to remain for a minimum of two hours for a seal to be fully formed.

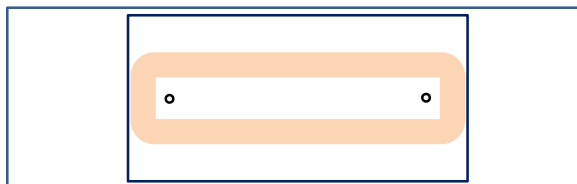


**Figure 8.4.4:** Assembled chamber.

5. Attach PDMS to inlet and outlet. First, punch 1.5 mm holes in PDMS cubes of 1 cm by 1 cm. Sonicate assembled chamber and PDMS blocks in isopropyl alcohol for 10 minutes. Dry afterwards in 60°C oven for 3 hours to ensure alcohol is completely evaporated. Bond PDMS to coverslip using plasma oxidizer in soft materials clean room (SMCR). The power is 25 Watts and the exposure time should be 10 seconds. Read tool manual for potential bonding procedure updates.

## 8.5 PUMP BEAM FOCUSING

Due to the low power of our pump laser—around 100 mW after coupling to fiber—the beam must be focused so that the intensity is large enough at the surface to result in optical forces in the femtonewtons.

The pump beam is collimated by an adjustable fiber collimator and then focused by an aspheric lens. Due to slant incidence, the beam spot is an ellipse on the bottom surface of the chamber. The spot size may be adjusted by translating the aspheric lens or translating or re-focusing the fiber collimator or all of the above.

The 60x objective is not appropriate for this work. A field of view larger than the beam spot size is required. There is a 10x objective which should be used in

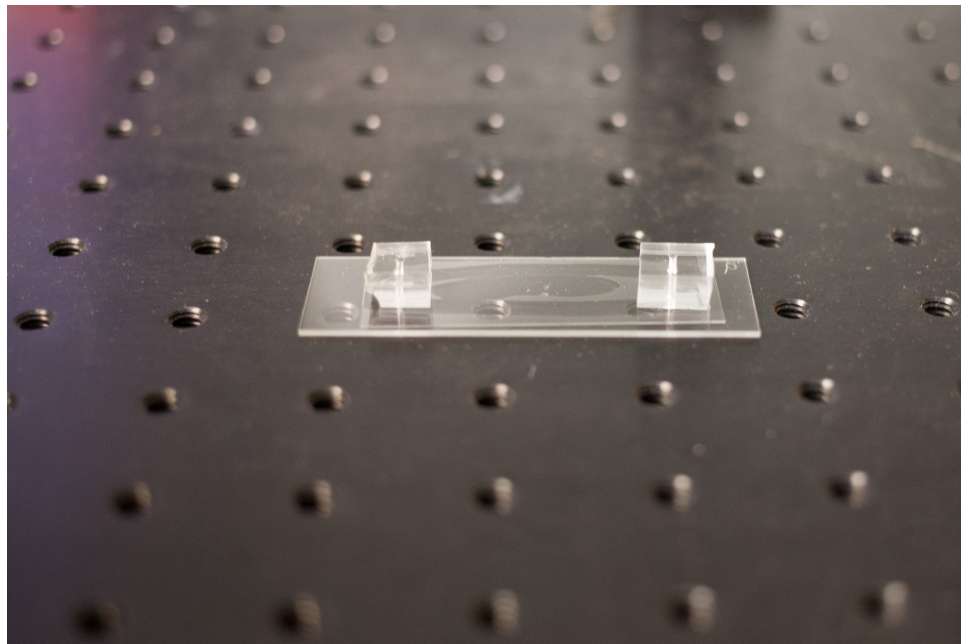


**Figure 8.4.5:** Photo of assembled microfluidic chamber.

place of the 6ox. Because the objective working distance and length and threading is different, it is encouraged that the second objective sit on its own removable Thorlabs magnetic platform, with its own hardware, so that alignment needs to be done only one time.

Once the 10x objective is in place, place a frosted glass slide with index-matching oil on the prism surface. The roughness on the surface of the slide, which is what makes it appear white or frosted, will scatter light from the totally internally reflecting beam. The intensity of the light scattered is related to the intensity of the evanescent field at that position.

Perform the adjustments until the spot is minimal in size.

For a quantitative measurement of the spot size and therefore field intensity, take a photo of the illuminated spot, e.g. Figure 8.5.1. Calibrate the distances in the camera image with a calibration slide and measure a cross-section in an image processing program for values of pixel brightness and fit to a Gaussian profile.

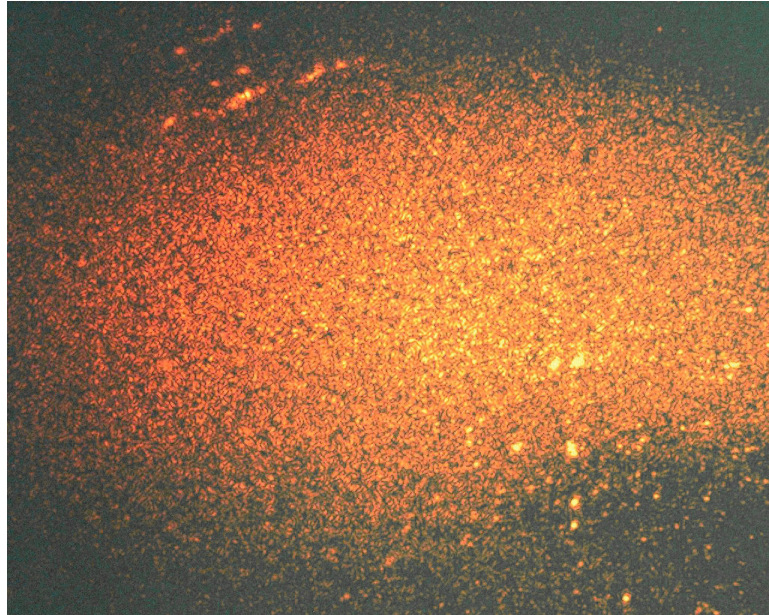


**Figure 8.5.1:** The imaged spot of the 785 nm totally internally reflecting pump beam scattering from a frosted glass slide.

## 8.6 PHASE CALIBRATION

The frequency-dependent response of the particle  $\tilde{x}(\omega)$  has real and imaginary components which are predicted by the particle's response function. The phase lag between the periodically varying force and response is an important quantity which not only determines the physical trajectory of the driven microsphere, but can act as confirmation that the measured signal is indeed the predicted translation of the particle's center of mass.

In order to measure precisely the phase of the particle's response, the delays in each measured signal – from circuitry in the photodiodes to signal propagation in transmission lines of different lengths – must be accounted for. We choose to measure these phase delays by sending a simultaneous optical signal to all detectors.

For this purpose we use the 785 nm wavelength pump beam in the normal data-taking configuration. A trapped bead is not necessary for this measurement.

Instead, I prefer to use a frosted slide in order to scatter light from the totally internally reflecting beam. Removing the notch and bandpass filters placed in front of each detector, the light should appear in all data channels. Apply the appropriate neutral density filters to avoid saturating the detectors.

By chopping this light at a moderate frequency, the modulated signal may be compared in phase between each position channel (one in each spatial dimension) and the pump reference channel. Make certain other lasers are not on during this process, and take at least 100 cycles of on-off data at five different frequencies between 1 and 200 Hz. When the phase delay between each channel and the reference channel is plotted against frequency, the result should be linear and increasing with frequency. The linear regression represents a constant time delay between the signals of the two channels. The fitted phase delay as a function of frequency will be used in data post-processing to correct the measured signal so that it is simultaneous with the reference signal.

## 8.7 LABVIEW CONTROL SOFTWARE

Figure 8.7.1 shows the front panel of the custom Labview control software as it was redesigned by Simon Kheifets updated by Andrea Didonato. Some functionalities are out of date. The interface could use some clean up at this point.

The three panels on the left column show three views of live data. Drop-down menus allow for toggle between different DAQ channels for display. The top panel shows live updating raw data for selected channels. Middle panel shows raw data for all channels simultaneously with a zoomed-out time axis. Bottom panel shows a live updating power spectrum for a selected channel, defined as the magnitude square of the Fourier transform of the signal.

The middle column contains the controls for acquiring data (top), and the readouts of the piezo and x-y stage (middle and bottom). The x-y stage controls are defunct, as it was replaced by a manual stage in 2015. Each new data set can be acquired, i.e. recorded to computer hard drive, by setting a limit for the

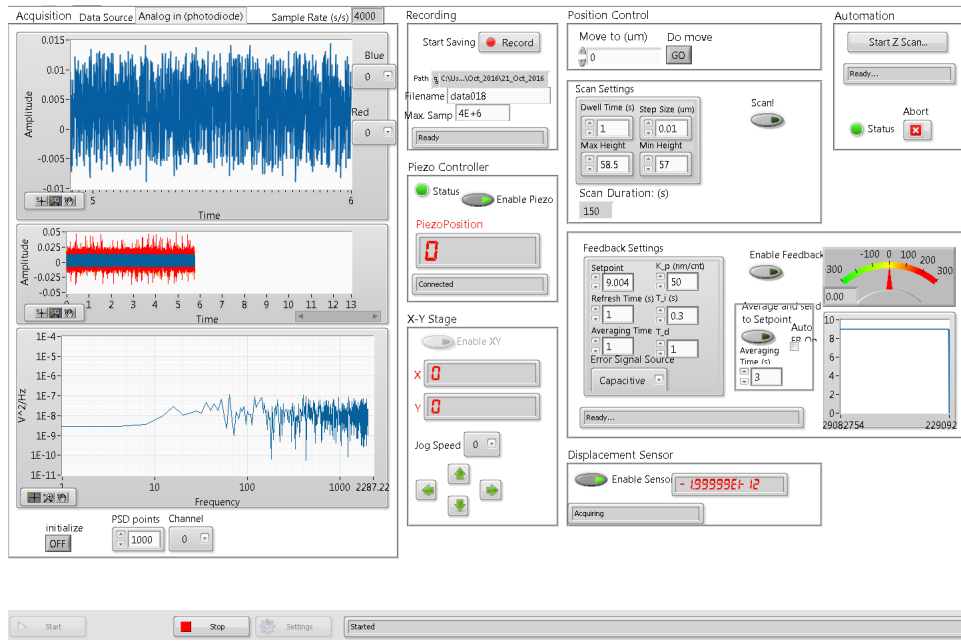


**Figure 8.7.1:** Front panel of our custom Labview control software.

number of samples, and then hitting *record*. The file path and file name are automatically filled in. The former with the date and the latter with an incrementally increasing data number. Data recording ends when the stop button is pressed or when maximum samples has been reached.

The far right column holds the *Position Control*, *Scan*, *Capacitive Feedback*, and *Automation* capabilities. Position Control originally moved the old objective piezo and has been defunct since about 2015. Instead, since the implementation of the capacitive feedback loop, piezo height is set using the *setpoint* of the capacitive feedback loop.

The *Scan Settings* panel is used to perform a vertical calibration scan of the trapped particle. Ensure that the feedback is disabled for this scan and that the pump beam is switched off. The purpose of the calibration is to find the relationship between height of the particle and the intensity of the light it scatters from the probe beam. The result can be analyzed using the Matlab script *PlotCalibration3*. The particle should first be lifted from the surface until no

scattered probe light appears on the camera. Then step size should be set along with time between steps. The current reading from the piezo controller should be input into the field *Max Height*. *Min Height* should be set to be at least 1.5 or 2  $\mu\text{m}$  lower. When the scan is initiated, the software begins to collect data on the intensity of the scattered probe light. Simultaneously, it records the position of the capacitive sensor. These two vectors will be used together to determine the height-intensity relationship.

The *Feedback Settings* contains the parameters of the PID control loop. It is best not to adjust these parameters unless the system is changed dramatically. *Average and send to Setpoint* measures current height from the capacitive sensor and sets this value as the target for the feedback loop. It's recommended to always use this feature before enabling feedback to prevent accidentally large movements of the piezo stage.

Finally, the *Automation* panel is used for obtaining force "spectra", or force as a function of height curves for a given probe. A dialog box opens when *Start Z Scan* button is pressed. The nature of the procedure is similar to the calibration scan. However, in this case, a separate data set is obtained for each height, and the steps are taken by incrementing not the piezo voltage directly, but rather changing the feedback loop setpoint. Once the new setpoint has been reached, the next data set will begin recording automatically. The pump beam should be left on for the duration of the scan.

## References

- [1] Sensitive force technique to probe molecular adhesion and structural linkages at biological interfaces. *Biophysical journal*, 68:2580–7, 1995. ISSN 0006-3495. URL  
<http://www.ncbi.nlm.nih.gov/pmc/articles/PMC1382168/>?tool=pmcentrez&rendertype=abstract.
- [2] Analysis of radiation pressure exerted on a metallic particle within an evanescent field. *Optics Letters*, 25(18):1385–1387, 2000. ISSN 0146-9592. doi: 10.1364/OL.25.001385.
- [3] An optically driven pump for microfluidics. *Lab on a chip*, 6(6):735–739, 2006. ISSN 1473-0197. URL  
[http://pubs.rsc.org/en/content/articlelanding/2006/lc/b6o1886f\\$& delimiter=o26E3oF\\$nhttp://pubs.rsc.org/en/content/articlelanding/2006/lc/b6o1886f{#}!divAbstract](http://pubs.rsc.org/en/content/articlelanding/2006/lc/b6o1886f$& delimiter=o26E3oF$nhttp://pubs.rsc.org/en/content/articlelanding/2006/lc/b6o1886f{#}!divAbstract).
- [4] Propulsion of gold nanoparticles with surface plasmon polaritons: Evidence of enhanced optical force from near-field coupling between gold particle and gold film. *Nano Letters*, 9:2623–2629, 2009. ISSN 15306984. doi: 10.1021/nl900944y.
- [5] Force generation by the growth of amyloid aggregates. *Proceedings of the National Academy of Sciences*, 112:1417326112, 2015. ISSN 1091-6490. doi: 10.1073/pnas.1417326112. URL  
<http://www.pnas.org/content/early/2015/07/16/1417326112.abstract?sid=5c24a61b-5bba-45a7-bca1-30102a5175dd>.
- [6] E Almaas and I Brevik. Radiation forces on a micrometer-sized sphere in an evanescent field. *Journal of the Optical Society of America B*, 12:2429–2438, 1995.

- [7] Arthur Ashkin. Forces of a single-beam gradient laser trap on a dielectric sphere in the ray optics regime. *Biophysical journal*, 61(2):569–582, 1992.
- [8] Arthur Ashkin, JM Dziedzic, JE Bjorkholm, and Steven Chu. Observation of a single-beam gradient force optical trap for dielectric particles. *Optics letters*, 11(5):288–290, 1986.
- [9] Aleksandr Y Bekshaev, Konstantin Y Bliokh, and Franco Nori. Mie scattering and optical forces from evanescent fields: a complex-angle approach. *Optics express*, 21(6):7082–7095, 2013.
- [10] Michael A Bevan and Dennis C Prieve. Direct measurement of retarded van der Waals attraction. *Langmuir*, 15(23):7925–7936, 1999.
- [11] Konstantin Y Bliokh, Aleksandr Y Bekshaev, and Franco Nori. Extraordinary momentum and spin in evanescent waves. *Nature communications*, 5:14, 2013. ISSN 2041-1723. doi: 10.1038/ncomms4300. URL [http://www.ncbi.nlm.nih.gov/pubmed/24598730\\$& delimiter=o26E3oF\\$nhttp://arxiv.org/abs/1308.0547](http://www.ncbi.nlm.nih.gov/pubmed/24598730$& delimiter=o26E3oF$nhttp://arxiv.org/abs/1308.0547).
- [12] Seth Blumberg, Matthew W Pennington, and Jens-Christian Meiners. Do femtonewton forces affect genetic function? A review. *Journal of biological physics*, 32(2):73–95, 2006. ISSN 0092-0606. doi: 10.1007/s10867-005-9002-8. URL <http://www.ncbi.nlm.nih.gov/pmc/articles/PMC1470000/>
- [13] Craig F Bohren and Donald R Huffman. *Absorption and scattering of light by small particles*. John Wiley & Sons, 2008.
- [14] Howard Brenner. The slow motion of a sphere through a viscous fluid towards a plane surface. *Chemical Engineering Science*, 16(3):242–251, 1961.
- [15] Herbert B Callen and Theodore A Welton. Irreversibility and generalized noise. *Physical Review*, 83(1):34, 1951.
- [16] Mauricio D Carbajal-Tinoco, Ricardo Lopez-Fernandez, and José Luis Arauz-Lara. Asymmetry in colloidal diffusion near a rigid wall. *Physical review letters*, 99(13):138303, 2007.

- [17] Yih Fan Chen, J. N. Milstein, and Jens Christian Meiners. Femtonewton entropic forces can control the formation of protein-mediated DNA loops. *Physical Review Letters*, 104(4):1–4, 2010. ISSN 00319007. doi: 10.1103/PhysRevLett.104.048301.
- [18] B Derjaguin. On the repulsive forces between charged colloid particles and on the theory of slow coagulation and stability of lyophobe sols. *Transactions of the Faraday Society*, 35:203–215, 1940.
- [19] Albert Einstein. The theory of the brownian movement. *Ann. der Physik*, 17:549, 1905.
- [20] Albert Einstein. On the quantum theory of radiation. *Physikalische Zeitschrift*, 18:121–128, 1917.
- [21] Luc P Faucheu and Albert J Libchaber. Confined brownian motion. *Physical Review E*, 49(6):5158, 1994.
- [22] Scott G Flicker and Stacy G Bike. Measuring double layer repulsion using total internal reflection microscopy. *Langmuir*, 9(1):257–262, 1993.
- [23] Ernst-Ludwig Florin, Arnd Pralle, JK Heinrich Hörber, and Ernst HK Stelzer. Photonic force microscope based on optical tweezers and two-photon excitation for biological applications. *Journal of structural biology*, 119(2):202–211, 1997.
- [24] V Garcés-Chávez, D McGloin, MJ Padgett, W Dultz, H Schmitzer, and K Dholakia. Observation of the transfer of the local angular momentum density of a multiringed light beam to an optically trapped particle. *Physical review letters*, 91(9):093602, 2003.
- [25] V Garcés-Chávez, R Quidant, PJ Reece, G Badenes, L Torner, and K Dholakia. Extended organization of colloidal microparticles by surface plasmon polariton excitation. *Physical Review B*, 73(8):085417, 2006.
- [26] Frederick Gittes and Christoph F Schmidt. Interference model for back-focal-plane displacement detection in optical tweezers. *Optics Letters*, 23(1):7, 1998. ISSN 0146-9592. doi: 10.1364/OL.23.000007. URL <https://www.osapublishing.org/abstract.cfm?URI=ol-23-1-7>.

- [27] Frederick Gittes and Christoph F. Schmidt. Thermal noise limitations on micromechanical experiments. *European Biophysics Journal*, 27:75–81, 1998. ISSN 01757571. doi: 10.1007/s002490050113.
- [28] AJ Goldman, Raymond G Cox, and Howard Brenner. Slow viscous motion of a sphere parallel to a plane wall—i motion through a quiescent fluid. *Chemical Engineering Science*, 22(4):637–651, 1967.
- [29] David G Grier. A revolution in optical manipulation. *Nature*, 424(6950):810–6, 2003. ISSN 1476-4687. doi: 10.1038/nature01935. URL <http://www.ncbi.nlm.nih.gov/pubmed/12917694>.
- [30] David Jeffrey Griffiths and Reed College. *Introduction to electrodynamics*, volume 3. prentice Hall Upper Saddle River, NJ, 1999.
- [31] Amaury Hayat, J. P. Balthasar Mueller, and Federico Capasso. Lateral chirality-sorting optical forces. *Proceedings of the National Academy of Sciences*, 2015:201516704, 2015. ISSN 0027-8424. doi: 10.1073/pnas.1516704112. URL <http://www.pnas.org/lookup/doi/10.1073/pnas.1516704112>.
- [32] Laurent Helden, Elena Eremina, Norbert Riefler, Christopher Hertlein, Clemens Bechinger, Yuri Eremin, and Thomas Wriedt. Single-particle evanescent light scattering simulations for total internal reflection microscopy. *Applied optics*, 45(28):7299–7308, 2006.
- [33] Laurent Helden, Ralf Eichhorn, and Clemens Bechinger. Direct measurement of thermophoretic forces. *Soft Matter*, 11:2379–2386, 2015. ISSN 1744-683X. doi: 10.1039/C4SM02833C. URL <http://xlink.rsc.org/?DOI=C4SM02833C>.
- [34] Jacob N Israelachvili. *Intermolecular and surface forces / Jacob N. Israelachvili*. Academic Press London ; San Diego, 2nd ed. edition, 1991. ISBN 0123751810.
- [35] Petr Jákl, Mojmír Šerý, Jan Ježek, Alexandr Jonáš, Miroslav Liška, and Pavel Zemánek. Behaviour of an optically trapped probe approaching a dielectric interface. *Journal of Modern Optics*, 50(10):1615–1625, 2003.
- [36] John D Joannopoulos, Steven G Johnson, Joshua N Winn, and Robert D Meade. *Photonic crystals: molding the flow of light*. Princeton university press, 2011.

- [37] Alexandr Jonášs, Pavel Zemánek, and Ernst-Ludwig Florin. Single-beam trapping in front of reflective surfaces. *Optics letters*, 26(19):1466–1468, 2001.
- [38] Philip Jones, Onofrio Maragó, and Giovanni Volpe. *Optical tweezers: Principles and applications*. Cambridge University Press, 2015.
- [39] Satoshi Kawata and Tadao Sugiura. Movement of Micrometer-Sized Particles in the Evanescent Field of a Laser Beam. *Optics Letters*, 17(11):772–774, 1992.
- [40] Simon Kheifets, Akarsh Simha, Kevin Melin, Tongcang Li, and Mark G Raizen. Observation of brownian motion in liquids at short times: instantaneous velocity and memory loss. *science*, 343(6178):1493–1496, 2014.
- [41] KD Kihm, Arindam Banerjee, CK Choi, and T Takagi. Near-wall hindered brownian diffusion of nanoparticles examined by three-dimensional ratiometric total internal reflection fluorescence microscopy (3-d r-tirfm). *Experiments in Fluids*, 37(6):811–824, 2004.
- [42] Lulu Liu, Alexander Woolf, Alejandro W. Rodriguez, and Federico Capasso. Absolute position total internal reflection microscopy with an optical tweezer. *Proceedings of the National Academy of Sciences*, 111:E5609–E5615, 2014. ISSN 0027-8424. doi: 10.1073/pnas.1422178112. URL <http://www.pnas.org/lookup/doi/10.1073/pnas.1422178112>.
- [43] Lulu Liu, Simon Kheifets, Vincent Ginis, and Federico Capasso. Subfemtonewton Force Spectroscopy at the Thermal Limit in Liquids. *Physical Review Letters*, 116(22):228001, 2016. ISSN 0031-9007. doi: 10.1103/PhysRevLett.116.228001. URL <http://journals.aps.org/prl/abstract/10.1103/PhysRevLett.116.228001>.
- [44] Carlos López-Mariscal, Julio C Gutiérrez-Vega, Graham Milne, and Kishan Dholakia. Orbital angular momentum transfer in helical mathieu beams. *Optics express*, 14(9):4182–4187, 2006.
- [45] MP MacDonald, GC Spalding, and Kishan Dholakia. Microfluidic sorting in an optical lattice. *Nature*, 426(6965):421–424, 2003.
- [46] Masud Mansuripur. Electromagnetic stress tensor in ponderable media. *Optics Express*, 16(8):5193–5198, 2008.

- [47] Changjun Min, Zhe Shen, Junfeng Shen, Yuquan Zhang, Hui Fang, Guanghui Yuan, Luping Du, Siwei Zhu, Ting Lei, and Xiaocong Yuan. Focused plasmonic trapping of metallic particles. *Nature communications*, 4:2891, 2013. ISSN 2041-1723. doi: 10.1038/ncomms3891. URL <http://www.ncbi.nlm.nih.gov/articleinfo.fcgi?artid=3863898&tool=pmcentrez&rendertype=abstract>.
- [48] Gerhard Nägele. On the dynamics and structure of charge-stabilized suspensions. *Physics Reports*, 272(5):215–372, 1996.
- [49] Keir C Neuman and Steven M Block. Optical trapping. *Review of scientific instruments*, 75(9):2787–2809, 2004.
- [50] Timo A Nieminen, Nathaniel du Preez-Wilkinson, Alexander B Stilgoe, Vincent LY Loke, Ann AM Bui, and Halina Rubinsztein-Dunlop. Optical tweezers: Theory and modelling. *Journal of Quantitative Spectroscopy and Radiative Transfer*, 146:59–80, 2014.
- [51] M Nieto-Vesperinas, PC Chaumet, and A Rahmani. Near-field photonic forces. *Philosophical Transactions of the Royal Society A*, 362:719–738, 2004.
- [52] Andrey Novitsky, Cheng Wei Qiu, and Haifeng Wang. Single gradientless light beam drags particles as tractor beams. *Physical Review Letters*, 107(20):1–4, 2011. ISSN 00319007. doi: 10.1103/PhysRevLett.107.203601.
- [53] H. Nyquist. Thermal agitation of electric charge in conductors. *Phys. Rev.*, 32:110–113, Jul 1928. doi: 10.1103/PhysRev.32.110. URL <http://link.aps.org/doi/10.1103/PhysRev.32.110>.
- [54] Harry Nyquist. Thermal agitation of electric charge in conductors. *Physical review*, 32(1):110, 1928.
- [55] AT O’Neil, I MacVicar, L Allen, and MJ Padgett. Intrinsic and extrinsic nature of the orbital angular momentum of a light beam. *Physical review letters*, 88(5):053601, 2002.
- [56] Jean Perrin. Mouvement brownien et réalité moléculaire. In *Annales de Chimie et de Physique*, volume 18, pages 5–104, 1909.
- [57] Erwin JG Peterman, Frederick Gittes, and Christoph F Schmidt. Laser-induced heating in optical traps. *Biophysical journal*, 84(2):1308–1316, 2003.

- [58] Michelle L Povinelli, Marko Lončar, Mihai Ibanescu, Elizabeth J Smythe, Steven G Johnson, Federico Capasso, and John D Joannopoulos. Evanescent-wave bonding between optical waveguides. *Optics letters*, 30(22):3042–3044, 2005.
- [59] A Pralle, E-L Florin, EHK Stelzer, and JKH Hörber. Local viscosity probed by photonic force microscopy. *Applied Physics A: Materials Science & Processing*, 66:S71–S73, 1998.
- [60] A. Pralle, M. Prummer, E.L. Florin, E.H.K. Stelzer, and J.K.H. Hörber. Three-dimensional position tracking for optical tweezers by forward scattered light. *Microscopy Research and Technique*, 44(November 1998):378–386, 1999. doi: 10.1002/(SICI)1097-0029(19990301)44:
- [61] Dennis C Prieve and Nasser A Frej. Total internal reflection microscopy: a quantitative tool for the measurement of colloidal forces. *Langmuir*, 6(2):396–403, 1990.
- [62] Dennis C Prieve and John Y Walz. Scattering of an evanescent surface wave by a microscopic dielectric sphere. *Applied optics*, 32(9):1629–1641, 1993.
- [63] Edward M Purcell. Life at low reynolds number. *Am. J. Phys*, 45(1):3–11, 1977.
- [64] Francisco J Rodríguez-Fortuño, Nader Engheta, Alejandro Martínez, and Anatoly V Zayats. Lateral forces on circularly polarizable particles near a surface. *Nature communications*, 6, 2015.
- [65] Alexander Rohrbach and Ernst H K Stelzer. Trapping forces, force constants, and potential depths for dielectric spheres in the presence of spherical aberrations. *Applied optics*, 41(13):2494–2507, 2002.
- [66] Yohai Roichman, Bo Sun, Allan Stolarski, and David G. Grier. Influence of nonconservative optical forces on the dynamics of optically trapped colloidal spheres: The fountain of probability. *Physical Review Letters*, 101(12):1–5, 2008. ISSN 00319007. doi: 10.1103/PhysRevLett.101.128301.
- [67] Erik Schäffer, Simon F Nørrelykke, and Jonathon Howard. Surface forces and drag coefficients of microspheres near a plane surface measured with optical tweezers. *Langmuir*, 23(7):3654–3665, 2007.
- [68] Lennart Sjogren. Lecture notes on statistical processes. Chapter 6.

- [69] George E Uhlenbeck and Leonard Salomon Ornstein. On the theory of the brownian motion. *Physical review*, 36(5):823, 1930.
- [70] Mario B. Viani, Tilman E. Schäffer, Ami Chand, Matthias Rief, Hermann E. Gaub, and Paul K. Hansma. Small cantilevers for force spectroscopy of single molecules. *Journal of Applied Physics*, 86(4):2258, 1999. ISSN 00218979. URL <http://scitation.aip.org/content/aip/journal/jap/86/4/10.1063/1.371039>.
- [71] K Volke-Sepulveda, V Garcés-Chávez, S Chávez-Cerda, J Arlt, and K Dholakia. Orbital angular momentum of a high-order bessel light beam. *Journal of Optics B: Quantum and Semiclassical Optics*, 4(2):S82, 2002.
- [72] Giovanni Volpe, Romain Quidant, Gonçal Badenes, and Dmitri Petrov. Surface Plasmon Radiation Forces. *Physical Review Letters*, 96(23):238101, jun 2006. ISSN 0031-9007. doi: 10.1103/PhysRevLett.96.238101. URL <http://link.aps.org/doi/10.1103/PhysRevLett.96.238101>.
- [73] Ken-ichiro Wada, Keiji Sasaki, and Hiroshi Masuhara. Optical measurement of interaction potentials between a single microparticle and an evanescent field. *Applied Physics Letters*, 76(20):2815–2817, 2000.
- [74] John Y Walz. Ray optics calculation of the radiation forces exerted on a dielectric sphere in an evanescent field. *Applied optics*, 38(25):5319–5330, 1999.
- [75] Kai Wang, Ethan Schonbrun, Paul Steinurzel, and Kenneth B Crozier. Trapping and rotating nanoparticles using a plasmonic nano-tweezer with an integrated heat sink. *Nature communications*, 2:469, 2011. ISSN 2041-1723. doi: 10.1038/ncomms1480. URL <http://dx.doi.org/10.1038/ncomms1480>.
- [76] S. B. Wang and C. T. Chan. Lateral optical force on chiral particles near a surface. *Nature Communications*, 5:1–8, 2014. ISSN 2041-1723. doi: 10.1038/ncomms4307. URL <http://www.nature.com/doifinder/10.1038/ncomms4307>.
- [77] Shubo Wang and Che Ting Chan. Strong optical force acting on a dipolar particle over a multilayer substrate. *Optics express*, 24(3):2235–2241, 2016.

- [78] Yiqiong Zhao, J. Scott Edgar, Gavin D M Jeffries, David McGloin, and Daniel T. Chiu. Spin-to-orbital angular momentum conversion in a strongly focused optical beam. *Physical Review Letters*, 99(August):15–18, 2007. ISSN 00319007. doi: 10.1103/PhysRevLett.99.073901.